Nucleon generalized form factors from two-flavor lattice QCD and stochastic three-point functions with open indices

Dissertation

zur Erlangung des Doktorgrades
der Naturwissenschaften (Dr. rer. nat.)
der Fakultät für Physik
der Universität Regensburg

vorgelegt von

Rudolf H. Rödl

aus Garmisch-Partenkirchen

im Jahr 2020

Promotionsgesuch eingereicht am: 22. Januar 2020
Die Arbeit wurde angeleitet von: Prof. Dr. Andreas Schäfer

Contents

1 Introduction

1.1 QCD

Quantum Chromodynamics (QCD) is a non-abelian gauge theory which describes the strong interaction of quarks and gluons. A quark is a fermion, i.e., a spin-1/2 particle, with fractional electrical charge, color charge and flavor. In total there are six quark flavors q called up (u), down (d), charmed (c), strange (s), top(t) and bottom (b). Quarks participate in strong interactions because of their color charge. In total there are $N_c = 3$ different colors. However, quarks do not interact with each other directly. The interaction between quarks is mediated by gluons which are massless gauge bosons with spin 1. Neither quarks nor gluons are observed as free particles. This is a central but unproven hypothesis of Quantum Chromodynamics. Instead, quarks and gluons form color-neutral particles called hadrons. The two most prominent subclasses of hadrons are mesons ($q_1\,\overline{q}_2$), which consist of a quark q_1 and an anti-quark $\overline{q}_2$, and baryons ($q_1\,q_2\,q_3$), which are formed by three quarks. For the structure of ordinary matter, the first generation of quarks, i.e., the first two u and d, play an important role because they form the most stable particles. The proton for instance is composed of two u quarks and one d quark which yields a total electrical charge of $1 = 2/3 + 2/3 - 1/3$. Currently, the free proton is considered to be a stable particle. A neutron is slightly heavier than a proton and decays to a proton through the weak interaction

$$n \rightarrow p + e^- + \nu_e$$

with a mean life time of about 15 minutes. In contrast to hadrons, all mesons are unstable. The lightest mesons are the pions which come in three electricals variants. There are two charged pions, namely the π^+ $(u, \overline{d})$ and the π^- $(d, \overline{u})$ as well as the electrically neutral pion π^0, which is a linear combination of $(u, \overline{u})$ and $(d, \overline{d})$ states. The mean life time of the charged pions is about 26 nanoseconds. The complex phenomena of the strong interaction are consequences of an elegant mathematical structure, known as the QCD Lagrangian

$$\mathcal{L}_{\mathrm{QCD}} = \sum_f \overline{\Psi}_f \left(i \not{D} - m_f \right) \Psi_f - \frac{1}{4} F^A_{\mu\nu} F^{A\mu\nu} \,. \tag{1.1}$$

While this formula looks rather simple, it is in fact notoriously hard to solve due its non-abelian structure. Over time physicist developed different approaches to tackle QCD. One possibility is the utilization of perturbation theory where one uses power series expansions in a small parameter. This approach has been successfully applied to quantum electrodynamics (QED) where the small expansion parameter is the fine structure constant $\alpha_{\mathrm{em}} \approx 1/137$. This approach, however, can only be applied partially to QCD since the expansion parameter $\alpha_{\mathrm{s}}(Q^2)$ can not be assumed to be small for all values of the energy scale Q^2. A relatively new approach to study QCD in its non-perturbative region is given by the so-called AdS/QCD duality, which is a manifestation of the AdS/CFT correspondence. It applies the holographic principle and maps a strongly coupled field theory (which is similar to QCD) to a string theory in its weak-coupling limit which allows for the treatment of problems which would be otherwise inaccessible. All these different attempts to tackle QCD originate for the fact that QCD has unsolved puzzles such as quark confinement which is one of the seven Millennium Prize Problems stated by the Clay Mathematics Institute. However, one has to point out that many aspects of QCD are well understood. One of the most prominent examples is asymptotic freedom which was discovered by Gross, Politzer and Wilczek. Asymptotic freedom means that the effective quark-gluon coupling becomes weaker as the energy scale of the process increases. In fact, the QCD scale dependence of the coupling constant can be derived from renormalization group equations. An explicit one-loop calculation yields

$$\alpha_{\mathrm{s}}(\mu) = \frac{4\pi}{\beta_0 \ln(\frac{\mu}{\Lambda_{\mathrm{QCD}}})} \,. \tag{1.2}$$

The dimension-full parameter $\Lambda_{\mathrm{QCD}} \approx 200\,\mathrm{Mev}$ defines what weak and strong means and is a consequence of a renormalization procedure which introduces a scale μ. The remaining parameter β_0 can be computed e.g. by a one-loop calculation of the gluon self-energy yielding

$$\beta_0 = \frac{1}{3} \left(11 \cdot N_c - 2 \cdot N_f \right) , \tag{1.3}$$

where N_c and N_f denote the number of colors and quark flavors, respectively. For QCD with $N_c = 3$ and $N_f = 6$ β_0 is negative implying that Eq. (1.2) grows for $\mu \to \Lambda_{\text{QCD}}$.

Let us now change the perspective and focus on the theoretical framework. QCD is formulated in a mathematical language which is commonly known as quantum field theory (QFT). It is a combination of classical field theory, quantum mechanics and special relativity. Particles are described in terms of dynamical fields governed by the Lagrangian density which can be conveniently written as

$$\mathcal{L}_{\text{QCD}} = \mathcal{L}_{\text{quark}} + \mathcal{L}_{\text{gauge}} + \mathcal{L}_{\text{ghost}} + \mathcal{L}_{\text{gaugefixing}} \,. \tag{1.4}$$

The two terms, $\mathcal{L}_{\text{ghost}}$ and $\mathcal{L}_{\text{gaugefixing}}$, are necessary for the quantization of the classical theory, i.e, they maintain the consistency of the path integral which is usually used for the quantization of non-Abelian gauge field theories. However, we do not discuss this rather technical topic here because none of the terms are needed to formulate QCD on the lattice. Instate we discuss the fermionic part of the QCD Lagrangian

$$\mathcal{L}_{\text{quark}} = \sum_f \overline{\Psi}_f \, (i \not{D}[\mathcal{A}] - m_f) \, \Psi_f \,. \tag{1.5}$$

Quarks with flavor $f \in \{u, d, c, s, t, b\}$ and mass m_f are represented by spinors ψ_f which are vectors in color ($N_c = 3$) and spin ($N_s = 4$) space. They transform under the fundamental representation of the $SU(3)$ color group. The fermionic part is minimally coupled to the gauge fields $\mathcal{A}$, i.e. it depends on the gauge fields only trough the covariant derivative

$$\not{D}[\mathcal{A}] = \gamma^\mu \partial_\mu - \mathrm{i} g_s \gamma^\mu \, \mathcal{A}^A_\mu \, t^A \,, \tag{1.6}$$

with the γ-matrices defined by $\{\gamma_\mu, \gamma_\nu\} = 2\, g_{\mu\nu}$. Gluonic fields $\mathcal{A}^A_\mu$ are contracted with 3×3 matrices t^C, which are the generators of the $SU(3)$ algebra

$$[t^A, t^B] = \mathrm{i} \, f^{ABC} \, \lambda^C \,, \tag{1.7}$$

$$\mathrm{Tr}\left(t^A t^B\right) = \frac{1}{2} \delta^{AB} \,. \tag{1.8}$$

The strong coupling g_s is an input parameter of the theory and appears also in

$$\mathcal{L}_{\text{gauge}} = -\frac{1}{4} F^A_{\mu\nu} F^{A\,\mu\nu}$$

which describes the gluon dynamics in terms of the field strength tensor

$$F^A_{\mu\nu} = \partial_\mu \, \mathcal{A}^A_\nu - \partial_\nu \, \mathcal{A}^A_\mu + g_s f^{ABC} \mathcal{A}^B_\mu \mathcal{A}^C_\nu \,, \tag{1.9}$$

with the $SU(3)$ structure constants f^{ABC}. The gluon (vector) fields $\mathcal{A}^A_\mu$ are parametrized

by $A \in \{1 \dots N_c^2 - 1\}$. The eight gluons transform under the adjoint representation of $SU(3)$. The quadratic term in $\mathcal{A}$ is the origin for the non-trivial gluon self interaction, a characteristic feature of non-abelian field theories. In the following we discuss some aspects about the construction of the QCD Lagrangian which is mainly driven by symmetry considerations. One of these symmetries is local gauge symmetry, a fundamental concept in quantum field theory. Local gauge symmetry in QCD means, that physics is invariant under local $SU(3)$ transformations

$$\Omega(x) = e^{\mathrm{i}\,\Theta(x)^A \cdot t^A} \quad \text{with} \quad \det(\Omega(x)) = 1\,.$$

Quarks with flavor f transform according to the following equations

$$\Psi_f(x)^\alpha_a \to \Psi'_f(x)^\alpha_a = \Omega(x)_{ab}\,\Psi_f(x)^\alpha_b\,, \tag{1.10}$$

$$\overline{\Psi}_f(x)^\alpha_a \to \overline{\Psi'}_f(x)^\alpha_a = \overline{\Psi}_f(x)^\alpha_b\,\Omega^{-1}(x)_{ba}\,. \tag{1.11}$$

To illustrate local gauge invariance let us revisit the formal definition of mesons M and baryons B

$$\begin{aligned} M(x)^{\alpha\beta}_{f_1 f_2} &\equiv \overline{\Psi}_{f_1}(x)^\alpha_c\,\Psi_{f_2}(x)^\beta_c\,, \\ B(x)^{\alpha\beta\gamma}_{f_1 f_2 f_3} &\equiv \epsilon_{ijk}\,\Psi_{f_1}(x)^\alpha_i\,\Psi_{f_2}(x)^\beta_j\,\Psi_{f_3}(x)^\gamma_k\,. \end{aligned}$$

A local gauge transformation yields

$$\begin{aligned} M_{f_1 f_2}(x)^{\alpha\beta} &\to M'_{f_1 f_2}(x)^{\alpha\beta} = \overline{\Psi}_{f_1}(x)^\alpha_a\,\Omega^{-1}(x)_{ac}\,\Omega(x)_{cd}\Psi_{f_2}(x)^\beta_d = \overline{\Psi}_{f_1}(x)^\alpha_a\,\delta_{ad}\Psi_{f_2}(x)^\beta_d \\ &= M_{f_1 f_2}(x)^{\alpha\beta}\,, \\ B(x)^{\alpha\beta\gamma}_{f_1 f_2 f_3} &\to B'(x)^{\alpha\beta\gamma}_{f_1 f_2 f_3}\epsilon_{ijk}\,\Omega(x)_{il}\,\Omega(x)_{jm}\,\Omega(x)_{kq}\,\Psi_{f_1}(x)^\alpha_l\,\Psi_{f_2}(x)^\beta_m\,\Psi_{f_3}(x)^\gamma_q \\ &= \det(\Omega)\,\epsilon_{lmq}\,\Psi_{f_1}(x)^\alpha_l\,\Psi_{f_2}(x)^\beta_m\,\Psi_{f_3}(x)^\gamma_q \\ &= B(x)^{\alpha\beta\gamma}_{f_1 f_2 f_3}\,, \end{aligned}$$

which shows that mesons and baryons are invariant under local gauge transformations. However, local gauge invariance in QCD requires that not only physical observables are invariant but the complete QCD Lagrangian. The mass term in Eq. (1.5) is trivially gauge invariant, however, this does not apply to the covariant derivative. One requires, that it transforms like a quark field

$$\mathrm{D}[\mathcal{A}]^\mu\,\Psi_f \to (\mathrm{D}[\mathcal{A}]^\mu\,\Psi_f)' \equiv \Omega(x)\,\mathrm{D}^\mu\,\Psi_f$$

which yields the following transformation of the gluon fields

$$t^A\mathcal{A}^A_\mu \to t^A\mathcal{A}'^A_\mu = \Omega(x)\,t^A\,\mathcal{A}^A_\mu\,\Omega^{-1}(x) + \frac{1}{g_\mathrm{s}}\,(\partial_\mu\Omega(x))\;\Omega^{-1}(x)\,. \tag{1.12}$$

In other words, the requirement of local gauge invariance in the fermionic sector defines the transformation property of the gauge fields. Subsequently, one must verify that the gauge sector is also invariant. To that end one considers the transformation property of the field strength tensor which can be derived from Eq. (1.12)

$$t^A F^A_{\mu\nu} \rightarrow t^A F'^A_{\mu\nu} = \Omega(x)\, t^A F^A_{\mu\nu}\, \Omega^{-1}(x)\,. \tag{1.13}$$

In this context it is convenient to re-express the gluonic part of Lagrangian

$$\mathcal{L}_{\text{gauge}} = -\frac{1}{4} F^A_{\mu\nu} F^{A\mu\nu} = -\frac{1}{2}\,\text{Tr}\, F^A_{\mu\nu} F^{B\mu\nu}\,\text{Tr}\left(t^A t^B\right) = -\frac{1}{2}\text{Tr}\left(F^A_{\mu\nu}\, t^A\; F^{B\mu\nu}\, t^B\right)\,. \tag{1.14}$$

Applying a local gauge transformation yields

$$\begin{aligned}
\mathcal{L}_{\text{gauge}} \rightarrow \mathcal{L}'_{\text{gauge}} &= -\frac{1}{2}\text{Tr}\left(F'^A_{\mu\nu}\, t^A\; F'^{B\mu\nu}\, t^B\right) \\
&= -\frac{1}{2}\text{Tr}\left(\Omega(x)\, F^A_{\mu\nu}\, t^A \Omega^{-1}(x)\, \Omega(x)\, F^{B\mu\nu}\, t^B\, \Omega^{-1}(x)\right) \\
&= -\frac{1}{2}\text{Tr}\left(F^A_{\mu\nu}\, t^A\; F^{B\mu\nu}\, t^B\right) = \mathcal{L}_{\text{gauge}}\,.
\end{aligned}$$

1.2 Lattice QCD

In order to access QCD in the non-perturbative region we follow an approach called "lattice gauge theory" which was proposed by K. Wilson in 1974 [1]. In this work he demonstrates how to quantize a gauge field theory on a discrete lattice in Euclidean space-time in a gauge-invariant manner. Due to the discrete formulation of QCD it is possible to rigorously define the path integral which is needed for the quantization of the classical theory. Analogous to statistical mechanics one is able to define the QCD partition function

$$\mathcal{Z} = \int \prod_x \prod_{\mu=0}^{3} \mathrm{d}U(x)_\mu\, \mathrm{e}^{-S_{\text{eff}}[U]}$$

The gauge field variables $U(x)_\mu$ which are elements of the $SU(3)$ group play an important role in this formulation. Physically speaking they represent the gluonic degrees of freedom. Quark and anti-quark fields which are Grassmann-valued objects have been analytically integrated out and are absorbed in the action S_{eff}. The positive real valued factor $\mathrm{e}^{-S_{\text{eff}}[U]}$ is interpreted as a weight function. Configurations U, close to the minimum of $S_{\text{eff}}[U]$ are more important. To demonstrate the connection to statistical mechanics we quote the partition function of a classical spin system

$$\mathcal{Z} = \sum_s \mathrm{e}^{-\beta H[s]} \quad \text{with} \quad \beta = \frac{1}{k_B T}$$

The similarity between the two different disciplines are important because established numerical methods developed for statistical mechanics can be adapted to lattice QCD. In particular Mote Carlo techniques are used to create sets of gauge configurations $\{U(x)_\mu\}_{i=1\ldots N_{\text{conf}}}$. These sets are commonly called gauge ensembles and are used to calculate physical observables like masses or hadronic matrix elements. Depending on the considered observable the number of necessary configurations N_{conf} varies. Typically N_{conf} is chosen between several hundreds and several thousands. The generation process of gauge ensembles is an expensive task and needs to be performed on a reasonably-sized super computer. After the generation they can be used for various types of measurements. Nowadays, the generation of gauge configurations is a task which can hardly be achieved by a single group, especially if the set of gauge configurations is large. Instead it is a joint effort project which requires larger-scale collaborations like in CLS (Coordinated Lattice Simulations). The aim of CLS is the generation of a set of gauge ensembles which allow to reach the required precision and control of systematic errors in particular with respect to the continuum limit. However, one has to keep in mind that the generation is not only expensive but comes with significant subtleties. For instance one has to keep track of autocorrelations in Monte-Carlo time, which are expected to grow while approaching the continuum limit. As the physical lattice spacing approaches the region smaller than 0.05 fm lattice QCD simulations tend to get trapped in the topological charge sectors of field space and may consequently yield biased results in practice. To circumvent this behavior, termed topological freezing, one has to improve methods and algorithms [2, 3]. One possibility to circumvent this effect are open boundary conditions in time and periodic boundary conditions in the space directions. This setup leads to a topological charge flow and thus decrease the autocorrelation times. However, further obstacles arise from the fact that the discretization of the fermionic and gluonic parts of the Lagrangian are not unique and can suffer from discretization effects, respectively. For instance the Wilson quark action has $\mathcal{O}(a)$ discretization errors. Using this type of action makes it harder to perform the continuum limit ($a \to 0$) because the extrapolation has to be performed linearly in the lattice spacing. This can be resolved by an $\mathcal{O}(a)$ improved action which gives a more reliable $\mathcal{O}(a^2)$ extrapolation. Typically improvements of this kind do not come for free. They introduce new parameters which have to be determined or tuned carefully. Besides the mentioned obstacles lattice QCD ultimately empowers us to calculate observables from first principles using statistical methods. For example, the expectation value of an observable O can be evaluated as the statistical average over the set of gauge configurations $\{U(x)_\mu\}_{i=1\ldots N_{\text{conf}}}$ according

to

$$\langle O \rangle = \frac{1}{N_{\text{conf}}} \sum_{i=1}^{N_{\text{conf}}} O[U_i] + \mathcal{O}(1/\sqrt{N_{\text{conf}}}) \,. \tag{1.15}$$

The estimate for the observable O has an intrinsic statistical uncertainty. Corrections can be expected to be proportional to the inverse square root of the number of configurations in the ensemble. Due to the fact that the correction term vanishes only in the limit $N_{\text{conf}} \to \infty$ one has to find reliable estimates for the statistical errors. There are different methods to calculate these errors which each have advantages and disadvantages of their own. Most often, re-sampling techniques such as Jackknife or Bootstrap are used. At this stage one has also to track autocorrelations of the measured observable. In practice, two methods are widely used to estimate autocorrelations. The first method is the direct calculation of the autocorrelation function and the second is to perform a binning analysis. The central task in a binning analysis is to determine a proper binsize. This has to be carried out separately for each observable. While it is not an unmanageable task, it is not perfectly rigid and opens up room for time-consuming discussions.

In contrast to other approaches lattice QCD does not require model assumptions. The only (bare) input parameters are the quark masses and the strength of the coupling. However, predictions from lattice QCD calculations suffer from systematic effects which have to be treated in a separate step. For instance, the results will depend on the lattice size as well as on the lattice spacing. Therefore, one has to carry out the measurement of interest on different sets of gauge ensembles in a way such that one is able to systematically extrapolate to physical results. These extrapolations may introduce an implicit model dependence to LQCD simulations. For instance, one can use chiral perturbation theory (χ-PT) for the extrapolation to physical pion masses. While this approach is not wrong in principle, one is confronted with the question whether χ-PT is allowed to be applied for the current set of gauge ensembles. The parameter which is addressed by this question is the pion mass associated to the gauge ensemble. A further notorious systematic effect which needs to be treated are excited-state contaminations. These appear, e.g., in the calculation of matrix elements. The most straight-forward way to reduce them is to increase the source-sink distance of the involved three-point function. This will clearly improve the situation because excited-state contributions are exponentially stronger suppressed as the ground-state matrix element one is typically interested in. The drawback of this straight-forward method manifests itself in a decreasing signal-to-noise ratio of the ground-state matrix element. In principle this can be compensated by increasing the number of gauge configurations. In order to reduce the statistical error of the considered matrix elements by a factor 1/2 one needs four times the number of gauge

configurations. This clearly shows that this straight-forward approach is limited by the production cost in practice. However, this is not the only method to reduce excited-state contributions. One can suppress them with smearing techniques which aim to improve the ground-state dominance. To achieve this one has to choose a smearing regime which introduces additional parameters to tune. On top of this approach one can create ensembles with multiple source-sink separations in order to parametrize the excited-state contributions by using a suitable fit Ansatz. While this can considerably improve the situation in some scenarios, there are situations where this can not be accomplished at all. For instance if the signal of the correlation functions is not good enough to restrict the additional parameters of the parametrization. This is often the case when one considers operators with an increasing number of derivatives and high momenta. Generating multiple source-sink separations may still pay off in this situation since one can study the systematic effects of source-sink separations on the final result. Another kind of systematic effect are contributions which arise from so-called disconnected diagrams. In the past, disconnected contributions have been neglected because they were too expensive to calculate. With recent improvements in computer power and algorithms, the calculation of disconnected contributions has become feasible. However, the resulting contributions tend to be noisy which in turn yields larger statistical uncertainties of the final result. A standard approach to calculate disconnected loops is stochastic estimation, which introduces an additional error on top of the gauge noise already present. Because of the difficulties associated with disconnected diagrams, many lattice QCD calculations still address only isovector observables, which do not have disconnected contributions. With all these subtleties in mind, lattice QCD finally allows us to study the nucleon structure from first principles, which is considered a milestone of hadronic physics. For instance we are able to compute the axial, scalar, tensor and pseudoscalar isovector couplings of the nucleon [4]. Furthermore, lattice QCD allows us to access moments of parton distribution functions and form factors as well as generalized form factors (GFFs) [5]. These observables provide important information on the distribution of momentum, spin and charge within a nucleon. The calculation of GFFs on the lattice is an important contribution to the understanding of hadron structure. One prominent example is the calculation of the total angular momentum of a quark in a nucleon which can not be measured directly in an experiment except for its spin contribution. By means of lattice calculations we make a contribution to the question how all angular momenta in a proton add up to one half. In the following sections we introduce basic concepts relevant for a grasp of lattice QCD.

1.3 Wick rotation

The attempt to study QCD numerically is closely connected to the path integral quantization of the classical continuum theory. In terms of lattice QCD the most important feature is the ability to quantize the classical theory non-perturbatively. Beside this, the path integral provides a set of rules for the computation of observables. As an illustration, one can compute the expectation value of an operator $\hat{\mathcal{O}}_n$ using the path integral formalism

$$\langle \mathcal{O}_n \rangle = \frac{1}{\mathcal{Z}} \int \mathcal{D}\left[A_\mu , \Psi , \overline{\Psi} \right] \cdot \mathcal{O}_n \cdot \mathrm{e}^{\mathrm{i}S^M\left[A_\mu , \Psi , \overline{\Psi} \right]} , \tag{1.16a}$$

$$\mathcal{Z} = \int \mathcal{D}\left[A_\mu , \Psi , \overline{\Psi} \right] \cdot \mathrm{e}^{\mathrm{i}S^M\left[A_\mu , \Psi , \overline{\Psi} \right]} . \tag{1.16b}$$

Adapting this continuum formulation to a numerical accessible counterpart consists of two major parts. First, one must formulate a proper discretization of the theory to make the number of integration variables finite. This step is addressed in section 1.4. The second part addresses the factor i in $\mathrm{e}^{\mathrm{i}S^M\left[A_\mu , \Psi , \overline{\Psi} \right]}$ which leads to strong oscillations. Problems of that type do not exclusively appear in lattice QCD but are known to happen also in other fields. For example, it is pointed out in [6] that the indefinite metric of Minkowski space causes many problems in QFT which can be avoided by analytic continuation of time. This trick is used in lattice QCD and known as Wick rotation. One rotates to imaginary time $x^0 \to -\mathrm{i}x^4$ to convert the oscillating phase to a real-valued negative exponential

$$\mathrm{e}^{\mathrm{i}S^M\left[A_\mu , \Psi , \overline{\Psi} \right]} \xrightarrow{\text{Wick rotation}} \mathrm{e}^{\mathrm{i}\mathrm{i}S^E\left[A_\mu , \Psi , \overline{\Psi} \right]} = \mathrm{e}^{-S^E\left[A_\mu , \Psi , \overline{\Psi} \right]} . \tag{1.17}$$

The substitution must be applied consistently to all objects in the action integral. This includes the integration measure, derivative operator, gluon fields as well as the definition of the γ-matrices

$$\{\gamma_\mu, \gamma_\nu\} = 2g_{\mu\nu} \to \{\gamma_\mu^E, \gamma_\nu^E\} = 2\delta_{\mu\nu} . \tag{1.18}$$

A consistent application of the described steps yields the following transformation for the ferminoic part of the action

$$S_F^M \left[A_\mu , \Psi , \overline{\Psi} \right] = \int \mathrm{d}^4x \left(\sum_f \overline{\Psi}_f \left(\mathrm{i}\gamma^\mu \mathrm{D}_\mu - m_f \right) \Psi_f \right) \xrightarrow{\text{Wick rotation}}$$

$$\xrightarrow{\text{Wick rotation}} \mathrm{i} \int \mathrm{d}^4x^E \left(\sum_f \overline{\Psi}_f \left(\gamma_\mu^E \mathrm{D}_\mu^E + m_f \right) \Psi_f \right) \equiv \mathrm{i} S_F^E \left[A_\mu , \Psi , \overline{\Psi} \right] . \tag{1.19}$$

For the gluonic part one finds

$$S_G^M[A_\mu] = \int \mathrm{d}^4x \left(-\frac{1}{4}F^A_{\mu\nu}F^{A\mu\nu}\right) \xrightarrow{\text{Wick rotation}}$$
$$\xrightarrow{\text{Wick rotation}} \mathrm{i}\int \mathrm{d}^4x^E \left(\frac{1}{4}(F^E)^A_{\mu\nu}(F^E)^A_{\mu\nu}\right) \equiv \mathrm{i}S_G^E[A_\mu]\,. \tag{1.20}$$

The Wick rotation originates from a deep connection between Euclidean and Minkowski QFT. The theoretical foundations are given in terms of the Wightman axioms and the Osterwalder-Schrader theorem [7, 6, 8]. The index E is from here on omitted for notational convenience since only the Euclidean formulation of the theory is considered.

1.4 Discrete space-time

The first step towards a well-defined path integral is the discretization of space-time [1]. This is done by replacing the space-time continuum with a discrete mesh of lattice points which are part of a finite hypercubic lattice. Lattice points are usually referred to as sites. The distance between two neighbouring sites is called the lattice spacing, denoted by the letter a. A formal definition of the lattice Λ is [9]

$$\Lambda = \{n = (n_1, n_2, n_3, n_4) \quad n_\mu = (0, \ldots N_\mu - 1)\} \tag{1.21}$$

and depicted in Fig. 1.1. We restrict ourselves to a spatial box size of $N_S = N_1 = N_2 = N_3$ and a temporal extent of $N_T = N_4$. For typical applications one sets $N_T > N_S$. Physical sites are given in terms of $x = a \cdot n$ and the momentum space lattice is defined according to

$$\tilde{\Lambda} = \left\{ p = (p_1, p_2, p_3, p_4) \,\middle|\, p_\mu = \frac{2\pi}{aN_\mu}\left(k_\mu + \theta_\mu\right),\, k_\mu = -\frac{N_\mu}{2} + 1, \ldots, \frac{N_\mu}{2} \right\}. \tag{1.22}$$

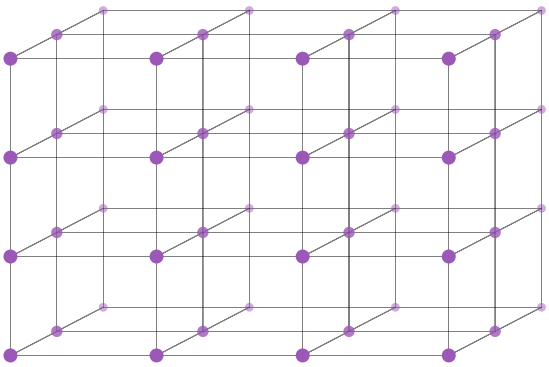

Figure 1.1: Three dimensional lattice Λ. Sites are shown as circles and the distance between to sites is a.

The discretization of space-time yields two types of regulators. The lattice spacing a plays the role of the ultraviolet regulator while the finite size of the lattice yields a maximal momentum

$$p_\mu^{\max} = \frac{2\pi}{aN_\mu} \cdot \left(\frac{N_\mu}{2} + \theta_\mu \right) \tag{1.23}$$

making the theory infrared safe. To obtain physical results one must remove both regulators in a systematic fashion. The two necessary steps are performed by taking the continuum limit $a \to 0$ as well as the infinite volume limit $N_\mu \to \infty$.

The parameter θ_μ in Eq. (1.22) is used to impose boundary conditions. Anti-periodic boundary conditions are obtained by $\theta_\mu = 1/2$ and periodic boundary conditions with $\theta_\mu = 0$. In typical lattice QCD calculations, one uses periodic boundary conditions in space-like directions to maintain translational invariance. In temporal direction one imposes periodic boundary conditions for the gauge fields and anti-periodic boundary conditions for the fermions. However, one is not restricted to $\theta_\mu = 1/2$ or $\theta_\mu = 0$. Arbitrary values can be used instead, refereed to as twisted boundary conditions. Imposing them to quark fields has the advantage to adjust the otherwise static lattice momenta

$$p_\mu = \frac{2\pi}{aN_\mu} \left(k_\mu + \theta_\mu \right) .$$

1.5 Free fermion discretization

After the discretization of the Euclidean space-time one must define a discrete action. In this section we consider the Euclidean continuum action in Eq. (1.19) for fermions in the free case

$$S_F \left[\mathcal{A} = 0 \, , \Psi \, , \overline{\Psi} \right] = \int \mathrm{d}^4 x \Big[\overline{\Psi}(x) \, \left(\gamma_\mu \partial_\mu + m \right) \, \Psi(x) \Big] . \tag{1.24}$$

For simplicity we consider only a single quark flavor but the generalization to more flavors is straight forward. Several steps are necessary to obtain a lattice version. First, one uses spinors which are defined only on the lattice sites $\Psi(x) \to \Psi(x = an)$ with $n \in \Lambda$. This step is crucial because it makes the number of fermionic degrees finite (c.f. Fig. 1.1). Subsequently one converts the derivative operator ∂_μ. Note that this conversion is not unique. As a preliminary step we consider a Taylor expansion of an one-dimensional function $f(z)$ evaluated at $z - a$ and $z + a$ [9]

$$f(z - a) = f(z) - \frac{a}{1} f'(z) + \frac{a^2}{2} f''(z) - \frac{a^3}{6} f'''(z) + \dots , \tag{1.25}$$

$$f(z + a) = f(z) + \frac{a}{1} f'(z) + \frac{a^2}{2} f''(z) + \frac{a^3}{6} f'''(z) + \dots . \tag{1.26}$$

Subtraction of Eq. (1.25) from Eq. (1.26) yields the so-called symmetric derivative

$$f'(z) = \frac{f(z+a) - f(z-a)}{2a} + \mathcal{O}(a^2)\,, \tag{1.27}$$

which is a generalization of the ordinary derivative. Symmetric derivatives are usually used because they have discretization errors which are quadratic in a. The generalization to multiple directions μ is straight forward

$$\partial_\mu \Psi(x) = \frac{\Psi(x + a\hat{\mu}) - \Psi(x - a\hat{\mu})}{2a} + \mathcal{O}(a^2)\,. \tag{1.28}$$

$\hat{\mu}$ represents the unit vector in the μ direction. Finally, one replaces the integral in Eq. (1.24) by a sum over all lattice sites yield the free fermion lattice action

$$S_F^\Lambda\left[\mathcal{A} = 0\,,\Psi\,,\overline{\Psi}\,\right] = a^4 \sum_{x\in\Lambda} \overline{\Psi}(x) \left(\sum_{\mu=1}^{4} \gamma_\mu \frac{\Psi(x + a\hat{\mu}) - \Psi(x - a\hat{\mu})}{2a} + m\Psi(x) \right)\,, \tag{1.29}$$

The continuum formulation can be restored in the limit $a \to 0$ where the physical volume of the lattice must be kept fixed. Note that this action is not gauge invariant.

1.6 Gauge links

Gauge links are the most fundamental objects in lattice QCD. They have several remarkable properties and play a special role as integration variables in the lattice QCD path integral. In contrast to the so far introduced lattice spinors they are oriented and commonly denote as $U_\mu(x)$. The orientation is manifested by the index μ. A link $U_\mu(x)$ defined for the lattice site $x = an$ connects x with any adjacent site $(x + a\hat{\mu})$. Gauge links in backward direction are written as $U_{-\mu}(x)$. Forward and backward links are not independent but connected via $U_{-\mu}(x) \equiv U_\mu^\dagger(x - a\hat{\mu})$. A graphical representation in three dimensions is presented in Fig. 1.2.

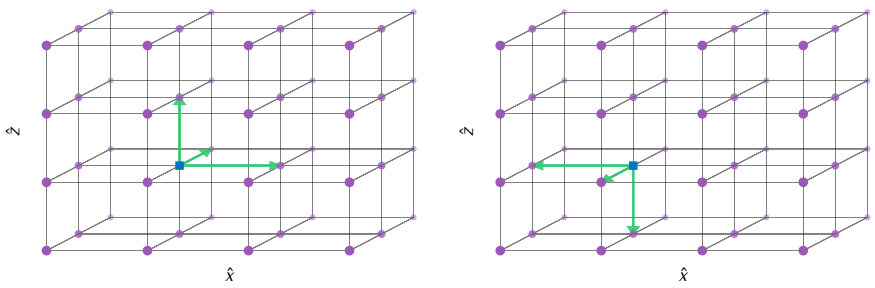

(a) Forward links. (b) Backward links.

Figure 1.2: Gauge links $U_\mu(x)$ are oriented objects, represented by arrows along the μ direction. The starting site $x = an$ is depicted as blue square.

The construction of the gauge links is connected to a continuum object known as gauge transporter

$$G(x, y) \equiv \mathrm{P} \exp\left(\mathrm{i} \int_{\mathcal{C}(x,y)} \mathcal{A} \cdot \mathrm{d}s\right) . \tag{1.30}$$

The gauge transporter is the path ordered integral over the algebra valued gauge fields $\mathcal{A}_\mu$ along a curve $\mathcal{C}$ connecting the points x and y. P denotes path-ordering of the colour matrices along the line $\mathcal{C}(x, y)$. The gauge links can be interpreted as infinitesimal versions of the continuum gauge transporter

$$U_\mu(x) \equiv \exp\left(\mathrm{i}\mathcal{A}_\mu(x)a\right) . \tag{1.31}$$

This becomes obvious in the limit $a \to 0$ where the integral in Eq. (1.30) is approximated by the gluon field times the lattice spacing a. Since only a single gluon field is involved the path ordering becomes trivial and one can drop the operator P. The transformation properties of the the links under a local gauge rotation are

$$U_\mu(x) \to U'_\mu(x) = \Omega(x)\, U_\mu(x)\, \Omega^\dagger(x + a\hat{\mu}) , \tag{1.32a}$$

$$U_{-\mu}(x) \to U'_{-\mu}(x) = \Omega(x)\, U_{-\mu}(x)\, \Omega^\dagger(x - a\hat{\mu}) . \tag{1.32b}$$

Gauge links are the building blocks for the construction of gauge invariant objects. A piecewise continuous string of gauge links form the lattice gauge transporter, i.e., the lattice counterpart of Eq. (1.30). An example of such a setup is shown in Fig. 1.3.

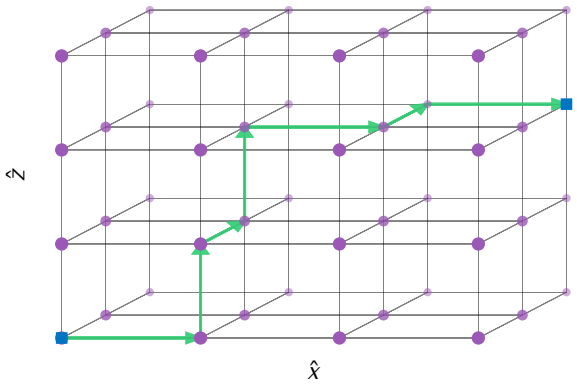

Figure 1.3: Lattice version of the gauge transporter constructed in terms of gauge links. The gauge transporter connects the sites x and $y \equiv x + a(3\hat{x} + 2\hat{y} + 2\hat{z})$ which are depicted as blue squares respectively. The site x is shown on the bottom left corner.

The corresponding algebraic expression of the lattice gauge transporter, shown in Fig. 1.3, is given below

$$P(U) = U_x(x)\; U_z(x + a\hat{x})\; U_y(x + a\hat{x} + a\hat{z}) \cdots U_x(x + 2a\hat{x} + 2a\hat{y} + 2a\hat{z})\,. \quad (1.33)$$

The ellipsis are used to indicate the remaining links which are not explicitly shown for notational convenience. Applying a gauge transformation to Eq. (1.33) yields

$$\begin{aligned} P(U') &= \Omega(x)U_x(x)\mathbb{1}U_z(x + a\hat{x})\mathbb{1}U_y(x + a\hat{x} + a\hat{z})\mathbb{1}\cdots \\ &\quad \cdots \mathbb{1}U_x(x + 2a\hat{x} + 2a\hat{y} + 2a\hat{z})\Omega(y) \\ &= \Omega(x)P_U\Omega(y)^\dagger\,, \end{aligned} \quad (1.34)$$

A whole class of gauge invariant objects can be constructed by forming a closed loop

$$P_{\text{closed}}(U') = \text{Tr}\left[\Omega(x)P_{\text{closed}}(U)\Omega(x)^\dagger\right] = P_{\text{closed}}(U)\,. \quad (1.35)$$

1.7 Naive fermion action

The definition of local gauge invariance within the lattice framework is similar to the continuum formulation. Lattice spinors transform according to

$$\Psi(x) \to \Psi'(x) = \Omega(x)\,\Psi(x)\,, \quad (1.36a)$$

$$\overline{\Psi}(x) \to \overline{\Psi}'(x) = \overline{\Psi}(x)\,\Omega^\dagger(x)\,, \quad (1.36b)$$

with $\Omega(x) \in \text{SU}(3)$. Applying these transformations to the mass term in Eq. (1.29) yields an extra term

$$\frac{\overline{\Psi}(x)\,\Omega^\dagger(x)\,\Omega(x + a\hat{\mu})\,\Psi(x + a\hat{\mu}) - \overline{\Psi}(x)\,\Omega^\dagger(x)\,\Omega(x - a\hat{\mu})\,\Psi(x - a\hat{\mu})}{2a}\,,$$

which breaks gauge invariance. This can be fixed by a proper usage of the gauge links introduced in the last section. A gauge invariant fermion action, according to the transformations defined in Eqs. (1.36a, 1.36b, 1.32), is given by

$$S_F^\Lambda\left[U, \Psi, \overline{\Psi}\right] = a^4 \sum_{x\in\Lambda} \overline{\Psi}(x) \left(\sum_{\mu=1}^{4} \gamma_\mu \frac{U_\mu(x)\Psi(x + a\hat{\mu}) - U_{-\mu}(x)\Psi(x - a\hat{\mu})}{2a} + m\Psi(x) \right) \quad (1.37)$$

This action approaches the continuum formulation in the limit of $a \to 0$ which can be shown by a Taylor expansion of Eq. (1.31) [9]

$$U_\mu(x) = \mathbb{1} + \mathrm{i}\mathcal{A}_\mu(x)a + \mathcal{O}(a), \qquad U_{-\mu}(x) = \mathbb{1} + \mathrm{i}\mathcal{A}_\mu(x - a\hat{\mu})a + \mathcal{O}(a)\,,$$

where we used $\mathcal{A}_\mu = \mathcal{A}_\mu^\dagger$. Substituting this expression into Eq. (1.37) yields

$$S_F^\Lambda\left[\mathcal{A},\Psi,\overline{\Psi}\right] = S_F^\Lambda\left[\mathcal{A}=0,\Psi,\overline{\Psi}\right] + S_F^\Lambda\left[\mathcal{A},\Psi,\overline{\Psi}\right] + \mathcal{O}(a)\,. \tag{1.38}$$

The first term on the right hand side is the free fermionic continuum action

$$S_F\left[\mathcal{A}=0\,,\Psi\,,\overline{\Psi}\,\right] = \int \mathrm{d}^4x\Big[\overline{\Psi}(x)\;(\gamma_\mu\partial_\mu + m)\;\Psi(x)\Big]\,. \tag{1.39}$$

The second term describes the interaction with the gauge field

$$\begin{aligned} S_F^\Lambda\left[\mathcal{A},\Psi,\overline{\Psi}\right] &= \frac{\mathrm{i}}{2}a^4\sum_{x\in\Lambda}\sum_{\mu=1}^{4}\overline{\Psi}(x)\gamma_\mu\Big(\mathcal{A}_\mu(x)\Psi(x+a\hat{\mu}) + \mathcal{A}_\mu(x-a\hat{\mu})\Psi(x-a\hat{\mu})\Big) \\ &= \mathrm{i}a^4\sum_{x\in\Lambda}\sum_{\mu=1}^{4}\overline{\Psi}(x)\gamma_\mu\mathcal{A}_\mu(x)\Psi(x) \\ &= \int \mathrm{d}^4x\overline{\Psi}(x)\mathrm{i}\gamma_\mu\mathcal{A}_\mu(x)\Psi(x)\,, \end{aligned} \tag{1.40}$$

where we used the following approximations in the second step

$$\Psi(x\pm a\hat{\mu}) = \Psi(x) + \mathcal{O}(a)\,, \qquad \mathcal{A}_\mu(x-a\hat{\mu}) = \mathcal{A}_\mu(x) + \mathcal{O}(a)\,. \tag{1.41}$$

Substituting Eq. (1.40) and Eq. (1.39) into the right hand side of Eq. (1.38) yields

$$\begin{aligned} S_F\left[\mathcal{A}\,,\Psi\,,\overline{\Psi}\,\right] &= \int \mathrm{d}^4x\overline{\Psi}(x)\Big[\gamma_\mu\partial_\mu + m + \mathrm{i}\gamma_\mu\mathcal{A}_\mu(x)\Big]\Psi(x) \\ &= \int \mathrm{d}^4x\overline{\Psi}(x)\Big[\gamma_\mu\mathrm{D}_\mu + m\Big]\Psi(x)\,. \end{aligned} \tag{1.42}$$

which proves that the continuum action is restored in the in the limit $a \to 0$. Note that Eq. (1.37) can be written as

$$S_F^N\left[U,\Psi,\overline{\Psi}\right] = a^4\sum_{m,n\in\Lambda}\sum_{\alpha\beta}\sum_{ab}\overline{\Psi}(n)_a^\alpha\, D_N(n|m)_{ab}^{\alpha\beta}\,\Psi(m)_b^\beta\,, \tag{1.43}$$

with the naive Dirac operator

$$D_N(n|m)_{ab}^{\alpha\beta} = \sum_{\mu=1}^{4}(\gamma_\mu)_{\alpha\beta}\frac{U_\mu(n)_{ab}\delta_{n+\hat{\mu},m} - U_{-\mu}(n)_{ab}\delta_{n-\hat{\mu},m}}{2a} + m\delta_{\alpha\beta}\delta_{ab}\delta_{nm}\,, \tag{1.44}$$

which is a compact and common notation in lattice QCD. In this step we substitute $\Lambda \to N$ to indicate the type of the lattice action.

1.8 Fermion doubling

The naive fermion action introduced previously has a serious drawback because it yields non-physical degrees of freedom, called doublers. To examine this phenomena we follow [9] and compute the Fourier transform of Eq. (1.44) for the free case $U = 1$, to obtain the lattice Dirac operator in momentum space

$$\tilde{D}(p) = m + \frac{\mathrm{i}}{a} \sum_{\mu=1}^{4} \gamma_\mu \sin(p_\mu a) \,. \tag{1.45}$$

The operator in Eq. (1.45) has the following inverse [9]

$$\tilde{D}^{-1}(p) = \frac{m - \mathrm{i} a^{-1} \sum_\mu \gamma_\mu \sin(p_\mu a)}{m^2 + a^{-2} \sum_\mu \sin(p_\mu a)^2} \,, \tag{1.46}$$

providing the basis for the following discussion. We consider the massless, free continuum quark propagator. It is obtained from Eq. (1.46), in the limit $a \to 0$ while physical momentum is kept fixed

$$\tilde{D}^{-1}_{m=0}(p) = \frac{-\mathrm{i} a^{-1} \sum_\mu \gamma_\mu \sin(p_\mu a)}{+a^{-2} \sum_\mu \sin(p_\mu a)^2} \xrightarrow{a \to 0} -\mathrm{i} \sum_\mu \frac{\gamma_\mu p_\mu}{p^2} \tag{1.47}$$

As expected, we obtain the free continuum propagator in momentum space, which has exactly on pole for $p = (0, 0, 0, 0)$. This is in contrast to the free lattice propagator in momentum space, which has in addition 15 (unphysical) poles (c.f. Eq. (1.46)). For instance, at $p_{\text{pole}} = (\pi/a, \pi/a, \pi/a, \pi/a)$.

1.9 Wilson fermions

In [10] Wilson demonstrated a solution to the fermion doubling problem. He proposed to add an additional term to the fermion action which vanishes in the continuum limit but removes the doublers for non-vanishing values of a. How this works can be understood best in momentum space [9]. To that end, one considers a modified version of Eq. (1.45)

$$\tilde{D}(p) = m + \frac{\mathrm{i}}{a} \sum_{\mu=1}^{4} \gamma_\mu \sin(p_\mu a) + \frac{1}{a} \sum_{\mu=1}^{4} (1 - \gamma_\mu \cos(p_\mu a)) \,. \tag{1.48}$$

The additional term vanishes for $p_\mu = (0,0,0,0)$ and yield extra mass contributions for the doublers, parametrized by

$$m_{\text{doubler}} = m + \frac{l}{a}\,,$$

where l denotes the number of p_μ components with $p_\mu = \frac{\pi}{a}$. The term $\frac{l}{a}$ becomes large in the limit $a \to 0$ and thus decouples the doublers from the theory. The operator in position space is obtained via inverse Fourier transformation, applied after the inversion of Eq. (1.48). To make this operator gauge invariant one needs to introduce suitable[1] gauge links. This yields the Wilson's Dirac operator

$$D(n|m)^{\alpha\beta}_{ab} = (m + \frac{4}{a})\delta_{\alpha\beta}\delta_{ab}\delta_{nm} - \frac{1}{2a}\sum_{\mu=\pm1}^{\pm4}(\mathbb{1} - \gamma_\mu)_{\alpha\beta}U_\mu(n)_{ab}\delta_{n+\hat{\mu},m} \tag{1.49}$$

where we define $\gamma_{-\mu} = -\gamma_\mu$. This operator obeys the following relation,

$$D(n|m)^\dagger = \gamma_5 D(m|n)\gamma_5\,, \tag{1.50}$$

known as γ_5-hermiticity. It can be used to show that the eigenvalues of D are either real or come in complex-conjugate pairs which implies that the determinate of D must be real. This is an important requirement for Monte-Carlo simulations. However, also this discretized action is not perfect. While it is doubler-free by construction it explicitly breaks chiral symmetry on the lattice[2]. In case that chiral symmetry is of crucial importance, one has to consider a generalization of chiral symmetry on the lattice by means of the Ginsparg-Wilson relation [14].

1.10 Discretization of the gluonic part

In this section we construct the Wilson gauge action [1, 9]. Again, we require that the discretized action is invariant under local gauge transformations and shall recover the continuum action in the limit $a \to 0$. To this end we define an object called plaquette

$$U_{\mu\nu}(x) = U_\mu(x)\,U_\nu(x + a\hat{\mu})\,U^\dagger_{-\mu}(x + a\hat{\nu})\,U^\dagger_{-\nu}(x) \tag{1.51}$$

and illustrate it in Fig. 1.4. This object is gauge invariant by construction since it is a closed string of lattice gauge links. The plaquette can be connected to the continuum

[1] More information can be found in [9].

[2] This follows from the no-go theorem by Nielsen and Ninomiya [11, 12, 13]

field strength tensor by[3]

$$U_{\mu\nu}(x) = \exp\left(\mathrm{i}\, a^2 \mathrm{F}_{\mu\nu}(x) + \mathcal{O}(a^3)\right), \tag{1.52}$$

and it used to define the Wilson gauge action

$$S_G^{\Lambda}[U] \equiv \frac{\beta}{3} \sum_{x\in\Lambda} \sum_{\mu<\nu} \mathrm{Re}\ \mathrm{Tr}\left[\mathbb{1} - U_{\mu\nu}(x)\right]. \tag{1.53}$$

The summation over indices μ and ν is restricted to $\mu < \nu$ which reflects that only one orientation per plaquette contributes. The real-valued parameter β is a function of the bare coupling and given by $\beta = 6/g^2$. In the limit of $a \to 0$ this action reproduces the continuum action. This can be seen by inserting the Taylor expansion of Equation (1.52) into Eq. (1.53) which yields [9]

$$\begin{aligned} S_G^{\Lambda}[U] \xrightarrow{a\to 0} & \frac{1}{2g^2} a^4 \sum_{n\in\Lambda} \sum_{\mu\nu} \mathrm{Tr}\left[\mathrm{F}_{\mu\nu}(an)\mathrm{F}_{\mu\nu}(an)\right] + \mathcal{O}(a^2) = \\ & \frac{1}{2g^2} \int \mathrm{d}^4x\ \mathrm{Tr}\left[\mathrm{F}_{\mu\nu}(x)\mathrm{F}_{\mu\nu}(x)\right] + \mathcal{O}(a^2) = \\ & \frac{1}{4g^2} \int \mathrm{d}^4x F^A_{\mu\nu}(x) F^A_{\mu\nu}(x) + \mathcal{O}(a^2) = \\ & \frac{1}{4} \int \mathrm{d}^4x F^A_{\mu\nu}(x) F^A_{\mu\nu}(x) + \mathcal{O}(a^2)\,. \end{aligned} \tag{1.54}$$

In the last step we absorbed the coupling into the definition of the gauge fields.

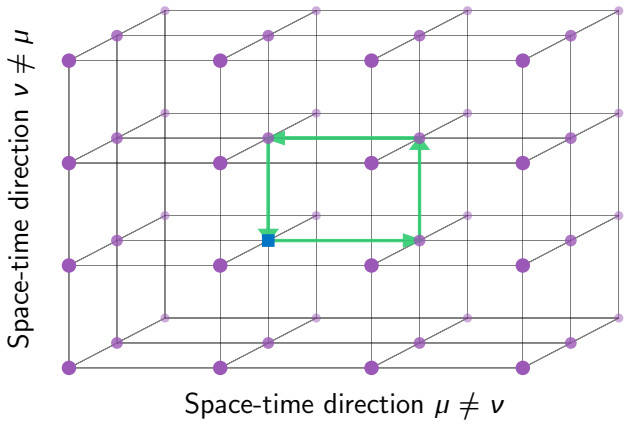

Figure 1.4: Graphical representation of a plaquette $U_{\mu\nu}(x)$. The lattice site $x = an$ is shown in blue.

[3] More details can be found in [9].

1.11 Clover Wilson Fermion

The clover fermion action is an $\mathcal{O}(a)$-improved version of the Wilson quark action. By adding

$$S_F^{\Lambda\,\mathrm{sw}}\left[U,\Psi,\overline{\Psi}\right] = c_{\mathrm{sw}}a^5\sum_{x\in\Lambda}\sum_{\mu<\nu}\overline{\Psi}(x)\,\frac{1}{2}\sigma_{\mu\nu}\hat{F}_{\mu\nu}(x)\Psi(x) \tag{1.55}$$

to the Wilson action in Eq. (1.49) one can eliminate the $\mathcal{O}(a)$ errors brought by the Wilson term while keeping the doublers away. The Sheikholeslami-Wohlert coefficient c_{sw} is a real valued function of the bare coupling g_0 and needs to be determined numerically. $\hat{F}_{\mu\nu}$ is a lattice version of the field strength tensor. Its definition is not unique, but a common choice is [9]

$$\hat{F}_{\mu\nu}(x) = -\mathrm{i}\frac{Q_{\mu\nu}(x) - Q_{\nu\mu}(x)}{8a^2} \tag{1.56}$$

where the $Q_{\mu\nu}(x)$ is the sum of plaquettes.

$$Q_{\mu\nu}(x) = U_{\mu\nu}(x) + U_{\nu-\mu}(x) + U_{-\mu-\nu}(x) + U_{-\nu-\mu}(x)\,. \tag{1.57}$$

$Q_{\mu\nu}(x)$ is the so-called clover term. A graphical representation is given in Fig. 1.5.

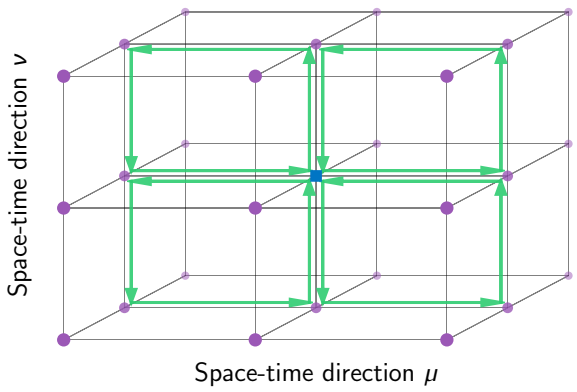

Figure 1.5: The clover term $Q_{\mu\nu}(x)$. The blue site represents x.

1.12 Fermionic expectation values

So far, we introduced fermionic fields $\Psi_f(x)^\alpha_a$ to describe spin 1/2 quark fields. These fields are complex valued Grassmann number, i.e., they anti-commute which is closely related to the he Pauli exclusion principle. It states, that two identical fermions can not occupy the same quantum state. This requirement is implemented by a Grassmann algebra [15] over the complex numbers which is an associative algebra generated by

a set of generators θ_i with $i \in \{1 \dots N_g\}$ that satisfy the anti-commutation relations

$$\theta_i \theta_j = -\theta_j \theta_i \,. \tag{1.58}$$

In essence, this gives rise to the following rules for fermionic fields [9]

$$\Psi_{f_1}(x_1)^{\alpha_1}_{a_1} \, \Psi_{f_2}(x_2)^{\alpha_2}_{a_2} = -\Psi_{f_2}(x_2)^{\alpha_2}_{a_2} \, \Psi_{f_1}(x_1)^{\alpha_1}_{a_1} \tag{1.59a}$$

$$\overline{\Psi}_{f_1}(x_1)^{\alpha_1}_{a_1} \, \Psi_{f_2}(x_2)^{\alpha_2}_{a_2} = -\Psi_{f_2}(x_2)^{\alpha_2}_{a_2} \, \overline{\Psi}_{f_1}(x_1)^{\alpha_1}_{a_1} \tag{1.59b}$$

$$\overline{\Psi}_{f_1}(x_1)^{\alpha_1}_{a_1} \, \overline{\Psi}_{f_2}(x_2)^{\alpha_2}_{a_2} = -\overline{\Psi}_{f_2}(x_2)^{\alpha_2}_{a_2} \, \overline{\Psi}_{f_1}(x_1)^{\alpha_1}_{a_1} \tag{1.59c}$$

Beside these simple rules one can establish differential and integral calculus on Grassmann numbers. This however, is not discussed here, it can be found in [9]. For our purpose, it is sufficient to use the results. We are interested in fermionic expectation values, formulated within the path integral formalism

$$\left\langle \Psi_{f_1}(x_1)^{\alpha_1}_{a_1} \dots \Psi_{f_k}(x_2)^{\alpha_k}_{a_k} \dots \overline{\Psi}_{g_1}(y_1)^{\beta_1}_{b_1} \dots \overline{\Psi}_{g_k}(y_2)^{\beta_k}_{b_k} \right\rangle = \frac{\int \mathcal{D}\left[\, U, \Psi, \overline{\Psi} \,\right] \left(\Psi_{f_1}(x_1)^{\alpha_1}_{a_1} \dots \Psi_{f_k}(x_2)^{\alpha_k}_{a_k} \dots \overline{\Psi}_{g_1}(y_1)^{\beta_1}_{b_1} \dots \overline{\Psi}_{g_k}(y_2)^{\beta_k}_{b_k} \right) \mathrm{e}^{\overline{\Psi} \cdot D[U] \cdot \Psi - S_G[U]}}{\mathcal{Z}} \,.$$

In this expression we introduced the fermion matrix D, which is an abbreviation for the discretized Dirac operator (cf. Eq. (1.49)). For further simplicity, we only consider a single quark flavor. Note that the gluonic degrees of freedom are given in terms of the gauge links U. With $S_G[U]$ we denote the discretized version of the gluonic action (cf. Eq. (1.53)). Applying the rules of Grassmann integration and Wick's theorem [9] we can integrate out the fermionic degrees of freedom which yields

$$\left\langle \Psi_{f_1}(x_1)^{\alpha_1}_{a_1} \dots \Psi_{f_k}(x_2)^{\alpha_k}_{a_k} \dots \overline{\Psi}_{g_1}(y_1)^{\beta_1}_{b_1} \dots \overline{\Psi}_{g_k}(y_2)^{\beta_k}_{b_k} \right\rangle = \frac{\int \mathcal{D}\left[U\right] \left\langle \Psi_{f_1}(x_1)^{\alpha_1}_{a_1} \dots \Psi_{f_k}(x_2)^{\alpha_k}_{a_k} \dots \overline{\Psi}_{g_1}(y_1)^{\beta_1}_{b_1} \dots \overline{\Psi}_{g_k}(y_2)^{\beta_k}_{b_k} \right\rangle_W \det\left(D[U]\right) \mathrm{e}^{-S_G[U]}}{\mathcal{Z}} \,. \tag{1.60}$$

This expression contains the Wick contraction $\langle \dots \rangle_W$. It maps Grassmann valued field operators to a sum of products of quark propagators. A single quark propagator $G[U]$ is by definition just the inverse of the Dirac operator $D[U]$. This object plays a fundamental role because it describes the probability amplitude for a quark. In the most simplest case of two fields the Wick contraction yields

$$\left\langle \Psi_{f_1}(x_1)^{\alpha_1}_{a_1} \, \overline{\Psi}_{g_1}(y_1)^{\beta_1}_{b_1} \right\rangle_W = \delta_{f_1 g_1} \, G_{f_1}[U](x_1, y_1)^{\alpha_1 \beta_1}_{a_1 b_1} \,. \tag{1.61}$$

1.13 Monte Carlo integration

The topic of this section concerns the numerical evaluation of the path integral defined in Eq. (1.60). Therefore, we consider the special case of two[4] fermionic fields

$$\left\langle \Psi_F(x_1)^{\alpha_1}_{a_1}\overline{\Psi}_F(y_1)^{\beta_1}_{b_1}\right\rangle = \frac{1}{\mathcal{Z}}\int \mathcal{D}\left[U\right]\left\langle \Psi_F(x_1)^{\alpha_1}_{a_1}\overline{\Psi}_F(y_1)^{\beta_1}_{b_1}\right\rangle_W \det\left(D[U]\right)\mathrm{e}^{-S_G[U]} = \frac{1}{\mathcal{Z}}\int \mathcal{D}\left[U\right]\, G_F[U](x_1,y_1)^{\alpha_1\beta_1}_{a_1b_1}\det\left(D[U]\right)\mathrm{e}^{-S_G[U]}. \tag{1.62}$$

Here, one can use, the discretized versions of the actions. However, the dimensionality is far too large for a direct evaluation. The number of integration variables is $4\times N_S\times N_T\times 8$. The factor 8 originates from the gauge links, which are 3×3 matrices, with 8 independent real components. High dimensional integrals are usually estimated by means of Monte Carlo techniques. The basic idea is as follows

$$\begin{aligned}\left\langle \Psi_F(x_1)^{\alpha_1}_{a_1}\overline{\Psi}_F(y_1)^{\beta_1}_{b_1}\right\rangle &= \frac{1}{\mathcal{Z}}\int \mathcal{D}\left[U\right]\, G_F[U](x_1,y_1)^{\alpha_1\beta_1}_{a_1b_1}\det\left(D[U]\right)\mathrm{e}^{-S_G[U]}\\ &\approx \frac{1}{N_{\text{conf}}}\sum_{n=1}^{N_{\text{conf}}}\det\left(D[U_n]\right)\mathrm{e}^{-S_G[U_n]}\, G_F[U_n](x_1,y_1)^{\alpha_1\beta_1}_{a_1b_1}\\ &\approx \frac{1}{N_{\text{conf}}}\sum_{\substack{U_n \text{ with}\\ \text{probability}\propto\\ \det\left(D[U_n]\right)\exp\left(-S_G[U_n]\right)}} G_F[U_n](x_1,y_1)^{\alpha_1\beta_1}_{a_1b_1}\end{aligned} \tag{1.63}$$

Using this ansatz, one can expect an error term which is proportional to $\mathcal{O}(N_{\text{conf}}^{-\frac{1}{2}})$. This however, is only valid if the generated configurations (U_n) are sampled from the equilibrium distribution. The time spent to reach this point is called thermalization time. Further important details have their origin in the fermion determinant. Usually, it is required to be positive definite to allow for a statistical interpretation. While this is the case for Wilson fermions, there are other situations giving rise to a complex determinant. For instance, if a non-zero chemical potential is considered. Problems of that type, are usually referred to as the sign problem, an unsolved problem and thus a topic of active research. We remark, that nowadays the determinant is included in the probability weight. This is referred to as dynamical simulation, in contrast to the quenched approximation, where the determinant is set to one. The standard algorithm for dynamical simulations it the Hybrid Monte Carlo (HMC) algorithm [16]. This algorithm, includes the determinant, but not directly because it is infeasible since the cost is proportional to $\mathcal{O}((N_S N_T N_c N_s)^3)$. However, one can reformulate the action as shown in [17]. This circumvents the evaluation of the determinant by converting fermion integrals to equivalent integrals over effective boson degrees of freedom. In

[4] A generalization to more than two fields is straight forward.

case of lattice QCD, with two flavors of degenerate Wilson fermions, one obtains

$$\det\left(D^\dagger D\right) \propto \int \mathcal{D}\left[\phi\,,\phi^\dagger\right] \mathrm{e}^{-|D^{-1}\phi|^2} \tag{1.64}$$

The auxiliary fields ϕ are called pseudo-fermions and have the same degrees of freedom as their fermionic counterparts. The action of this theory

$$S[U\,,\phi] = S_G[U] + |D^{-1}\phi|^2 \tag{1.65}$$

An important detail in Eq. (1.65) is that it contains the inverse of the Dirac operator, yielding a non-local problem. In the following, we assume, that the necessary gauge configurations are provided and refer the interested reader to [9, 18, 19] for more details about HMC.

1.14 Point-to-all propagator

After the generation of gauge configurations U_n, one can start to measure physics on them. In this section we discuss the calculation of quark propagators, the building blocks for many lattice QCD calculations. The theoretical basis, introduced previously, is the expectation value for fermionic operators as shown in Eq. (1.63). It requires the inversion of large matrices, a common problem in lattice QCD. In particular, one is confronted with

$$G[U_n]_F(x',x)^{\alpha'\alpha}_{a'b} \equiv D[U_n]_F^{-1}(x',x)^{\alpha'\alpha}_{a'b}\,. \tag{1.66}$$

In general, this does not raise a problem as long as the condition number[5] of $D[U_n]$ is well-behaved and the dimension of the matrix is not too large. However, in lattice QCD one faces $(N_S \times N_T \times N_s \times N_c)^2$ matrix elements. This expression contains the spatial volume of the lattice (N_S), the temporal extent (N_T), the number of spin indices ($N_s = 4$) as well as the number of color indices ($N_c = 3$). Even for medium-sized lattices, a full inversion is not feasible. Fortunately, for most applications, it is sufficient to invert only a single column of the Dirac operator, justified by translational invariance. One considers source objects, in the simplest case, a point source,

$$\eta(x,x_0)^{\beta\beta_0}_{bb_0} \equiv \delta_{xx_0}\delta_{\beta\beta_0}\delta_{bb_0}\,, \tag{1.67}$$

where the spatial component of x_0 is randomly chosen. The actual value of the temporal component must be defined, but it depends on the considered problem. The point source can be used to define a relation between the point-to-all propagator and

[5] For lighter quark masses the condition number grows.

the all-to-all propagator

$$\underbrace{D[U_n]_F^{-1}(x', x_0)_{ab_0}^{\alpha\beta_0}}_{\text{point-to-all prop.}} = \underbrace{D[U_n]_F^{-1}(x', x)_{ab}^{\alpha\beta}}_{\text{all-to-all prop.}} \cdot \eta(x, x_0)_{bb_0}^{\beta\beta_0}. \tag{1.68}$$

Applying the Dirac operator $D[U_n]_F(y', x')_{a'a}^{\alpha'\alpha}$ from the left to Eq. (1.68) yields

$$\underbrace{D[U_n]_F(y', x')_{a'a}^{\alpha'\alpha}}_{A} \cdot \underbrace{D[U_n]_F^{-1}(x', x_0)_{ab_0}^{\alpha\beta_0}}_{\phi(x_0)^{(\beta_0\, b_0)}} = \underbrace{\eta(y', x_0)_{a'b_0}^{\alpha'\beta_0}}_{\eta(x_0)^{(\beta_0\, b_0)}}. \tag{1.69}$$

This equation is of the general form

$$A \cdot \phi(x_0)^{(\beta_0\, b_0)} = \eta(x_0)^{(\beta_0\, b_0)}. \tag{1.70}$$

For a fixed space-time position x_0, Eq. (1.70) must be solved for all twelve combinations of β_0 and b_0 to obtain the solution vectors $\phi(x_0)^{(\beta_0\, b_0)}$. Note that A is a sparse matrix, i.e., most matrix elements are zero. Depending on the symmetries[6] of A this procedure is numerically feasible. Which solver one uses depends on the problem, for instance on the quark mass. All currently-used solvers are (combinations of) Krylov-subspace methods. An introduction can be found in [9, 18].

1.15 Smearing

A further standard method which is commonly used in lattice QCD calculations is referred to as smearing. It is an attempt to improve the overlap with the physical ground state. This in turn helps to suppress unwanted excited-state contributions. The physical motivation for smearing is the following: Hadrons are not point like objects but have a physical extent. However, this is not reflected by our point-like interpolators. The application of quark smearing increases the overlap of the lattice and continuum wave functions. It produces a spatial distribution around the quark, located on a certain lattice site. In general, one distinguishes between gauge link smearing and quark field smearing. However, in many smearing schemes, both types of smearing are used simultaneously. A concrete example of quark smearing is the gauge covariant Wuppertal smearing [20, 21]. For simplicity, we suppress the flavor index of the quark fields as well as the time and spin indices (smearing is diagonal in time/spin). The m-th smeared quark field $\Psi(\boldsymbol{x})^{(m)}$ located at spatial position $\boldsymbol{x}$ is

[6] Note that the Wilson Dirac operator is not hermitian, which is generally not advantageous. However, one can formulate an equivalent problem for Eq. (1.70) which exploits the γ_5-hermicity symmetry and gives rise to a hermitian operator.

constructed by

$$\Phi(\boldsymbol{x})^{(m)} = \frac{1}{1+6\delta}\left(\Psi(\boldsymbol{x})^{(m-1)} + \delta \sum_{j=\pm 1}^{\pm 3} U(\boldsymbol{x})_j \, \Psi(\boldsymbol{x}+a\boldsymbol{j})^{(m-1)}\right), \quad \boldsymbol{j} = (\delta_{1,j}, \delta_{2,j}, \delta_{3,j}). \tag{1.71}$$

The parameter δ is a positive constant and the arbitrary normalization factor $\frac{1}{1+6\delta}$ is introduced to avoid a numerical overflow for large iteration counts m [22]. The smearing procedure contains the gauge link $U(\boldsymbol{x})_j$, with spatial direction index j. Usually, smeared gauge links are used in this context. For instance, APE smearing [23], which is a commonly used link smearing procedure. The n-th APE smeared gauge link $U(\boldsymbol{x})_j^{(n)}$ is obtained by

$$U(\boldsymbol{x})_i^{(n)} = P_{\mathrm{SU3}}\left(\alpha \, U(\boldsymbol{x})_i^{(n-1)} + \sum_{|j|\neq i}^{3} U(\boldsymbol{x})_j^{(n-1)} \; U(\boldsymbol{x}+a\boldsymbol{j})_i^{(n-1)} U(\boldsymbol{x}+a\boldsymbol{i})_j^{(n-1)\dagger}\right) \tag{1.72}$$

The projection operator P_{SU3} is used to ensure that the smeared gauge links are still elements of the $SU(3)$ gauge group. The smearing parameters, α and δ, must be tuned as well as the number of iteration steps, m and n. The tuning depends on the actual purpose, hence, it can not be discussed here in general.

2

Generalized Form Factor from lattice QCD

In this chapter, based on Ref. [5], results for generalized form factors (GFFs) are presented. GFFs are related to generalized parton distributions (GPDs) which play an important role in the understanding of hadron structure. For instance, GPDs parametrize the transverse coordinate distribution of partons in a fast moving hadron and contain information on how these distributions depend on the parton and hadron spin direction. The theoretical understanding of GPDs and GFFs is well advanced and has already a long history [24, 25, 26, 27, 28, 29, 30]. However, accessing GPDs experimentally is still a hard task, for instance, it is not straight forward to include spin effects in the experimental analysis as demonstrated in [31, 32, 33]. In total there are eight nucleon GPDs, however, some of them are especially important because they provide information on the elusive orbital angular momentum of partons in the nucleon. The physical interpretation of it is not straightforward, because there exist inequivalent definitions of orbital angular momentum [26, 34, 35, 36, 37]. Complementary to experimental efforts, lattice QCD offers an ab initio method to compute quantities which can be used to supplement the understanding of the hadronic structure, for instance [4, 5, 38, 39, 40, 41, 42, 43, 44, 45, 46, 47, 48, 49]. The focus in this work is on nucleon GFFs which are Mellin moments of nucleon GPDs. By computing GFFs and not GPDs one circumvents the problem that GPDs are expressed in terms of bi-local operators which can not be computed directly on a Euclidean lattice.

2.1 Ensemble overview

The computation of GFFs on the lattice is based on the large set of gauge configurations produced by the QCDSF and the RQCD (Regensburg QCD) Collaborations using the standard Wilson gauge action with two mass-degenerate nonperturbatively improved clover fermions. Three different lattice spacings 0.081 fm, 0.071 fm and 0.060 fm are available. The pion masses range from about 490 MeV down to 150 MeV. In terms of Lm_π, values from about 3.4 up to 6.7 are covered. An ensemble overview is presented in Fig. 2.1. A more detailed description can be found in Table A.1.

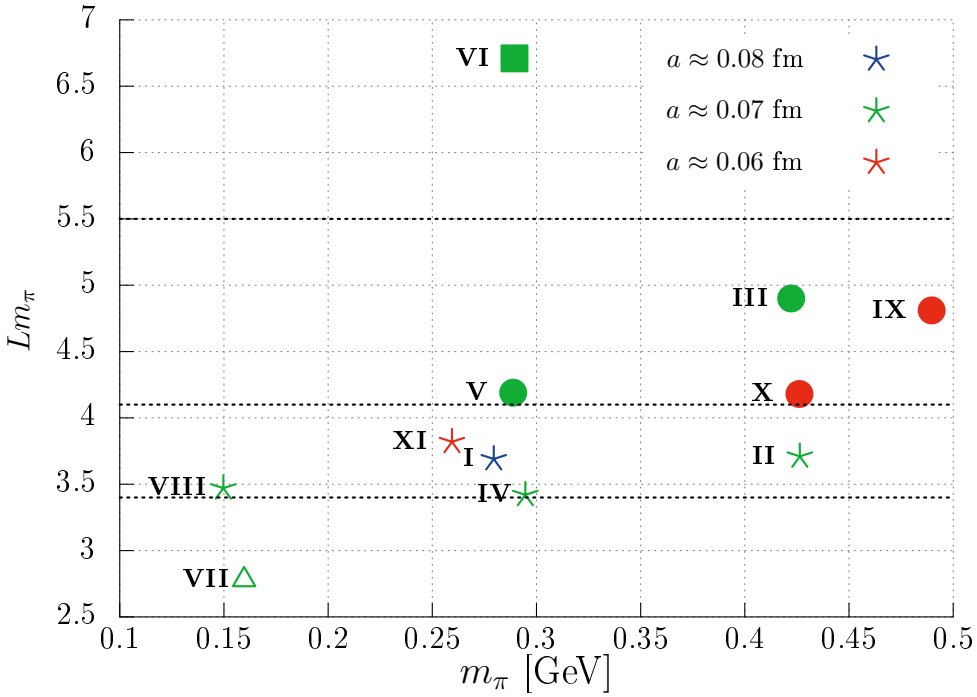

Figure 2.1: Colors encode the lattice spacings and symbols the lattice extents. The horizontal lines separate different volume ranges. Taken from [50].

2.2 Introduction to GPDs and GFFs

GPDs appear in hard exclusive processes such as Deeply Virtual Compton Scattering (DVCS). The corresponding amplitude can be expressed as a convolution of a perturbatively calculable hard-scattering part and the generalized parton distribution functions. The separation into two parts, valid for large photon virtualties, is known as factorization theorem [51]. GPDs parametrize the off-forward nucleon matrix element

$$\mathcal{M}_q^\Gamma(x) = \int_{-\infty}^{\infty} \frac{\mathrm{d}\lambda}{4\pi} e^{i\lambda x} \left\langle N(p',\sigma') | O_q^\Gamma(\lambda) | N(p,\sigma) \right\rangle \tag{2.1}$$

of a bilocal operator with quark flavor q

$$O_q^{\Gamma}(\lambda) = \bar{q}\,(-\lambda n/2)\;\Gamma\;\mathcal{U}_{-\lambda n/2}^{+\lambda n/2}\;q\,(+\lambda n/2)\;. \tag{2.2}$$

The Wilson line $\mathcal{U}$ in Eq. (2.2) connects $-\lambda n/2$ and $+\lambda n/2$ on the light cone ($n^2 = 0$). Depending on the Dirac structure, indicated by the symbol Γ in Eqs. (2.1) and (2.2), one can parametrize the matrix element $\mathcal{M}$ in terms of GPDs. For leading twist these read (see, e.g., Refs. [52, 53]),

$$\mathcal{M}_q^{\gamma^\mu} = \overline{U}(p',\sigma')\left[\begin{pmatrix}\gamma^\mu\\ \frac{i\sigma^{\mu\nu}\Delta_\nu}{2m_N}\end{pmatrix}\cdot\begin{pmatrix}H^q(x,\xi,\mathrm{t})\\ E^q(x,\xi,\mathrm{t})\end{pmatrix}\right]U(p,\sigma)\,, \tag{2.3a}$$

$$\mathcal{M}_q^{\gamma^\mu\gamma_5} = \overline{U}(p',\sigma')\left[\begin{pmatrix}\gamma^\mu\gamma_5\\ \frac{\Delta^\mu\gamma_5}{2m_N}\end{pmatrix}\cdot\begin{pmatrix}\widetilde{H}^q(x,\xi,\mathrm{t})\\ \widetilde{E}^q(x,\xi,\mathrm{t})\end{pmatrix}\right]U(p,\sigma)\,, \tag{2.3b}$$

$$\mathcal{M}_q^{i\sigma^{\mu\nu}} = \overline{U}(p',\sigma')\left[\begin{pmatrix}i\sigma^{\mu\nu}\\ \frac{\gamma^{[\mu}\Delta^{\nu]}}{2m_N}\\ \frac{\overline{p}^{[\mu}\Delta^{\nu]}}{m_N^2}\\ \frac{\gamma^{[\mu}\overline{p}^{\nu]}}{m_N}\end{pmatrix}\cdot\begin{pmatrix}H_T^q(x,\xi,\mathrm{t})\\ E_T^q(x,\xi,\mathrm{t})\\ \widetilde{H}_T^q(x,\xi,\mathrm{t})\\ \widetilde{E}_T^q(x,\xi,\mathrm{t})\end{pmatrix}\right]U(p,\sigma)\,, \tag{2.3c}$$

with $\sigma^{\mu\nu} = i[\gamma^\mu,\gamma^\nu]/2$ and the nucleon spinors $\overline{U}(p',\sigma')$ and $U(p,\sigma)$. The GPDs, e.g., H^q and E^q, and the corresponding tensor structures γ^μ and $i\sigma^{\mu\nu}\Delta_\nu/(2m_N)$ are written as vectors, where we apply a standard scalar product. We further introduce the kinematic variables $\Delta \equiv p' - p$ and $\overline{p} \equiv (p'+p)/2$ as well as the nucleon mass m_N. The antisymmetrization of indices is denoted by $[\ldots]$, e.g.,

$$B^{[\mu}C^{\nu]} \equiv \mathrm{A}_{\mu\nu}B^\mu C^\nu \equiv B^\mu C^\nu - C^\nu B^\mu\,.$$

The eight introduced generalized parton distribution functions, H^q, E^q, $\widetilde{H}^q$, $\widetilde{E}^q$ H_T^q, E_T^q, $\widetilde{H}_T^q$ and $\widetilde{E}_T^q$ are real functions of the three variables x, ξ and t. The total momentum transfer squared t is given by $\mathrm{t} \equiv \Delta^2 \leq 0$ and it is related to the virtuality $Q^2 = -\mathrm{t}$. The longitudinal momentum fraction x varies between -1 and 1 and the skewness $\xi \equiv -n\cdot\Delta/2$ between 0 and 1. In physical terms (for $|x| > \xi$) GPDs parametrize the probability amplitude for a hadron to stay intact if a parton is removed at the light cone point $-\lambda/2$ and replaced by a parton with different momentum at light cone time $\lambda/2$. For a more detailed discussion we refer the reader to Refs. [29, 30, 52, 53, 54, 55].

The four GPDs H^q, E^q, $\widetilde{H}^q$ and $\widetilde{E}^q$ are referred as quark-helicity conserving GPDs. H^q and E^q are also known as unpolarized GPDs in contrast to the polarized GPDs $\widetilde{H}^q$ and $\widetilde{E}^q$. The remaining four GPDs H_T^q, E_T^q, $\widetilde{H}_T^q$ and $\widetilde{E}_T^q$ are quark-helicity flip GPDs. They provide essential information on the transverse spin structure of the nucleon. An analogous set of gluonic GPDs exists, however, we do not address it here. As already mentioned in the introduction of this chapter, we can not compute

GPDs directly on the Euclidean lattice because the light cone loses its meaning. However, the operator product expansion (OPE) relates Mellin moments of GPDs to local matrix elements that are amenable to lattice calculation. For H^q and E^q, for instance, these x-moments read (see, e.g., Refs. [53, 52])

$$\int_{-1}^{+1} \mathrm{d}x\, x^{n-1}\, H^q(x,\xi,\mathrm{t}) = \sum_{i=0,\,\mathrm{even}}^{n-1} (-2\xi)^i A^q_{ni}(\mathrm{t}) + (-2\xi)^n\, C^q_{n0}(\mathrm{t})|_{n=\mathrm{even}}\,, \tag{2.4a}$$

$$\int_{-1}^{+1} \mathrm{d}x\, x^{n-1}\, E^q(x,\xi,\mathrm{t}) = \sum_{i=0,\,\mathrm{even}}^{n-1} (-2\xi)^i B^q_{ni}(\mathrm{t}) - (-2\xi)^n\, C^q_{n0}(\mathrm{t})|_{n=\mathrm{even}}\,, \tag{2.4b}$$

where the real functions $A^q(\mathrm{t})$, $B^q(\mathrm{t})$ and $C^q(\mathrm{t})$ in the ξ-expansion on the rhs are the GFFs. In principle one can determine Mellin moments of GPDs for any n on the lattice, in practice one is restricted to the lowest few n. The reason for this restriction is twofold. On the one hand, the signal to noise ratio becomes worse for an increasing number of covariant derivatives. On the other hand as n increases, mixing with lower-dimensional operators will take place, resulting in divergences that are powers of the inverse lattice spacing a^{-1}. In this study, we focus on the case $n = 2$, where such mixing does not occur. The desired GFFs are extracted from lattice calculations of two- and three-point correlation functions where the currents are the local twist-2 operators,

$$\mathcal{O}^{\mu\nu}_{V,q}(z) = \mathrm{S}_{\mu\nu}\, \bar{q}(z)\, \gamma^\mu i \overleftrightarrow{D}^\nu q(z)\,, \tag{2.5a}$$

$$\mathcal{O}^{\mu\nu}_{A,q}(z) = \mathrm{S}_{\mu\nu}\, \bar{q}(z)\, \gamma^\mu \gamma_5 i \overleftrightarrow{D}^\nu q(z)\,, \tag{2.5b}$$

$$\mathcal{O}^{\mu\nu\rho}_{T,q}(z) = \mathrm{A}_{\mu\nu}\mathrm{S}_{\nu\rho}\, \bar{q}(z) i\sigma^{\mu\nu} i \overleftrightarrow{D}^\rho q(z)\,. \tag{2.5c}$$

Here, $\mathrm{S}_{\mu\nu}$ and $\mathrm{A}_{\mu\nu}$ denote symmetrization (also subtracting traces and dividing by $n!$ for n indices) and antisymmetrization operators, respectively, and

$$\overleftrightarrow{D}_\mu \equiv \frac{1}{2}(\overrightarrow{D}_\mu - \overleftarrow{D}_\mu) \tag{2.6}$$

is the symmetric covariant derivative. In the continuum we can decompose the matrix elements

$$\left\langle N(p',\sigma')|\mathcal{O}^{\mu\nu}_{V,q}|N(p,\sigma)\right\rangle = \overline{U}(p',\sigma')\mathbb{D}^{\mu\nu}_{V,q} U(p,\sigma)\,, \tag{2.7a}$$

$$\left\langle N(p',\sigma')|\mathcal{O}^{\mu\nu}_{A,q}|N(p,\sigma)\right\rangle = \overline{U}(p',\sigma')\mathbb{D}^{\mu\nu}_{A,q} U(p,\sigma)\,, \tag{2.7b}$$

$$\left\langle N(p',\sigma')|\mathcal{O}^{\mu\nu\rho}_{T,q}|N(p,\sigma)\right\rangle = \overline{U}(p',\sigma')\mathbb{D}^{\mu\nu\rho}_{T,q} U(p,\sigma)\,, \tag{2.7c}$$

with the nucleon four-momentum $(p^\mu) = (E_N(\boldsymbol{p}), \boldsymbol{p})$. The desired GFFs are contained

in the Dirac structures,

$$\mathbb{D}^{\mu\nu}_{V,q} = S_{\mu\nu} \begin{pmatrix} \gamma^\mu \overline{p}^\nu \\ i\sigma^{\mu\rho}\Delta_\rho \overline{p}^\nu/(2m_N) \\ \Delta^\mu \Delta^\nu/m_N \end{pmatrix} \cdot \begin{pmatrix} A^q_{20} \\ B^q_{20} \\ C^q_{20} \end{pmatrix} , \tag{2.8a}$$

$$\mathbb{D}^{\mu\nu}_{A,q} = S_{\mu\nu} \begin{pmatrix} \gamma^\mu \gamma^5 \overline{p}^\nu \\ \gamma_5 \Delta^\mu \overline{p}^\nu/(2m_N) \end{pmatrix} \cdot \begin{pmatrix} \widetilde{A}^q_{20} \\ \widetilde{B}^q_{20} \end{pmatrix} , \tag{2.8b}$$

$$\mathbb{D}^{\mu\nu\rho}_{T,q} = A_{\mu\nu} S_{\nu\rho} \begin{pmatrix} i\sigma^{\mu\nu}\overline{p}^\rho \\ \gamma^{[\mu}\Delta^{\nu]}\overline{p}^\rho/(2m_N) \\ \overline{p}^{[\mu}\Delta^{\nu]}\overline{p}^\rho/m_N^2 \\ \gamma^{[\mu}\overline{p}^{\nu]}\Delta^\rho/m_N \end{pmatrix} \cdot \begin{pmatrix} A^q_{T20} \\ B^q_{T20} \\ \widetilde{A}^q_{T20} \\ \widetilde{B}_{T21} \end{pmatrix} . \tag{2.8c}$$

2.3 Lattice two- and three-point functions

The GFFs shown in the rhs of Eqs. (2.8) are extracted from combinations of hadronic two- and three-point correlation functions in Euclidean space-time. The two-point function reads

$$C(t', \boldsymbol{p}')^{\tau'\tau} = \left\langle \sum_{\boldsymbol{x}'} \left\langle \mathcal{N}(t', \boldsymbol{x}')^{\tau'} \overline{\mathcal{N}}(0, \boldsymbol{0})^{\tau} \right\rangle_W e^{-i\boldsymbol{p}'\cdot\boldsymbol{x}'} \right\rangle \tag{2.9}$$

where the big brackets $\langle \ldots \rangle$ are used to denote the ensemble average and $\langle \ldots \rangle_W$ indicates the Wick contraction of the Grassmann valued nucleon annihilation and creation interpolators $\mathcal{N}$ and $\overline{\mathcal{N}}$

$$\mathcal{N}(t, \boldsymbol{x})^{\tau'} = \varepsilon_{abc}\, u_a^{\tau'}(t, \boldsymbol{x}) \Big[u_b(t, \boldsymbol{x})^{\mathsf{T}}\, C\, \gamma_5\, d_c(t, \boldsymbol{x}) \Big], \tag{2.10a}$$

$$\overline{\mathcal{N}}(t, \boldsymbol{x})^{\tau} = \varepsilon_{abc} \Big[\bar{u}_b(t, \boldsymbol{x})\, C\gamma_5\, \bar{d}_c(t, \boldsymbol{x})^{\mathsf{T}} \Big] \bar{u}_a^{\tau}(t, \boldsymbol{x}) , \tag{2.10b}$$

containing appropriate combinations of u and d (anti)quark fields and the charge conjugation matrix C. The lattice three-point function is given by

$$C(\tau, t', \boldsymbol{p}', \boldsymbol{p})^{\tau'\tau} = \left\langle \sum_{\boldsymbol{x}'\boldsymbol{z}} \left\langle \mathcal{N}(t', \boldsymbol{x}')^{\tau'}\, \mathcal{O}(\tau, \boldsymbol{z})\, \overline{\mathcal{N}}(0, \boldsymbol{0})^{\tau} \right\rangle_W e^{-i\boldsymbol{p}'\cdot\boldsymbol{x}'} e^{+i\boldsymbol{z}\cdot(\boldsymbol{p}'-\boldsymbol{p})} \right\rangle . \tag{2.11}$$

The definition of the operator $\mathcal{O}$ in Eq. (2.11) depends on the desired GFF. For the vector, axial and tensor GFFs at leading twist-2 the operators are given in Eq. (2.5). On the lattice we construct our operators as linear combinations of

$$\mathcal{O}^{\mu\nu}_{V,q}(z) = \bar{q}(z)\gamma^\mu \overleftrightarrow{\nabla}^\nu q(z) , \tag{2.12a}$$

$$\mathcal{O}^{\mu\nu}_{A,q}(z) = \bar{q}(z)\gamma^\mu\gamma_5 \overleftrightarrow{\nabla}^\nu q(z) , \tag{2.12b}$$

$$\mathcal{O}^{\mu\nu\rho}_{T,q}(z) = \bar{q}(z) i\sigma^{\mu\nu} \overleftrightarrow{\nabla}^\rho q(z) . \tag{2.12c}$$

To realize different spin projections and positive parity we use the projector

$$\mathcal{P}^{\rho} = \frac{1}{2}\left(1+\gamma_4\right)\left(-i\gamma^{\rho}\gamma_5\right)^{1+\delta_{\rho,4}} \tag{2.13}$$

and contract it with the open spin indices of Eq. (2.11). For $\rho = 1, 2, 3$ we obtain the difference of the spin polarization with respect to the quantization axis ρ, while $\rho = 4$ corresponds to the unpolarized case. The positive parity projection is only correct for zero momentum; however, excited state contributions (including states of different parity for nonvanishing momentum) are exponentially suppressed at large Euclidean times τ. In this work, we consider isovector currents $\mathcal{O}$; therefore, all quark lines in the corresponding Wick contractions of the three-point function are connected. Three-point functions are constructed by the sequential method [56] which involves the calculation of sequential propagators with fixed momentum $\boldsymbol{p}'(= \mathbf{0})$ and fixed sink time t'. To improve the overlap of our interpolators in Eqs. (2.10) with the physical ground state, we employ the combination of APE and Wuppertal (Gauss) smearing techniques as demonstrated in Ref [50]. The number of smearing iterations is tunned such that no significant lattice spacing dependencies are detected in the effective mass curve

$$m_N(t_f + a/2) = a^{-1} \ln \frac{C(t_f, \mathbf{0})}{C(t_f + a, \mathbf{0})} .$$

This is demonstrated in Fig. 2.2 where we plot the effective nucleon mass calculated on ensembles III and X and ensembles I, IV and V. These two groups of ensembles correspond to similar pion masses but differ in terms of the lattice spacing. For a more detailed discussion about smearing, we refer the interested reader to Refs. [50, 57, 58].

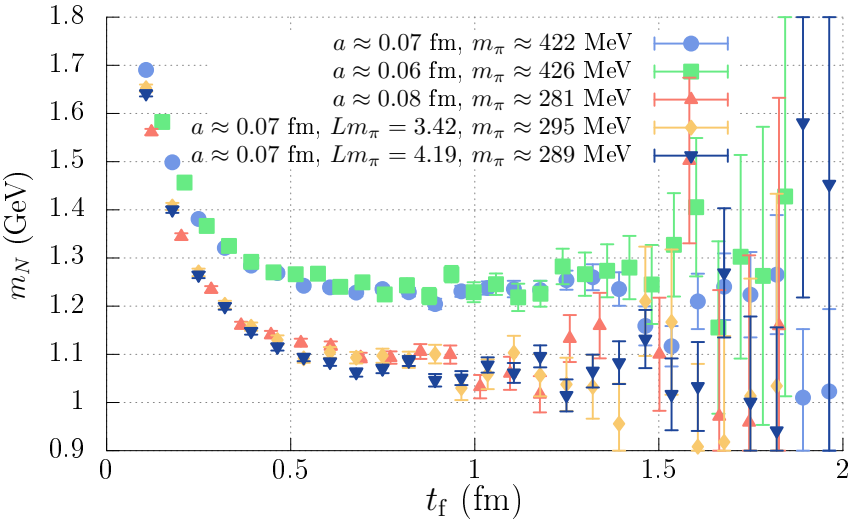

Figure 2.2: Effective nucleon masses for five of our ensembles, computed from smeared-smeared two-point functions. Figure taken from Ref [50].

2.4 Two-point correlation functions

The two-point correlation function, defined in Eq. (2.9), can be written as

$$C(t, \boldsymbol{p}) = \sum_{i=0}^{\infty} A_i(\boldsymbol{p}) \, \mathrm{e}^{-E_i(\boldsymbol{p}) \, t} \, . \tag{2.14}$$

This equation is extremely useful because it allows to determine non-perturbative quantities, like $A_0(\boldsymbol{p})$ and $E_0(\boldsymbol{p})$ from lattice data. In the limit of $t \to \infty$ only the ground state survives because excited states, with larger energies $E_0(\boldsymbol{p}) < E_1(\boldsymbol{p}) < \ldots$, decay more quickly

$$C(t \to \infty, \boldsymbol{p}) \to A_0(\boldsymbol{p}) \, \mathrm{e}^{-E_0(\boldsymbol{p}) \, t} \equiv A(\boldsymbol{p}) \, \mathrm{e}^{-E_N(\boldsymbol{p}) \, t} \, . \tag{2.15}$$

In practice, however, t is finite and excited states contributions are clearly visible in our correlation functions, e.g., compare Fig. 2.2. For the computation of GFFs it is necessary that the lattice data obeys the continuum dispersion relation

$$E_N^c(\boldsymbol{p}) = \sqrt{m_N^2 + \boldsymbol{p}^2} \, , \tag{2.16}$$

because our matrix element decomposition is only valid for the continuum case. To test whether this requirement is fulfilled, we extract the nucleon energy according to a two exponential fit

$$C(t, \boldsymbol{p}) = A(\boldsymbol{p}) \, \mathrm{e}^{-E_N(\boldsymbol{p}) \, t} + X(\boldsymbol{p}) \, \mathrm{e}^{-Y(\boldsymbol{p}) \, t} \tag{2.17}$$

The second term in this ansatz, with the two fit parameters $X(\boldsymbol{p})$ and $Y(\boldsymbol{p})$ is used to parametrize all remaining excited state contributions. We extract the nucleon energy $E_N(\boldsymbol{p})$ from the fit and compare it to the corresponding continuum energy $E_N^c(\boldsymbol{p})$ where we average over all momentum combinations, leading to the same $\boldsymbol{p}^2$. The results are summarized in Fig. 2.3. For the extraction of GFFs we only use momenta whose fitted values for $E_N(\boldsymbol{p})$ are consistent with $E_N^c(\boldsymbol{p})$. In addition, we extract the fit parameter $A(\boldsymbol{p})$ from Eq. (2.17) which is related to the overlap factor $Z(\boldsymbol{p})$ according to

$$A(\boldsymbol{p}) = Z(\boldsymbol{p}) \, \frac{E_N(\boldsymbol{p}) + m_N}{E_N(\boldsymbol{p})} \, . \tag{2.18}$$

These factors are needed for the extraction of GFF matrix elements because they do also appear in the three-point correlation function. Therefore, we compute bootstrap ensembles (bootstrap size is 500) for our fit parameters. The fit-range dependence is studied by varying the start time slices $t_s/a \in \{2, 3\}$ as well as the final time slice t_f/a. We find that the impact of t_s/a on the values for the GFFs is rather mild. Hence, we fix $t_s/a = 2$ in the following. Fig. 2.4 demonstrate our determination of t_f/a.

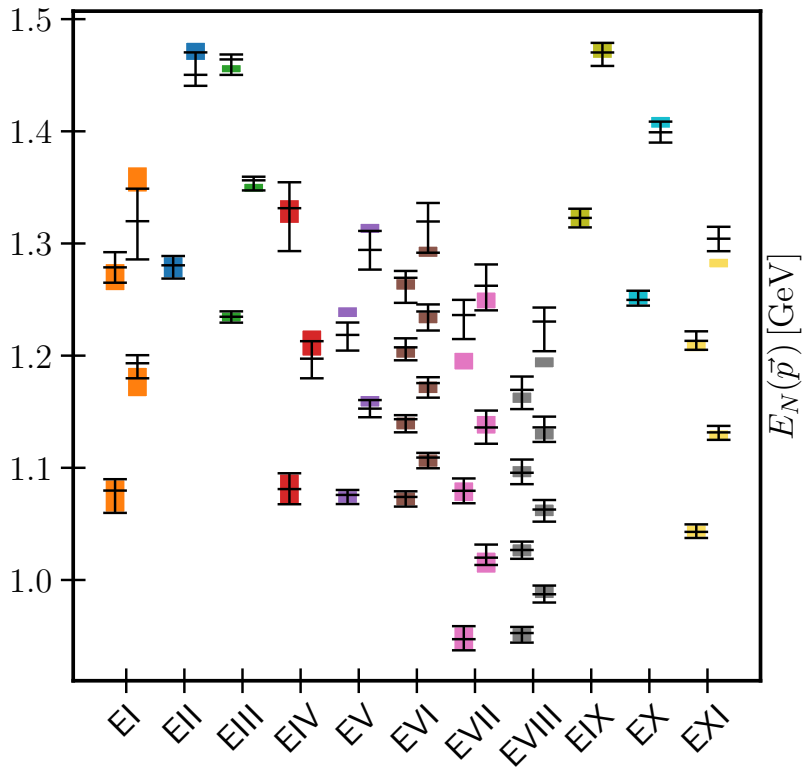

Figure 2.3: Overview of the nucleon energies for our ensembles. We compare the energies $E_N(\boldsymbol{p})$ and the errors extracted from a two-exponential fit shown as black error bars with the energies E_N^c expected from the continuum dispersion relation, which are depicted as colored boxes. Taken from Ref [5].

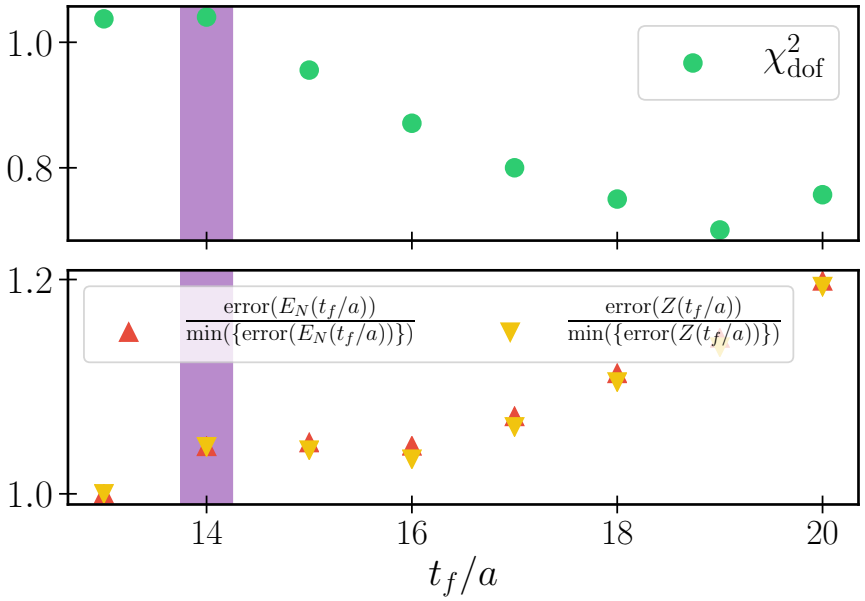

Figure 2.4: The top panel shows the correlated χ^2_{dof} as a function of the final time slice t_f/a for ensemble IV with $E_N(\boldsymbol{p}) = 1.33\,\mathrm{GeV}$; the bottom panel shows the uncorrelated normalized statistical error of the fit parameters E_N and Z. For the case shown we select the $t_f/a = 14$ result. Taken from Ref [5].

We also try single exponential fits and find that they give similar results if one adjusts the fit ranges appropriately. However, the resulting errors on $A(\boldsymbol{p})$ are larger. Hence, we use the two-exponential fit ansatz for our final analysis.

2.5 Renormalization

The computation of GFFs on the lattice involves the renormalization of operators

$$\mathcal{O}_{\overline{\text{MS}}}(\mu) = Z(\beta, \mu)_{\overline{\text{MS}}}\, \mathcal{O}(\beta)$$

where the renormalization factor $Z(\beta, \mu)_{\overline{\text{MS}}}$ depends on the β value, used in the gauge action and the renormalization scale μ. The used renormalization factors are products of perturbative and nonperturbative parts

$$Z_{\mathcal{O}}^{\overline{\text{MS}}} = Z_{\mathcal{O},\text{RI}'}^{\overline{\text{MS}}}\; Z_{\mathcal{O},\text{bare}}^{\text{RI}'} \,.$$

The nonperturbative factor $Z_{\mathcal{O},\text{bare}}^{\text{RI}'}$ translates the bare lattice data to the regularization scheme independent momentum subtraction (RI′-MOM) scheme [59, 60], while the perturbative factor $Z_{\mathcal{O},\text{RI}'}^{\overline{\text{MS}}}$ matches from the RI′-MOM to the $\overline{\text{MS}}$ scheme in the continuum. This is calculated in continuum perturbation theory and is known for our operators to three-loop accuracy [61]. The nonperturbative renormalization factors $Z_{\mathcal{O},\text{bare}}^{\text{RI}'}$ are extracted from the quark propagator in momentum space (color indices are suppressed)

$$S_{\alpha\beta}(a, p) = \frac{a^8}{V} \sum_{xy} e^{-ip\cdot(x-y)} \left\langle q_\alpha(x) \bar{q}_\beta(y) \right\rangle$$

and the three-point functions

$$G_{\alpha\beta}^{j,\mu}(a, p) = \frac{a^{12}}{V} \sum_{xyz} e^{-ip\cdot(x-y)} \left\langle q_\alpha(x)\, \mathcal{J}_\mu^j(z)\, \bar{q}_\beta(y) \right\rangle \,,$$

with the current

$$\mathcal{J}_\mu^j(z) = \bar{q}(z)\, \Gamma^j \overleftrightarrow{\nabla}_\mu q(z) = \bar{q}(z) \mathcal{O}_\mu^j(z) q(z) \,,$$

which are calculated on a subset of gauge configurations in Landau gauge. Γ^j denotes one of the sixteen possible products of Euclidean gamma matrices, $\gamma_1^{n_1} \cdots \gamma_4^{n_4}$ ($n_\mu \in \{0, 1\}$). The covariant lattice derivative acts on the respective left or right quark propagators resulting from the integration over the quark fields. The vertex function $\Gamma_{\mathcal{O}}$ is constructed for each operator $\mathcal{O}(0)$ by combining the appropriate $G^{j,\mu}$s and

amputating the fermion legs,

$$\Gamma_{\mathcal{O}}(a,p) \equiv S^{-1}(a,p) G_{\mathcal{O}}(a,p) S^{-1}(a,p)\,.$$

The renormalized vertex reads

$$\Gamma^{R}_{\mathcal{O}}(p,\mu^2) = \frac{Z^{\mathrm{RI}'}_{\mathcal{O},\mathrm{bare}}(a,\mu^2)}{Z_q(a,\mu^2)} \Gamma_{\mathcal{O}}(a,p)\,,$$

where the RI′-MOM renormalization condition

$$\frac{1}{12}\,\mathrm{Tr}\left(\Gamma^{R}_{\mathcal{O}}\left[\Gamma^{(0)}_{\mathcal{O}}\right]^{-1}\right) \overset{!}{=} 1 \quad \Big|_{p^2=\mu^2}$$

is imposed in the chiral limit. The quark wave function renormalization factor is given by

$$Z_q(a,\mu^2) = \left.\frac{-i\,\mathrm{Tr}\left(\gamma_\lambda \bar{p}_\lambda\, S^{-1}(a,p)\right)}{12\bar{p}^2}\right|_{p^2=\mu^2} \tag{2.19}$$

after extrapolation to the massless limit. In Eq. (2.19) we employ the lattice tree-level expression for the massless quark propagator; i.e., we set $a\bar{p}_\lambda \equiv \sin(ap_\lambda)$. Similarly, we use the lattice tree-level expression for the Born term $\Gamma^{(0)}_{\mathcal{O}}$ to reduce lattice discretization effects. For the example of the operator $\mathcal{O}^{\mu\nu}_{V,q}$ this reads

$$\Gamma^{(0)}_{\mathcal{O}}(p) = i\left(\gamma_\mu \bar{p}_\nu + \gamma_\nu \bar{p}_\mu\right)\,.$$

2.6 Operator multiplets

The calculation of GFFs on the lattice is based on hypercubic space-time implying that the used operators shall be classified according to the symmetries of the lattice rather than the full rotational symmetries of continuous Euclidean spacetime $O(4)$. To that end, operators are classified by irreducible representations of the hypercubic group $H(4) \subset O(4)$. In the case of the vector operator we work with multiplets that transform according to two distinct irreducible representations of the hypercubic group H(4) labeled as $v_{2,a}$ and $v_{2,b}$. These are combinations of the operators in Eq. (2.12a) given by

$$\begin{aligned}
\mathcal{O}^{v_{2,a}}_{\mu\nu} &= \mathrm{S}_{\mu\nu}\mathcal{O}^{V}_{\mu\nu} \quad \text{with} \quad 1 \le \mu < \nu \le 4 \\
\mathcal{O}^{v_{2,b}}_{1} &= \frac{1}{2}(\mathcal{O}^{V}_{11} + \mathcal{O}^{V}_{22} - \mathcal{O}^{V}_{33} - \mathcal{O}^{V}_{44})\,, \\
\mathcal{O}^{v_{2,b}}_{2} &= \frac{1}{\sqrt{2}}(\mathcal{O}^{V}_{33} - \mathcal{O}^{V}_{44})\,, \\
\mathcal{O}^{v_{2,b}}_{3} &= \frac{1}{\sqrt{2}}(\mathcal{O}^{V}_{11} - \mathcal{O}^{V}_{22})\,,
\end{aligned}$$

For the axial operator we use the multiplets $r_{2,a}$ and $r_{2,b}$ constructed from combinations of operators in Eq. (2.12b)

$$\begin{aligned}
\mathcal{O}^{r_{2,a}}_{\mu\nu} &= S_{\mu\nu}\mathcal{O}^{A}_{\mu\nu} \quad \text{with} \quad 1 \leq \mu < \nu \leq 4 \\
\mathcal{O}^{r_{2,b}}_{1} &= \frac{1}{2}(\mathcal{O}^{A}_{11} + \mathcal{O}^{A}_{22} - \mathcal{O}^{A}_{33} - \mathcal{O}^{A}_{44})\,, \\
\mathcal{O}^{r_{2,b}}_{2} &= \frac{1}{\sqrt{2}}(\mathcal{O}^{A}_{33} - \mathcal{O}^{A}_{44})\,, \\
\mathcal{O}^{r_{2,b}}_{3} &= \frac{1}{\sqrt{2}}(\mathcal{O}^{A}_{11} - \mathcal{O}^{A}_{22})\,,
\end{aligned}$$

In case of the tensor operator we use 16 linear combinations of operators defined in Eq. (2.12c) classified by two multiplet $h_{1,a}$ and $h_{1,b}$. The first eight from the $h_{1,a}$ multiplet

$$\begin{aligned}
\mathcal{O}^{h_{1,a}}_{1} &= \sqrt{\frac{2}{3}}(\mathcal{O}^{T}_{132} + \frac{1}{2}\mathcal{O}^{T}_{123} + \frac{1}{2}\mathcal{O}^{T}_{231}), \quad \mathcal{O}^{h_{1,a}}_{2} = \sqrt{\frac{2}{3}}(\mathcal{O}^{T}_{142} + \frac{1}{2}\mathcal{O}^{T}_{124} + \frac{1}{2}\mathcal{O}^{T}_{241}), \\
\mathcal{O}^{h_{1,a}}_{3} &= \sqrt{\frac{2}{3}}(\mathcal{O}^{T}_{143} + \frac{1}{2}\mathcal{O}^{T}_{134} + \frac{1}{2}\mathcal{O}^{T}_{341}), \quad \mathcal{O}^{h_{1,a}}_{4} = \sqrt{\frac{2}{3}}(\mathcal{O}^{T}_{243} + \frac{1}{2}\mathcal{O}^{T}_{234} + \frac{1}{2}\mathcal{O}^{T}_{342}), \\
\mathcal{O}^{h_{1,a}}_{5} &= \sqrt{2}\mathcal{O}^{T}_{2\{13\}}, \quad \mathcal{O}^{h_{1,a}}_{6} = \sqrt{2}\mathcal{O}^{T}_{2\{14\}}, \\
\mathcal{O}^{h_{1,a}}_{7} &= \sqrt{2}\mathcal{O}^{T}_{3\{14\}}, \quad \mathcal{O}^{h_{1,a}}_{8} = \sqrt{2}\mathcal{O}^{T}_{3\{24\}}\,.
\end{aligned}$$

and the remaining eight make up the $h_{1,b}$ multiplet.

$$\begin{aligned}
\mathcal{O}^{h_{1,b}}_{9} &= \sqrt{\frac{1}{2}}(\mathcal{O}^{T}_{122} - \mathcal{O}^{T}_{133}), \quad \mathcal{O}^{h_{1,b}}_{10} = \sqrt{\frac{1}{2}}(\mathcal{O}^{T}_{211} - \mathcal{O}^{T}_{233}), \\
\mathcal{O}^{h_{1,b}}_{11} &= \sqrt{\frac{1}{2}}(\mathcal{O}^{T}_{311} - \mathcal{O}^{T}_{322}), \quad \mathcal{O}^{h_{1,b}}_{12} = \sqrt{\frac{1}{2}}(\mathcal{O}^{T}_{411} - \mathcal{O}^{T}_{422}), \\
\mathcal{O}^{h_{1,b}}_{13} &= \sqrt{\frac{1}{6}}(\mathcal{O}^{T}_{122} + \mathcal{O}^{T}_{133} - 2\mathcal{O}^{T}_{144}), \quad \mathcal{O}^{h_{1,b}}_{14} = \sqrt{\frac{1}{6}}(\mathcal{O}^{T}_{211} + \mathcal{O}^{T}_{233} - 2\mathcal{O}^{T}_{244}), \\
\mathcal{O}^{h_{1,b}}_{15} &= \sqrt{\frac{1}{6}}(\mathcal{O}^{T}_{311} + \mathcal{O}^{T}_{322} - 2\mathcal{O}^{T}_{344}), \quad \mathcal{O}^{h_{1,b}}_{16} = \sqrt{\frac{1}{6}}(\mathcal{O}^{T}_{411} + \mathcal{O}^{T}_{422} - 2\mathcal{O}^{T}_{433}).
\end{aligned}$$

The renormalized operator multiplets for the vector, axial and tensor case are

$$\begin{aligned}
\mathcal{O}^{v_{2,a|b}}_{\overline{\text{MS}}}(\mu) &= Z(\beta,\mu)^{v_{2,a|b}}_{\overline{\text{MS}}}\,\mathcal{O}^{v_{2,a|b}}(\beta)\,, \\
\mathcal{O}^{r_{2,a|b}}_{\overline{\text{MS}}}(\mu) &= Z(\beta,\mu)^{r_{2,a|b}}_{\overline{\text{MS}}}\,\mathcal{O}^{r_{2,a|b}}(\beta)\,, \\
\mathcal{O}^{h_{2,a|b}}_{\overline{\text{MS}}}(\mu) &= Z(\beta,\mu)^{h_{2,a|b}}_{\overline{\text{MS}}}\,\mathcal{O}^{h_{2,a|b}}(\beta)\,,
\end{aligned}$$

where we use $\mu = 2\,\text{GeV}$ as the renormalization scale. The used renormalization factors a summarized in Table 2.1. Note that the renormalization factors depend on the multiplet, i.e., they slightly differ for $v_{2,a}$ and $v_{2,b}$. A detailed description of the renormalization procedure, that consists of first nonperturbatively matching from the

lattice to the RI′-MOM scheme [59, 60] and then translating perturbatively to the $\overline{\text{MS}}$ scheme, may be found in Ref. [62].

	$\beta = 5.20$	$\beta = 5.29$	$\beta = 5.40$
$Z^{v_{2,a}}_{\overline{\text{MS}}}$	1.090 (19)	1.113 (15)	1.140 (16)
$Z^{v_{2,b}}_{\overline{\text{MS}}}$	1.096 (17)	1.117 (21)	1.143 (13)
$Z^{r_{2,a}}_{\overline{\text{MS}}}$	1.083 (16)	1.106 (13)	1.134 (14)
$Z^{r_{2,b}}_{\overline{\text{MS}}}$	1.118 (16)	1.138 (22)	1.163 (13)
$Z^{h_{1,a}}_{\overline{\text{MS}}}$	1.115 (19)	1.141 (19)	1.171 (16)
$Z^{h_{1,b}}_{\overline{\text{MS}}}$	1.129 (20)	1.154 (20)	1.184 (16)

Table 2.1: The renormalization factors used to translate our bare lattice data to the continuum $\overline{\text{MS}}$ scheme at $\mu = 2\,\text{GeV}$, obtained by reanalyzing the data of Ref. [62]

2.7 Extracting GFFs from lattice data

In the following, we demonstrate the extraction procedure for the vector GFFs. The axial and tensor GFFs are treated analogously. We start by expanding the three-point function Eq. (2.11) in terms of energy eigenstates

$$C^{\tau'\tau}(\tau, t', \boldsymbol{p}', \boldsymbol{p}) = \mathcal{A}^{\tau'\tau} \cdot \mathrm{e}^{-E_N(\boldsymbol{p}')(t'-\tau)}\, \mathrm{e}^{-E_N(\boldsymbol{p})\,\tau} + \text{excited states}\,, \tag{2.20}$$

where the ground state amplitude reads

$$\mathcal{A}^{\tau'\tau} = \sum_{\sigma'\sigma} \frac{\left\langle 0|\mathcal{N}^{\tau'}|N(p',\sigma')\right\rangle \left\langle N(p',\sigma')|\mathcal{O}^{v_{2,a|b}}_{\overline{\text{MS}}}|N(p,\sigma)\right\rangle \left\langle N(p,\sigma)|\overline{\mathcal{N}}^{\tau}|0\right\rangle}{4\,E_N(\boldsymbol{p}')E_N(\boldsymbol{p})}\,. \tag{2.21}$$

The exponentials contain the energy of the nucleon as a function of the considered spatial momentum, the Euclidean operator insertion time τ, and the sink time t'. Up to lattice artifacts, the matrix elements of an operator $\mathcal{O}^{\mu\nu}_{V,q}(z)$ can be decomposed according to the Euclidean versions of Eqs. (2.7a) and (2.8a). In doing so, it is necessary to distinguish between the two multiplets $v_{2,a}$ and $v_{2,b}$ (cf. section 2.6). The decomposition of the matrix element defined in Eq. (2.21) can be written as

$$\left\langle N(p',\sigma')|\mathcal{O}^{v_{2,a|b}}_{\overline{\text{MS}}}|N(p,\sigma)\right\rangle = \overline{U}(p',\sigma')\,\mathbb{D}^{v_{2,a|b}}_{\overline{\text{MS}}}\,U(p,\sigma)\,. \tag{2.22}$$

Our final expression for the parametrization of the lattice three-point function is

$$\begin{aligned} c^{\rho}_{V}(\tau, t', \boldsymbol{p}', \boldsymbol{p}) &\equiv \sum_{\alpha,\beta} \mathcal{P}^{\rho}_{\beta\alpha} C_{\alpha\beta}(\tau, t', \boldsymbol{p}', \boldsymbol{p}) = \\ &= \sqrt{Z(\boldsymbol{p}')\,Z(\boldsymbol{p})}\,\mathcal{F}_V\,\mathrm{e}^{-E_N(\boldsymbol{p}')(t'-\tau)}\,\mathrm{e}^{-E_N(\boldsymbol{p})\,\tau} + \text{excited states}\,, \end{aligned} \tag{2.23}$$

where we included the projection operator $\mathcal{P}^\rho$ (cf. Eq. (2.13)). The Z factors in Eq. (2.23) depend on the overlap of our nucleon interpolation operators with the nucleon ground state. They vary with momentum and smearing and are extracted from the two-point correlation function as previously discussed in section 2.4. In Eq. (2.23) we use

$$\mathcal{F}_V = \frac{\mathrm{tr}\left\{\mathcal{P}^\rho\left[-i\not{p}' + m_N\right]\mathbb{D}^{V_2,a|b}_{\overline{\mathrm{MS}}}\left[-i\not{p} + m_N\right]\right\}}{4\,E_N(\boldsymbol{p}\,')E_N(\boldsymbol{p}\,)} \quad \text{with} \quad \not{p} \equiv iE_N(\boldsymbol{p}\,)\gamma_4 + \boldsymbol{p}\cdot\boldsymbol{\gamma}\,. \tag{2.24}$$

The desired GFFs are contained in $\mathcal{F}_V$ and the prefactors can be computed by inserting the respective Euclidean γ-matrices. Here, we restrict ourselves to the final momentum $\boldsymbol{p}\,' = \boldsymbol{0}$. Taking all available combinations of operator multiplets, projections $\mathcal{P}^\rho$ and momenta $\boldsymbol{p}$ for a fixed virtuality

$$Q^2 = -\mathrm{t} = \left(\boldsymbol{p}\,' - \boldsymbol{p}\,\right)^2 - \left(\sqrt{m_N^2 + \boldsymbol{p}\,'^2} - \sqrt{m_N^2 + \boldsymbol{p}^2}\right)^2\,, \tag{2.25}$$

we obtain a linear system of equations

$$\mathcal{F}_V = M_V \cdot \boldsymbol{g}_V\,. \tag{2.26}$$

The coefficient matrix M_V consists of the prefactors calculated from Eq. (2.24) and $\mathcal{F}_V$ is extracted from a fit of Eqs. (2.20) and (2.23) to two and three-point functions. The desired unknown GFFs are contained in the vector

$$\boldsymbol{g}_V = (A_{20}(\mathrm{t}), B_{20}(\mathrm{t}), C_{20}(\mathrm{t}))^\mathsf{T}\,. \tag{2.27}$$

The number of columns of M_V is equal to the number of unknown GFFs (in this case 3), but the number of rows depends on the available combinations. In almost all the cases this yields an overdetermined system of equations, meaning that the number of elements in $\mathcal{F}_V$, denoted with $\dim\mathcal{F}_V$, is larger than the number of GFFs. Note that the individual rows of M_V are either real or imaginary.[1] For a given ensemble this system of equations has to be solved separately for each virtuality to yield the GFFs as functions of t. In general, we write Eq. (2.26) as

$$\mathcal{F}^q_\Gamma = M_\Gamma \cdot \boldsymbol{g}^q_\Gamma\,, \tag{2.28}$$

where Γ can take the values V, A, T and $\boldsymbol{g}^q_\Gamma$ is the vector of the respective GFFs (cf. Eqs. 2.8). Due to equivalent combinations of momenta and polarizations most rows in the matrix M_Γ are equal or differ by a sign only. We average the corresponding three-point correlation functions, which improves the signal-to-noise ratio

[1] If a row vanishes, then it does not restrict the GFF and we remove it from the system of equations.

considerably and reduces the number of equations.

Let us now discuss the fitting procedure of lattice three-point functions, the parametrization of which is given in (2.23). As previously discussed we use the sequential source method where we set the outgoing nucleon momentum $\boldsymbol{p}' = \mathbf{0}$ for all our ensembles. This implies that $E_N(\boldsymbol{p}') = m_N$ in Eq. (2.23). The initial energy $E_N(\boldsymbol{p})$ in Eq. (2.23) is determined from the continuum dispersion relation (2.16). The momentum restriction, discussed in section 2.4 translates to a range $0 \leq Q^2 < 0.6\,\mathrm{GeV}^2$ for the three-point functions. With $Z(\boldsymbol{p}')$ and $Z(\boldsymbol{p})$ having been determined from the two-point correlation functions, the only free parameter left is $\mathcal{F}_\Gamma^q$. To achieve ground state dominance, one has to make sure that $aN_T \gg t' \gg \tau \gg 0$ (cf. Eq. (2.20)). We consider $\tau \in [\tau_s, \tau_e]$ where τ_s is substantially larger than zero and τ_e substantially smaller than t'. The sink times vary with the ensemble (see the last column of Table A.1). In section 2.9, we examine excited state contaminations.

2.8 Solving the overdetermined system of equations

As explained above, for every current $\Gamma = V$, A or T, quark flavor q and virtuality $-\mathrm{t}$, we need to solve the linear system Eq. (2.28), i.e., $\mathcal{F} = M \cdot \boldsymbol{g}$, to extract the relevant form factors $\boldsymbol{g}$ from the vector of inequivalent matrix elements $\mathcal{F}$ that correspond to nonvanishing rows of M. Here we drop all indices like the quark flavor q and Γ for convenience. In what follows m denotes the number of independent form factors while $n \geq m$ is the length of $\mathcal{F}$. Consequently, M is a $n \times m$ matrix of maximal rank, i.e., $\mathrm{Rank}(M) = m$. The determination of the form factors is carried out in two ways. The first method consists of two steps: First, we extract the ground state nucleon matrix elements $\mathcal{F}_j$ from the lattice three-point function data c_j^τ, restricted to the range of insertion times $\tau \in [\tau_s, \tau_e]$, through the numerical minimization of the χ^2-function

$$\chi^2\big(\mathcal{F}\big) = \sum_{j=1}^{n} \sum_{\tau,\tau'=\tau_s}^{\tau_e} \delta c_j^\tau \left[\mathrm{cov}_j^{-1}\right]_{\tau\tau'} \delta c_j^{\tau'}\,, \tag{2.29}$$

where δc_j^τ is the difference

$$\delta c_j^\tau = c_j^\tau - \mathcal{F}_j \sqrt{Z(\boldsymbol{p}')Z(\boldsymbol{p})}\, \mathrm{e}^{-m_N(t'-\tau)}\, \mathrm{e}^{-E_N(\boldsymbol{p})\tau} \tag{2.30}$$

between the lattice data and the three-point function parametrization Eq. (2.23). The inverse covariance matrix cov_j^{-1} depends on the insertion times τ and τ'. One can easily generalize the fit to the situation of multiple source-sink distances t' if this is required or include excited state contributions. The index $j \in \{1, \ldots, n\}$ runs over all possible polarizations ρ and initial momenta $\boldsymbol{p}$ (keeping the virtuality Q^2 fixed), which give nonvanishing contributions. Once the fit parameters $\mathcal{F}_j$ are determined,

one can minimize

$$\epsilon^2 = (M\boldsymbol{g} - \mathcal{F})^2 \tag{2.31}$$

to determine the form factors $\boldsymbol{g}$. The total number of parameters for this method is $m+n$ and, in particular for large virtualities, this number can be quite large (up to 50). This is not the only problem but it can happen that the resulting ϵ value is quite large and it is not clear how one should deal with such a situation. Ideally, ϵ should be zero but this is only possible if $\mathcal{F}$ is in the image of M (cf. Eq. (2.31)). Motivated by this observation, we carry out our fits employing a single step method, which combines the two subsequent steps into a single minimization problem, restricting the number of fit parameters to the relevant degrees of freedom. We start from the singular value decomposition,

$$M = U \cdot \Sigma \cdot V^\intercal \tag{2.32}$$

with orthogonal matrices $U \in \mathbb{R}^{n\times n}$, $V \in \mathbb{R}^{m\times m}$ and the matrix $\Sigma \in \mathbb{R}^{n\times m}$, which has nonvanishing entries only on the diagonal. The pseudoinverse Σ^+ is a $m \times n$ matrix that can easily be obtained, computing the inverses of the diagonal elements of Σ. Each vector $\mathcal{F}$ within the image of M can be uniquely expressed as a linear combination

$$\mathcal{F}(\boldsymbol{\alpha}) = \sum_{i=1}^{m} \alpha_i \, \boldsymbol{u}^i \tag{2.33}$$

of the first m column vectors of U. Note that $m = \mathrm{Rank}(M)$. Substituting $\mathcal{F} \mapsto \mathcal{F}(\boldsymbol{\alpha})$ in Eq. (2.30) [and thereby Eq. (2.29)], we obtain a modified χ^2-function that depends on the parameters α_i, where $i \in \{1, \ldots, m\}$. Finally, we convert the extracted vector $\boldsymbol{\alpha}$ to the desired GFF vector,

$$\boldsymbol{g} = [V\Sigma^+ U^\intercal] \sum_{i=1}^{m} \alpha_i \, \boldsymbol{u}^i = [V\Sigma^+] \, \boldsymbol{\alpha} \,, \tag{2.34}$$

where in the last step Σ^+ is truncated to a $m \times m$ square matrix. In Fig. 2.5 we show as example for the nearly physical quark mass ensemble VIII that this method works very well. In this case, eight different lattice channels, listed in Table 2.2, are well described in terms of three fit parameters. A comparison of the two fit methods shows that the results are consistent within errors for all GFFs and for all ensembles. The single step method, however, results in somewhat smaller statistical errors and a smoother Q^2 dependence, especially for the induced GFFs. In Fig. 2.6, we directly compare the two methods. For the final results, we only use the correlated single step method because the resulting fits provide a very satisfactory description of the data.

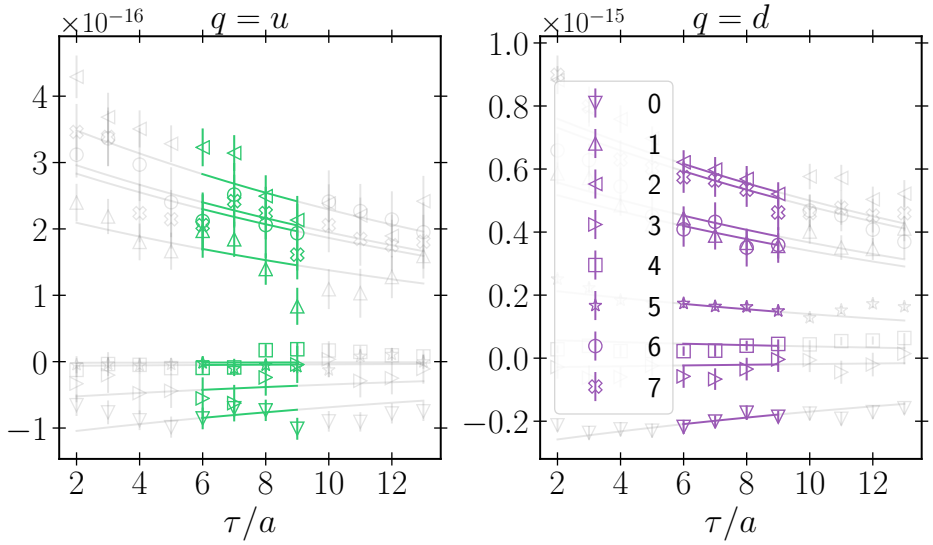

Figure 2.5: Fit results using the single step minimization method. We show ensemble VIII at the virtuality $Q^2 = 0.277\,\mathrm{GeV}^2$ in the vector channel. This corresponds to a spatial momentum transfer of $2 \cdot 2\pi/L$, where we have averaged over all equivalent lattice directions. Three fit parameters $\boldsymbol{\alpha} = (\alpha_1, \alpha_2, \alpha_3)^\intercal$ fully describe eight three-point functions. Colored points lie in the fit range $[\tau_s, \tau_e]$ [cf. Eq. (2.29)]. On the left we show data for the u quark and on the right for the d quark (omitting disconnected contributions). The numbers in the legend refer to the channels listed in Table 2.2. Taken from Ref [5].

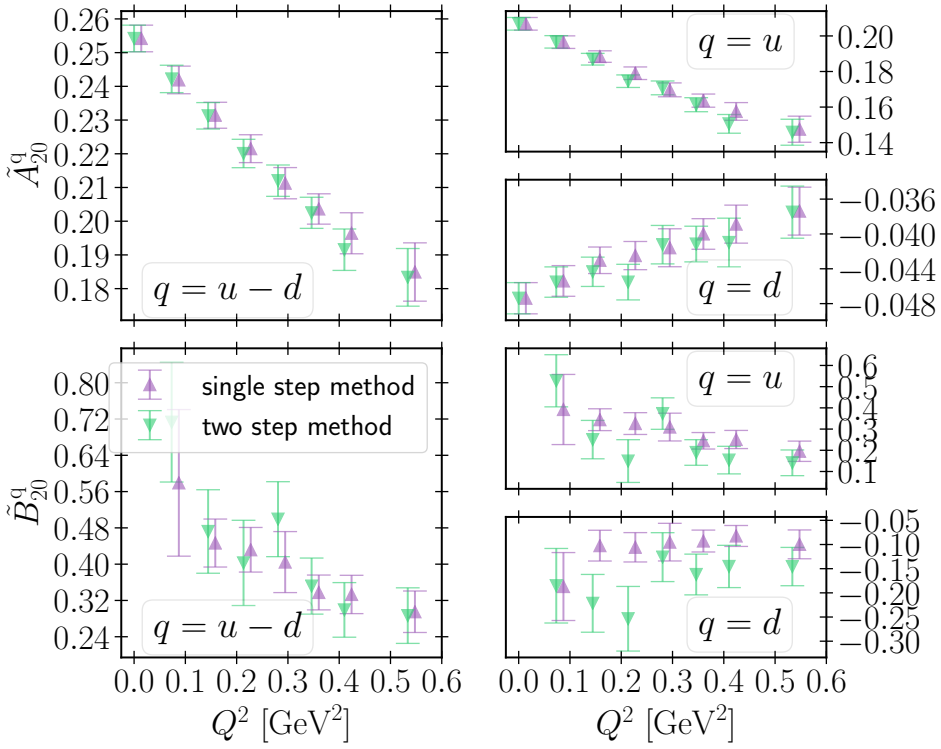

Figure 2.6: Comparison of single step and two step fit methods for the axial GFFs for ensemble VI. The right panels show $\widetilde{A}_{20}$ and $\widetilde{B}_{20}$ separately for the u and d quark (without disconnected contributions), the left panels for the isovector case. Taken from [5].

Channel	$\mathcal{P}^\rho$	$\mathcal{O}$	$\hat{k}$	Channel	#contrib.
0	$\mathcal{P}^4$	$\mathcal{O}_{14}^{\nu_2,a}$	$\pm 2\hat{e}_1$	imaginary	2
		$\mathcal{O}_{24}^{\nu_2,a}$	$\pm 2\hat{e}_2$		2
		$\mathcal{O}_{34}^{\nu_2,a}$	$\pm 2\hat{e}_3$		2
1		$\mathcal{O}_{1}^{\nu_2,b}$	$\pm 2\hat{e}_1$	real	2
			$\pm 2\hat{e}_2$		2
2		$\mathcal{O}_{2}^{\nu_2,b}$	$\pm 2\hat{e}_1$	real	2
			$\pm 2\hat{e}_2$		2
3		$\mathcal{O}_{3}^{\nu_2,b}$	$\pm 2\hat{e}_1$	real	2
			$\pm 2\hat{e}_2$		2
4	$\mathcal{P}^1$	$\mathcal{O}_{23}^{\nu_2,a}$	$\pm 2\hat{e}_2$, $\pm 2\hat{e}_3$	imaginary	4
	$\mathcal{P}^2$	$\mathcal{O}_{13}^{\nu_2,a}$	$\pm 2\hat{e}_1$, $\pm 2\hat{e}_3$		4
	$\mathcal{P}^3$	$\mathcal{O}_{12}^{\nu_2,a}$	$\pm 2\hat{e}_1$, $\pm 2\hat{e}_2$		4
5	$\mathcal{P}^1$	$\mathcal{O}_{34}^{\nu_2,a}$	$\pm 2\hat{e}_2$	real	2
		$\mathcal{O}_{24}^{\nu_2,a}$	$\pm 2\hat{e}_3$		2
	$\mathcal{P}^2$	$\mathcal{O}_{34}^{\nu_2,a}$	$\pm 2\hat{e}_1$		2
		$\mathcal{O}_{14}^{\nu_2,a}$	$\pm 2\hat{e}_3$		2
	$\mathcal{P}^3$	$\mathcal{O}_{24}^{\nu_2,a}$	$\pm 2\hat{e}_1$		2
		$\mathcal{O}_{14}^{\nu_2,a}$	$\pm 2\hat{e}_2$		2
6	$\mathcal{P}^4$	$\mathcal{O}_{1}^{\nu_2,b}$	$\pm 2\hat{e}_3$	real	2
7	$\mathcal{P}^4$	$\mathcal{O}_{2}^{\nu_2,b}$	$\pm 2\hat{e}_3$	real	2

Table 2.2: Individual operator contributions to the fits shown in Fig. 2.5. The numbers in the legend of Fig. 2.5 correspond to the channels below. We parametrize the spatial lattice momentum $\boldsymbol{q} = \hat{k} 2\pi/L$ in terms of $\hat{e}_1$,$\hat{e}_2$, and $\hat{e}_3$ which are unit vectors in the three spatial directions.

2.9 Excited states

For some of our ensembles, we have three-point function data for different source-sink separations. This allows us to analyze the influence of excited states on the GFFs. Our analysis is based on ensemble IV with five source-sink separations in the range $t'/a \in [7, 17]$ and on ensemble VIII with three source-sink separations in the range $t'/a \in [9, 15]$. In physical units $t' = 15a$ corresponds to about 1 fm. Ensemble VIII has data for eight values of Q^2 and this ensemble corresponds to an almost physical pion mass. We show results only for this ensemble, but our findings are consistent for both ensembles. For the tensor GFFs $\widetilde{A}_{T20}^{u-d}$, B_{T20}^{u-d} and $\widetilde{B}_{T21}^{u-d}$ we find that within statistical errors the Q^2 dependence is not affected by a variation of t'. Only for A_{T20}^{u-d} we find a mild dependence for the first virtualities as shown in Fig. 2.7.

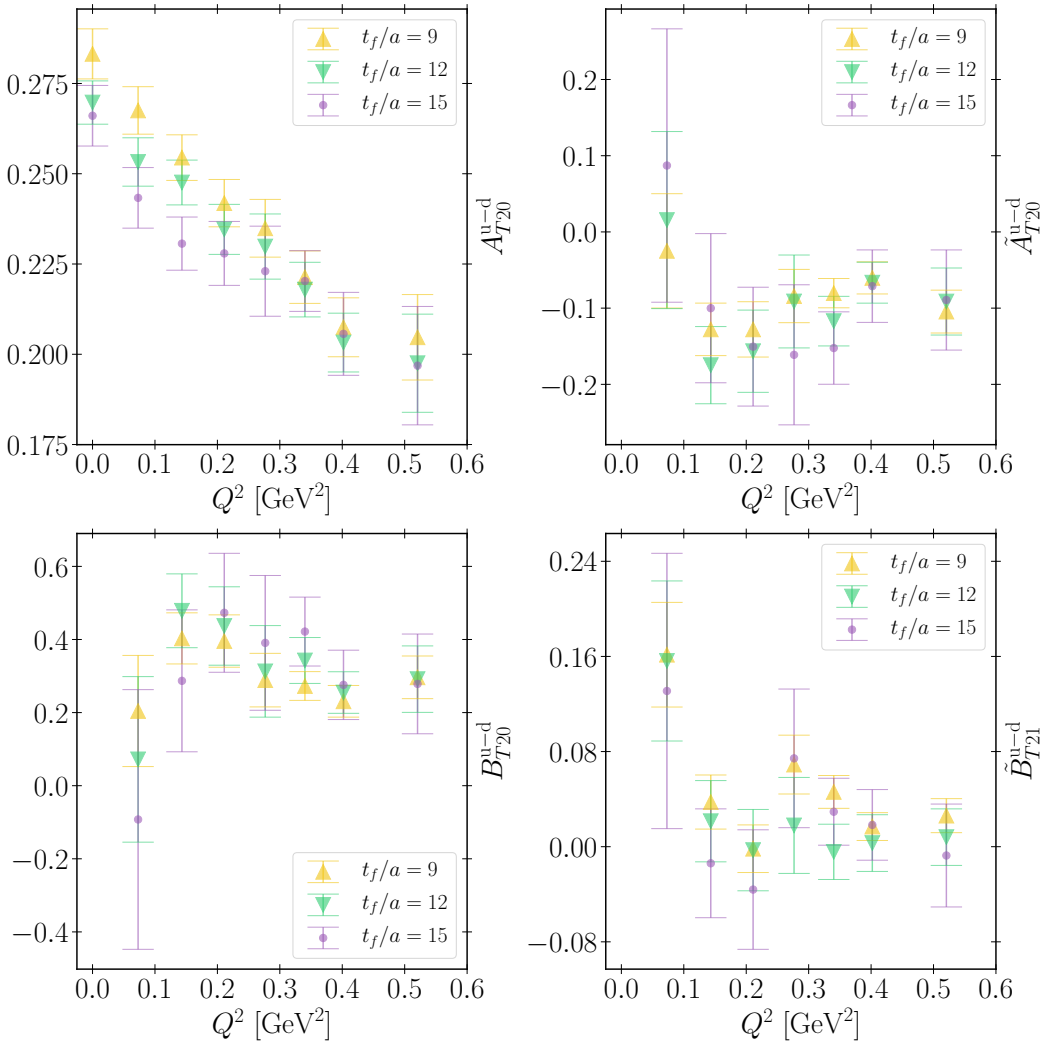

Figure 2.7: The tensor GFFs vs Q^2 for different sink times t' for ensemble VIII.

In Fig. 2.8, we show similar plots for the vector and axial GFFs. For the axial GFFs $\widetilde{A}^{u-d}_{20}$ and $\widetilde{B}^{u-d}_{20}$ we can not detect a significant exited states contamination. Only in the vector case, A^{u-d}_{20} and B^{u-d}_{20}, excited state contaminations are clearly visible. We have tried to parametrize these excited-state contributions to the three-point function with various multiexponential fit ansätze. This, however, introduces additional fit parameters, in particular the mass and the energy of the first excited state. The first excitation in the three-point function can be a multihadron state and hence its energy will in general not be well approximated by the single particle continuum dispersion relation. In order to parametrize excited state contributions, several source-sink separations are required. However, within present statistical errors little dependence is visible for $t' \gtrsim 0.9\,\text{fm}$, even in the A_{20} channel where we achieve the highest accuracy; Hence, we have restricted, our GFF fits to ranges of τ where the data are well described by a single exponential (cf. Fig. 2.5). In all the cases, t' is larger than 1 fm.

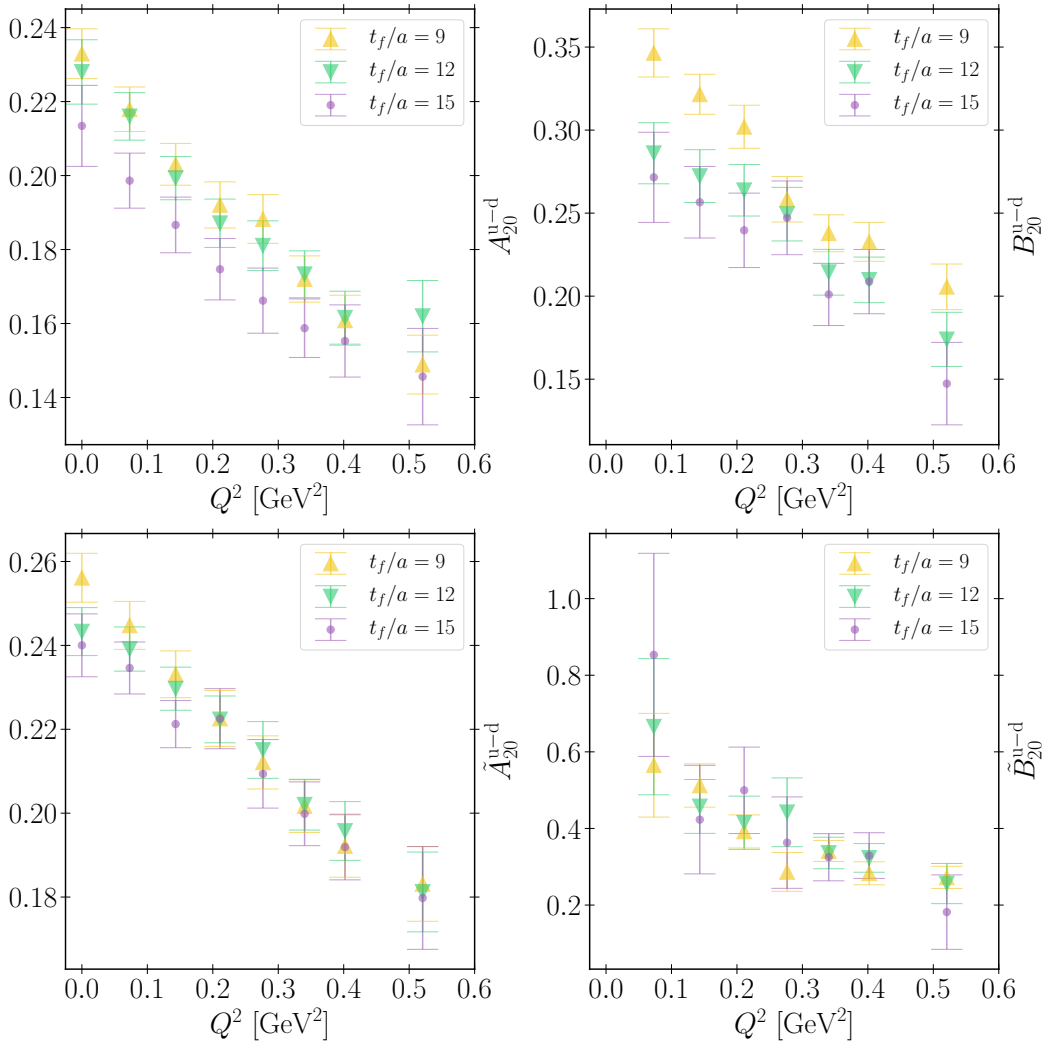

Figure 2.8: Vector and axial GFFs vs Q^2 for different sink times t' for ensemble VIII.

2.10 Results for nucleon GFFs

In this section, we present our results for the nucleon GFFs on a subset of the ensembles listed in Table A.1. We restrict ourselves to ensembles with $m_\pi < 300\,\text{MeV}$ and $m_\pi L > 3.4$ and analyze the quark mass, volume and lattice spacing dependence in the following subsections. In Fig. 2.9, we plot the legend which is common for all plots in this section. All results refer to the $\overline{\text{MS}}$ scheme at $\mu = 2\,\text{GeV}$. We discuss our results in the following subsections.

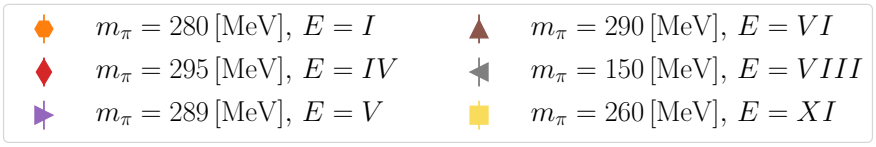

Figure 2.9: Used symbols for the plots shown in this section.

2.10.1 Vector and axial GFFs

Results for vector GFFs, A_{20}^{u-d}, B_{20}^{u-d} and C_{20}^{u-d}, are shown in Figs. (2.10, 2.11, 2.12), respectively, as a function of $Q^2 = -t$. Discretization effects are negligible within errors (comparing ensembles I and XI, which give about the same pion mass and a similar value for Lm_π). Also the volume dependence (cf. V and VI) is small, although there is a slight trend towards larger values for B_{20}^{u-d} if Lm_π increases from about 4.2 to 6.7. For A_{20}^{u-d} and C_{20}^{u-d}, we do not see any volume dependence within present errors.

Similar statements hold for the quark mass dependence: For A_{20}^{u-d} and C_{20}^{u-d}, it is negligible within errors, but for B_{20}^{u-d} we see a trend towards lower values if the pion mass decreases down to 150 MeV (cf. VIII and VI). However, the latter could also be a volume artifact, since there is also a clear correlation between Lm_π and B_{20}^{u-d} (cf. ensembles VIII, V and VI where $Lm_\pi \simeq 3.5$, 4.2 and 6.7, respectively).

A_{20}^{u-d} and B_{20}^{u-d} have a roughly linear Q^2 dependence for small Q^2, and C_{20}^{u-d} is zero within errors. This agrees with the leading t-dependence expected from covariant baryon chiral perturbation theory. We like to point out, that also the individual (quark line connected) u and d quark contributions to C_{20}^{u-d} are zero within error. So the smallness of this generalized form factor is not due to an approximate cancellation. For large Q^2 we expect that A_{20}^{u-d} exhibits a dipole-like Q^2-dependence, which we saw in our former study (cf. Fig. 2 of Ref. [42]). Furthermore, note that in the forward limit ($t = 0$), A_{20}^{u-d} equals the average quark momentum fraction.

Results for the axial GFFs are shown in Figs. (2.13, 2.14). A change of volume, quark mass or lattice spacing has almost no effect on the data. Within errors, these effects cannot be resolved. Both form factors grow approximately linearly for $Q^2 \to 0$. For $\widetilde{B}_{20}^{u-d}$ the statistical errors become larger for $Q^2 \to 0$ whereas the errors for $\widetilde{A}_{20}^{u-d}$ are nearly independent of Q^2.

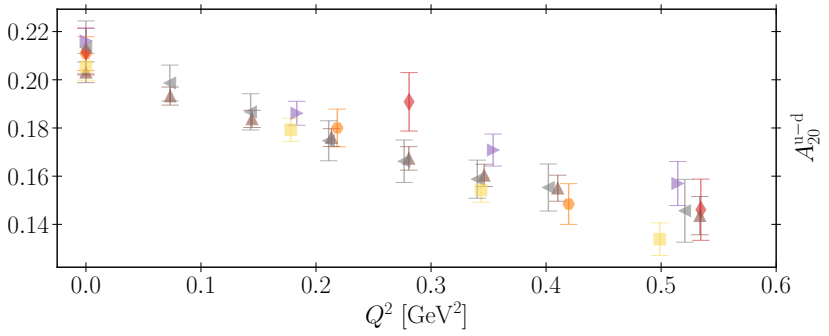

Figure 2.10: Results for A_{20}^{u-d} as a function of Q^2. Legend shown in Fig. 2.9.

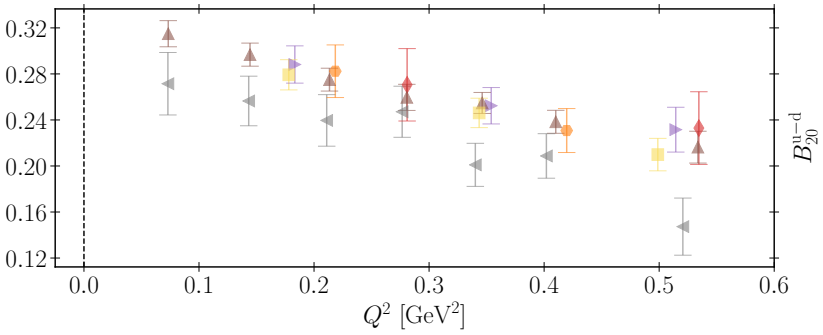

Figure 2.11: Results for B_{20}^{u-d} as a function of Q^2. Legend shown in Fig. 2.9.

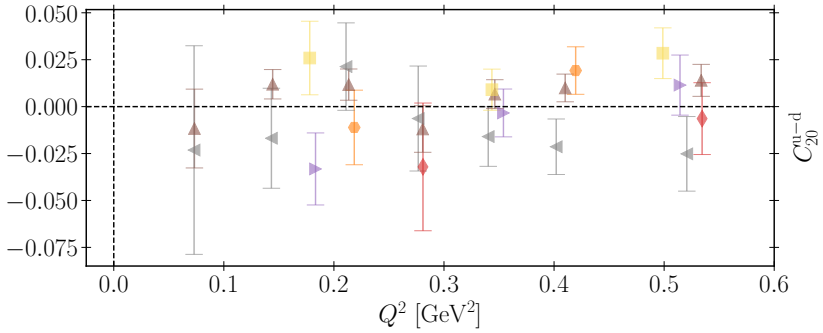

Figure 2.12: Results for C_{20}^{u-d} as a function of Q^2. Legend shown in Fig. 2.9.

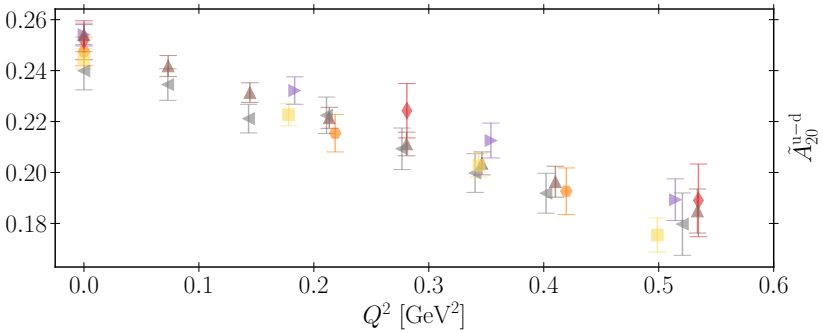

Figure 2.13: Results for $\widetilde{A}_{20}^{u-d}$ as a function of Q^2. Legend shown in Fig. 2.9.

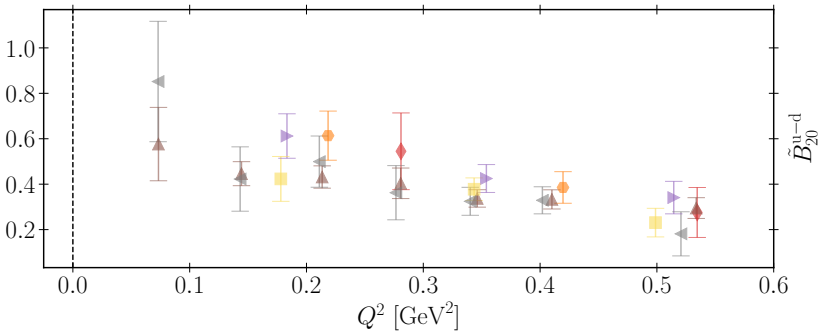

Figure 2.14: Results for $\widetilde{B}_{20}^{u-d}$ as a function of Q^2. Legend shown in Fig. 2.9.

2.10.2 Tensor GFFs

In the following, we show results for the tensor GFFs A_{T20}^{u-d}, B_{T20}^{u-d}, $\widetilde{A}_{T20}^{u-d}$ and $\widetilde{B}_{T21}^{u-d}$ in Figs. (2.15, 2.16, 2.17, 2.18), respectively. The dominant form factors are A_{T20}^{u-d} and B_{T20}^{u-d}. For the available virtualities A_{T20}^{u-d} rises linearly for $Q^2 \to 0$, while B_{T20}^{u-d} remains more or less constant, well above zero. Overall, the statistical errors for A_{T20}^{u-d} are smaller than for B_{T20}^{u-d}. Volume, quark mass or lattice spacing effects cannot be resolved within errors. The other two GFFs, $\widetilde{A}_{T20}^{u-d}$ and $\widetilde{B}_{T21}^{u-d}$, are smaller in comparison and, besides a few outliers, are best described by a constant. However, a final conclusion cannot be drawn as the statistical errors for both GFFs are rather large. Another interesting quantity is the linear combination

$$\overline{B}_{T20}^{q} = B_{T20}^{q} + 2\widetilde{A}_{T20}^{q}\,, \tag{2.35}$$

which corresponds to the combination of GPDs $E_T + 2\tilde{H}_T$ that is related to the Boer-Mulders function $h_1^{\perp}$ [63]. Furthermore, it is important for the transverse spin distribution in the nucleon which will be discussed in Section. 2.14. The results for $\overline{B}_{T20}^{u-d}$ are shown in Fig. 2.19. We find that the statistical error of $\overline{B}_{T20}^{q}$ is significantly smaller compared to the individual errors of B_{T20}^{q} and $\widetilde{A}_{T20}^{q}$.

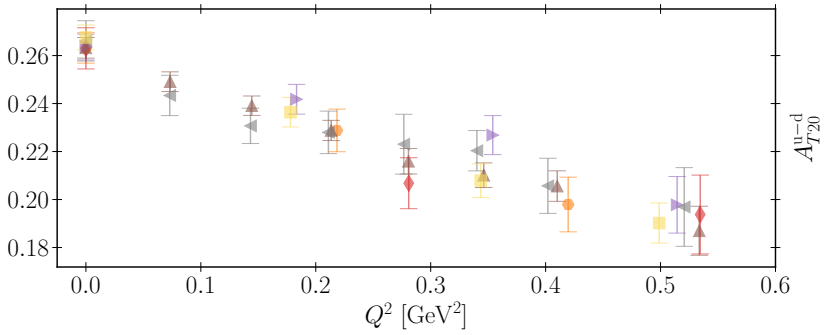

Figure 2.15: Results for $\widetilde{A}_{T20}^{u-d}$ as a function of Q^2. Legend shown in Fig. 2.9.

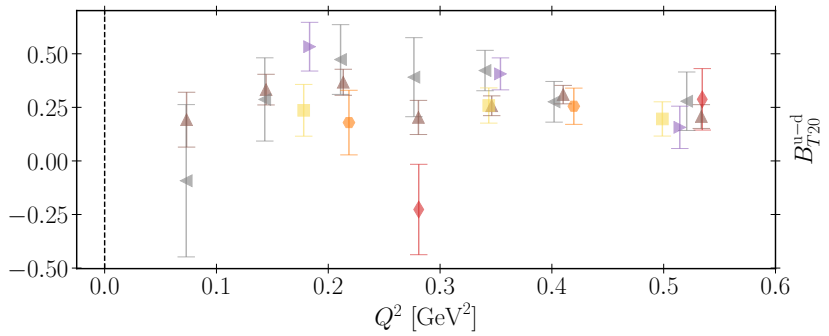

Figure 2.16: Results for $\widetilde{B}_{T20}^{u-d}$ as a function of Q^2. Legend shown in Fig. 2.9.

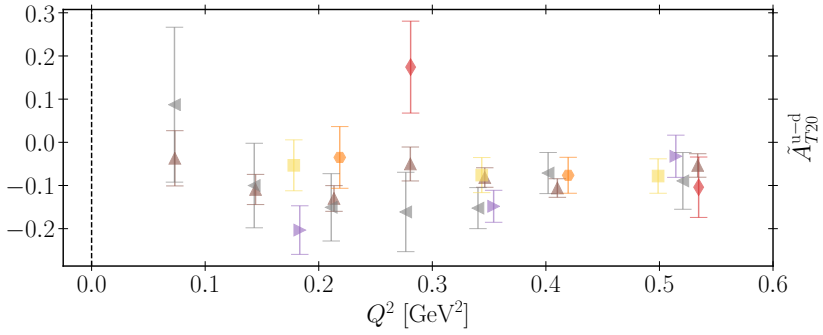

Figure 2.17: Results for $\widetilde{A}_{T20}^{u-d}$ as a function of Q^2. Legend shown in Fig. 2.9.

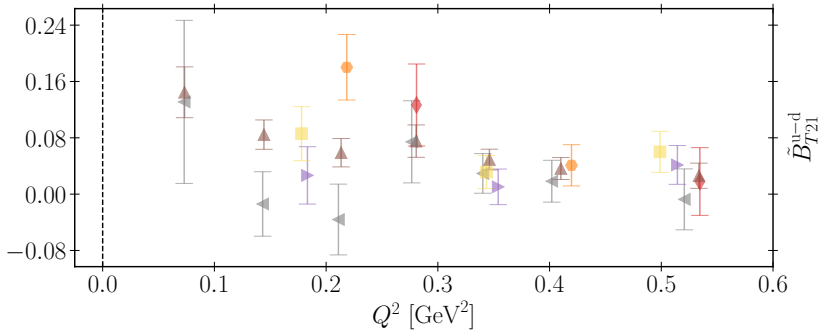

Figure 2.18: Results for $\widetilde{B}_{T21}^{u-d}$ as a function of Q^2. Legend shown in Fig. 2.9.

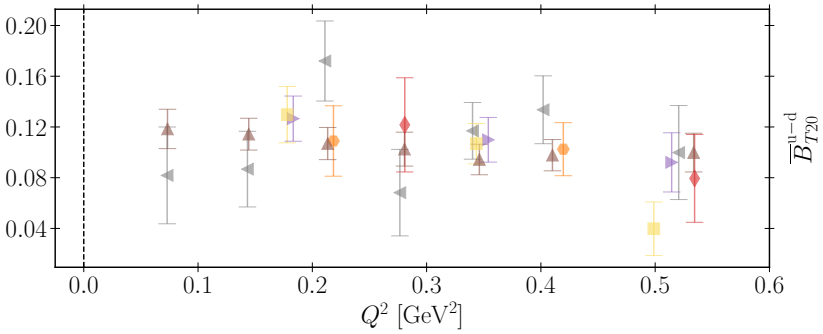

Figure 2.19: Results for $\overline{B}_{T20}^{u-d}$ as a function of Q^2. Legend shown in Fig. 2.9.

2.11 Effects on GFFs caused by renormalization constant errors

Our estimates for the renormalization factors carry an uncertainty which has to be propagated into the GFFs. We do this in a naive but conservative way by carrying out the whole analysis both using the central values of the renormalization factors and adding the error of these factors to their central values. The difference between these two sets of results is then due to the uncertainty of the renormalization. This procedure is applied to all ensembles and to all the available virtualities Q^2. We

find that the relative error is almost independent of Q^2 and the considered ensemble. Hence, for each GFF we decided to take the largest value of this uncertainty as an estimator of the error. These relative uncertainties are shown in Table 2.3.

A_{20}^{u-d}	B_{20}^{u-d}	$\widetilde{A}_{20}^{u-d}$	$\widetilde{B}_{20}^{u-d}$	A_{T20}^{u-d}	B_{T20}^{u-d}	$\widetilde{A}_{T20}^{u-d}$	$\widetilde{B}_{T21}^{u-d}$	$\overline{B}_{T20}^{u-d}$
0.019	0.019	0.015	0.034	0.020	0.020	0.020	0.027	0.020

Table 2.3: Relative error of the GFFs for the flavor combination $u - d$, induced by the uncertainty of the renormalization constants. This error turns out to be almost independent of the virtuality.

2.12 Forward limit results

In this section, we present forward limit results for GFFs which do not require an extrapolation to $Q^2 \to 0$. The presented results are obtained from our nearly physical point ensemble VIII. More specifically, we quote results for

$$A_{20}^{u-d}(0) = \langle x \rangle_{u-d} \,, \quad \widetilde{A}_{20}^{u-d}(0) = \langle x \rangle_{\Delta u - \Delta d} \,, \quad A_{T20}^{u-d}(0) = \langle x \rangle_{\delta u - \delta d} \,. \tag{2.36}$$

$\langle x \rangle_{u-d}$ is the well-known iso-vector quark momentum fraction and the two remaining objects are the helicity and transversity moments restrictively. Our results for the physical point ensemble are summarized in Table 2.4.

Ensemble VIII	Value
$A_{20}^{u-d}(0, m_\pi)$	0.213 (11) (04)
$\widetilde{A}_{20}^{u-d}(0, m_\pi)$	0.240 (07) (03)
$A_{T20}^{u-d}(0, m_\pi)$	0.266 (08) (04)

Table 2.4: Results for A_{20}^{u-d}, $\widetilde{A}_{20}^{u-d}$ and A_{T20}^{u-d} at the nearly physical pion mass $m_\pi = 150\,\text{MeV}$ (ensemble VIII). The first error is statistical, the second error is due to the uncertainty of the renormalization constants.

2.13 Extraction of J^{u-d}

The GFFs $A_{20}^q(0)$ and $B_{20}^q(t)$ are of particular interest since for t = 0 they are related to the total angular momentum (the Ji sum rule [26]).

$$J^{u-d} = \frac{1}{2}\left[A_{20}^{u-d}(0) + B_{20}^{u-d}(0)\right]. \tag{2.37}$$

In order to estimate J^{u-d} at the physical pion mass, we analyze our data for A_{20}^{u-d}(t) and B_{20}^{u-d}(t), employing the BChPT formulas of Ref. [64] truncated at order m_π^3. In

Fig. 2.20, we present the resulting fits for t = 0, where only in the case of A_{20}^{u-d} we can directly compare to data points.

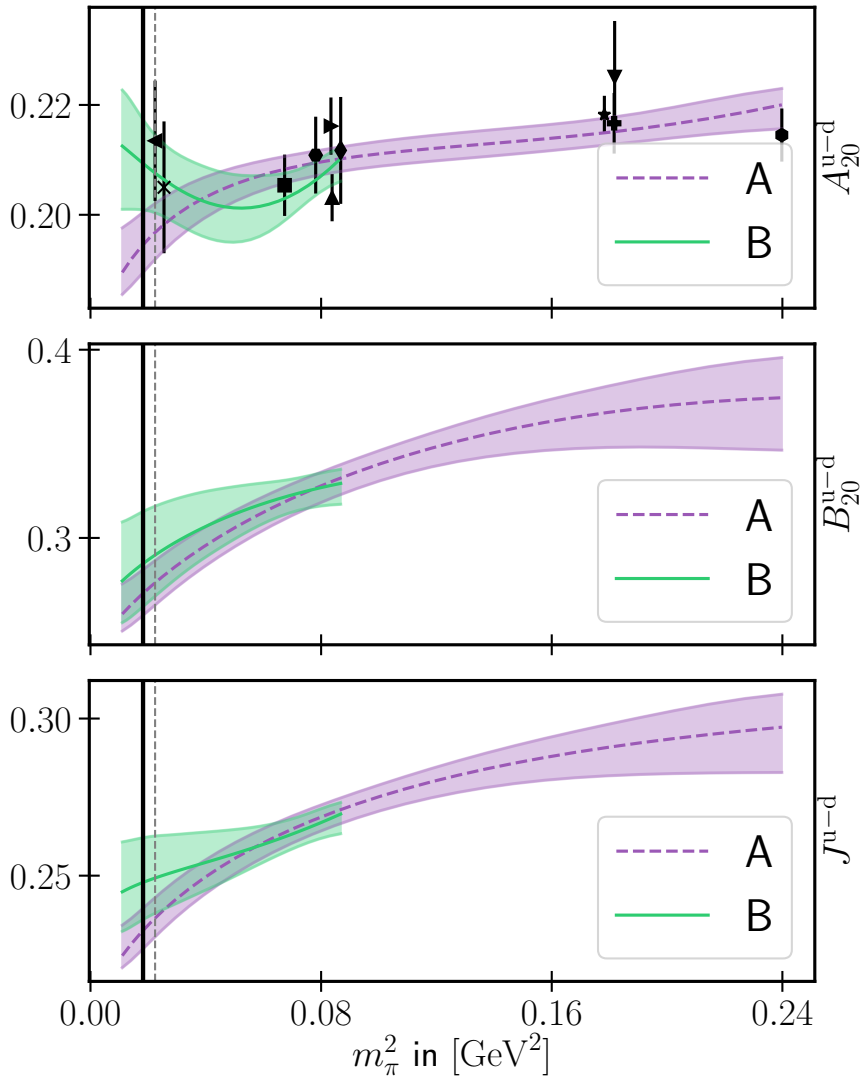

Figure 2.20: From top to bottom $A_{20}^{u-d}(0)$, $B_{20}^{u-d}(0)$ and J^{u-d} as a function of the pion mass squared. The vertical solid line marks the physical pion mass; the vertical dashed line indicates our smallest pion mass. The A-band is from a fit of all our ensembles and the B-band from a fit where ensembles with $m_\pi > 300\,\text{MeV}$ are removed. For $A_{20}^{u-d}(0)$, we have lattice data which are shown in the top panel for comparison. Taken from Ref [5].

The fits in Fig. 2.20 are parametrized by

$$A_{20}^{u-d}(\mathrm{t}, m_\pi) = \left[1 - \frac{(1+3\,g_A^2)\,m_\pi^2\,\log(\frac{m_\pi^2}{\mu^2})}{16\,f_\pi^2\,\pi^2}\right] L + m_\pi^2\,M_2^A + m_\pi^3\,M_3^A + \mathrm{t}(\,T_0^A + m_\pi^2\,T_1^A)\,, \tag{2.38}$$

$$B_{20}^{u-d}(\mathrm{t}, m_\pi) = \frac{g_A^2\, m_\pi^2\, \log(\frac{m_\pi^2}{\mu^2})}{16\, f_\pi^2\, \pi^2} L + \mathrm{t}(\, T_0^B + m_\pi^2\, T_1^B) + \left[1 - \frac{(1+2\,g_A^2)\, m_\pi^2 \log(\frac{m_\pi^2}{\mu^2})}{16\, f_\pi^2\, \pi^2}\right] L^B + m_\pi^2\, M_2^B\,. \tag{2.39}$$

It is not known in which range of $-\mathrm{t}$ and m_π BChPT is applicable. Therefore, we perform fits to all ensembles (set A) as well as fits using only ensembles with $m_\pi \leq 300\,\mathrm{MeV}$ (set B). The fit parameters T_1^A and T_1^B are manually added since our data extend up to virtualities $-\mathrm{t} \approx (770\,\mathrm{MeV})^2 \gg m_\pi^2$, however, these terms would naturally appear at the next order of BChPT. We determine the parameters $(L, M_2^A, M_3^A, T_0^A, T_1^A)$ and $(L, L^B, M_2^B, T_0^B, T_1^B)$ by carrying out combined fits to our data sets for $A_{20}^{u-d}(\mathrm{t}, m_\pi)$ and $B_{20}^{u-d}(\mathrm{t}, m_\pi)$. The remaining parameters in Eqs. (2.38) and (2.39) are constrained to $g_A = 1.256$, $f_\pi = 92.4\,\mathrm{MeV}$ and $\mu = 1.0\,\mathrm{GeV}$. For set A, the fit parameters have smaller statistical errors. For set B ,we see that A_{20}^{u-d} increases with $m_\pi \to m_\pi^{\mathrm{phy}}$. For both sets, we obtain values for χ^2_{dof} of about 0.75, hence we cannot use the χ^2_{dof} value to discriminate between the fit ranges. Instead, one may interpret the difference between fits A and B as a systematic uncertainty of the parameters. In Fig. 2.21 we show our fit for set A as a function of Q^2 at two fixed values of the pion masses ($m_\pi = 422\,\mathrm{MeV}$ and $150\,\mathrm{MeV}$, ensembles III and VIII). Obviously, our ansatz for the Q^2 and m_π^2 dependence describes the lattice data well. The final results are collected in Table 2.5, where the statistical errors are complemented by the uncertainties of the renormalization constants, which were estimated using the strategy described in section 2.11. Within the errors, our values agree with the isovector results of Ref. [65].

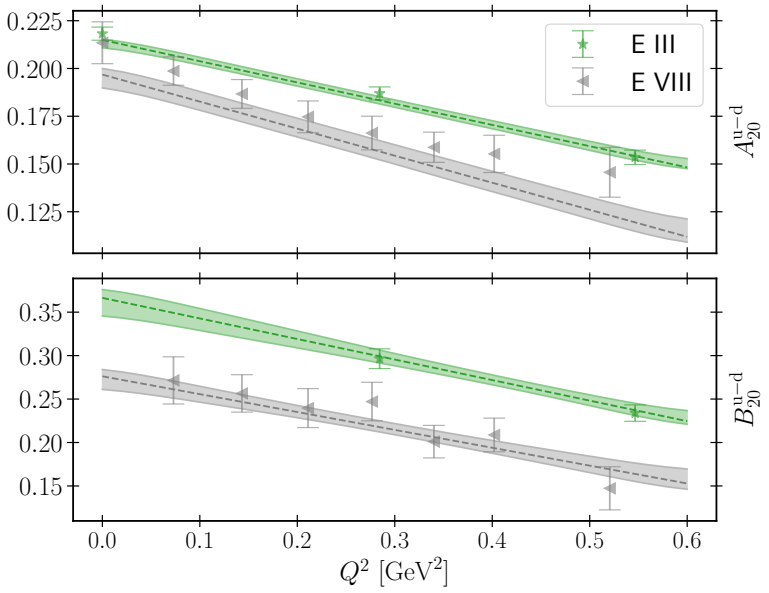

Figure 2.21: Chiral fit A versus Q^2 for two distinct pion masses: $m_\pi = 422\,\mathrm{MeV}$ (green) and $150\,\mathrm{MeV}$ (grey). The corresponding data points (ensemble III and VIII) are shown as well. Taken from Ref [5].

Ensemble selection	A	B
$A_{20}^{u-d}(0, m_\pi^{\text{phy}})$	0.195 (06) (03)	0.210 (08) (04)
$B_{20}^{u-d}(0, m_\pi^{\text{phy}})$	0.271 (13) (03)	0.287 (28) (04)
$J^{u-d}(m_\pi^{\text{phy}})$	0.233 (07) (03)	0.248 (14) (04)

Table 2.5: Results for $A_{20}^{u-d}(0, m_\pi)$, $B_{20}^{u-d}(0, m_\pi)$ and $J^{u-d}(m_\pi)$, extrapolated to the physical pion mass m_π^{phy} using the ensemble sets A and B. The first error is statistical, the second error is due to the uncertainty of the renormalization constants.

2.14 Nucleon tomography

We use our lattice results for the vector GFFs $A_{20}(\mathrm{t})$, $B_{20}(\mathrm{t})$ and the linear combination $\overline{B}_{T20}(\mathrm{t})$ [cf. Eq. (2.35)] in order to investigate the transverse spin density of the nucleon. To this end, we transform these GFFs to the impact parameter space $G(\mathrm{t}) \to G(\boldsymbol{b}_\perp^2)$ with

$$G\left(\boldsymbol{b}_\perp^2\right) = \int \frac{\mathrm{d}^2\Delta_\perp}{(2\pi)^2}\, e^{-i\boldsymbol{b}_\perp\cdot\Delta_\perp}\, G\left(\mathrm{t} = -\Delta_\perp^2\right)\,, \tag{2.40}$$

where we use the p-pole ansatz [66, 67]

$$G(\mathrm{t}) = \frac{G_0}{\left(1 - \mathrm{t}/m_p^2\right)^p} \tag{2.41}$$

for the interpolation of our lattice results. The impact parameter $\boldsymbol{b}_\perp$ is defined in the transverse x-y plane. It measures the transverse distance from the "center of momentum"

$$\boldsymbol{R}_\perp = \sum_i \boldsymbol{r}_{i\perp} x_i\,, \quad \sum_i x_i = 1\,, \tag{2.42}$$

where x_i is the momentum fraction of the ith parton [66, 68]. We define

$$\boldsymbol{b}_\perp \equiv (b_x,\, b_y)\,, \qquad b_\perp \equiv \sqrt{\boldsymbol{b}_\perp^2}\,. \tag{2.43}$$

To compute the transverse spin density, we also have to evaluate the derivative of $G(b_\perp^2)$ with respect to $b_\perp^2$,

$$G'(b_\perp^2) \equiv \frac{\partial}{\partial\, b_\perp^2}\, G(b_\perp^2). \tag{2.44}$$

The Fourier transform (2.40) of the p-pole ansatz (2.41) can be expressed in terms of the modified Bessel functions K_ν [66],

$$G(b_\perp^2) = \frac{G_0\, m_p^2\, (b_\perp m_p)^{p-1}\, K_{p-1}(b_\perp m_p)}{2^p\, \pi\, \Gamma(p)}\,. \tag{2.45}$$

The transverse spin density $\rho^q(x, \boldsymbol{b}_\perp, \boldsymbol{s}_\perp, \boldsymbol{S}_\perp)$ describes the probability to find a quark with longitudinal momentum fraction x, flavor q and transverse spin $\boldsymbol{s}_\perp$ at a distance $\boldsymbol{b}_\perp$ from the center of momentum of the nucleon with transverse spin $\boldsymbol{S}_\perp$. The explicit definition in terms of GPDs is given in Eq. (8) of Ref. [66]. Here, we consider the two transverse spin combinations,

$$\boldsymbol{s}_\perp = (1\,,0) \quad \text{and} \quad \boldsymbol{S}_\perp = (0\,,0)\,, \tag{2.46a}$$

$$\boldsymbol{s}_\perp = (0\,,0) \quad \text{and} \quad \boldsymbol{S}_\perp = (1\,,0)\,, \tag{2.46b}$$

where the first line describes a transversely polarized quark in an unpolarized nucleon and the second an unpolarized quark in a transversely polarized nucleon. In terms of GFFs the first moment of $\rho^q(x, \boldsymbol{b}_\perp, \boldsymbol{s}_\perp, \boldsymbol{S}_\perp)$ for these spin combinations reads

$$\begin{aligned}\langle\rho\rangle^q(\boldsymbol{b}_\perp, \boldsymbol{s}_\perp, \boldsymbol{S}_\perp) &= \int_{-1}^{1} \mathrm{d}x\, x\, \rho^q(x, \boldsymbol{b}_\perp, \boldsymbol{s}_\perp, \boldsymbol{S}_\perp) \\ &= \frac{1}{2} A_{20}^q(b_\perp^2) - \frac{\epsilon^{ij}\, b_\perp^j}{2m_N} \left(s_\perp^i\, \overline{B}_{T20}^{q\,\prime}(b_\perp^2) + S_\perp^i B_{20}^{q\,\prime}(b_\perp^2) \right)\,. \end{aligned} \tag{2.47}$$

For arbitrary spins $\boldsymbol{S}_\perp$ and $\boldsymbol{s}_\perp$ Eq. (2.47) will contain additional terms and we refer the reader to Refs. [66, 67]. We fit the GFFs for ensemble VI to the p-pole ansatz Eq. (2.41). Due to the thus limited number of data points, we restricted ourselves to the kinematic range $-\mathrm{t} \leq 0.6\,\mathrm{GeV}^2$, we find it impossible to simultaneously determine all three fit parameters, p, m_p and G_0. In particular the exponent p is strongly correlated with the pole mass m_p. This is demonstrated in Fig. 2.22. An increase of p results in a larger value of m_p, whereas χ^2_{dof} does not significantly change. Therefore, we cannot constrain p. This arbitrariness means it is difficult to obtain reliable, parametrization independent results for the moment $\langle\rho\rangle^q(\boldsymbol{b}_\perp, \boldsymbol{s}_\perp, \boldsymbol{S}_\perp)$ as a function of $\boldsymbol{b}_\perp$. This distribution has been studied in the past (see, e.g., [67]), but we find that its shape strongly depends on the value of p. In Fig. 2.23, we show $\langle\rho\rangle^q(\boldsymbol{b}_\perp, \boldsymbol{s}_\perp, \boldsymbol{S}_\perp)$ for $\boldsymbol{s}_\perp = (1, 0)$ and $\boldsymbol{S}_\perp = (0, 0)$ for four distinct values of p ranging from 1.45 up to 3.0. We see that with increasing p the density becomes less localized in the impact parameter plane and the maximum of the density is shifted away from the center. This also holds for other spin combinations.

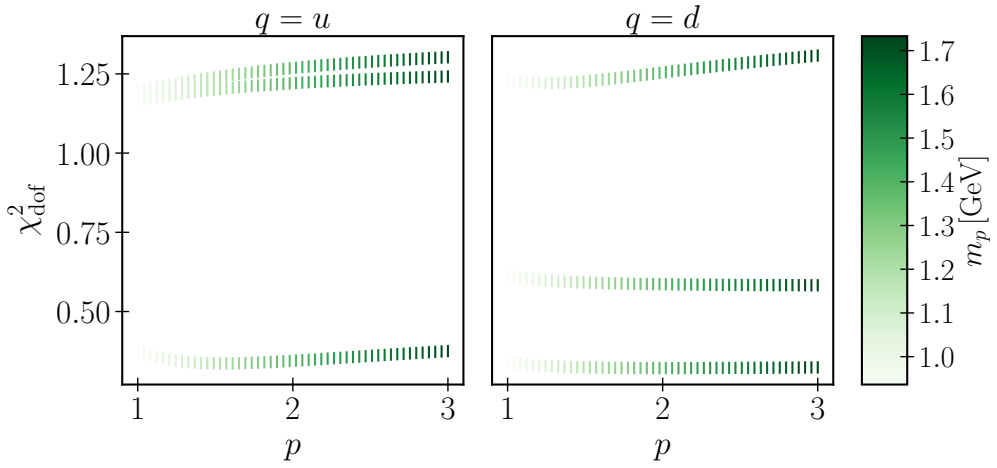

Figure 2.22: The pole mass m_p and χ^2_{dof} as a function of the fixed parameter p for ensemble VI. The colored lines correspond to fits to A^q_{20}, B^q_{20} and $\overline{B}^q_{T20}$ from top to bottom and flavor q from left to right. Taken from Ref [5].

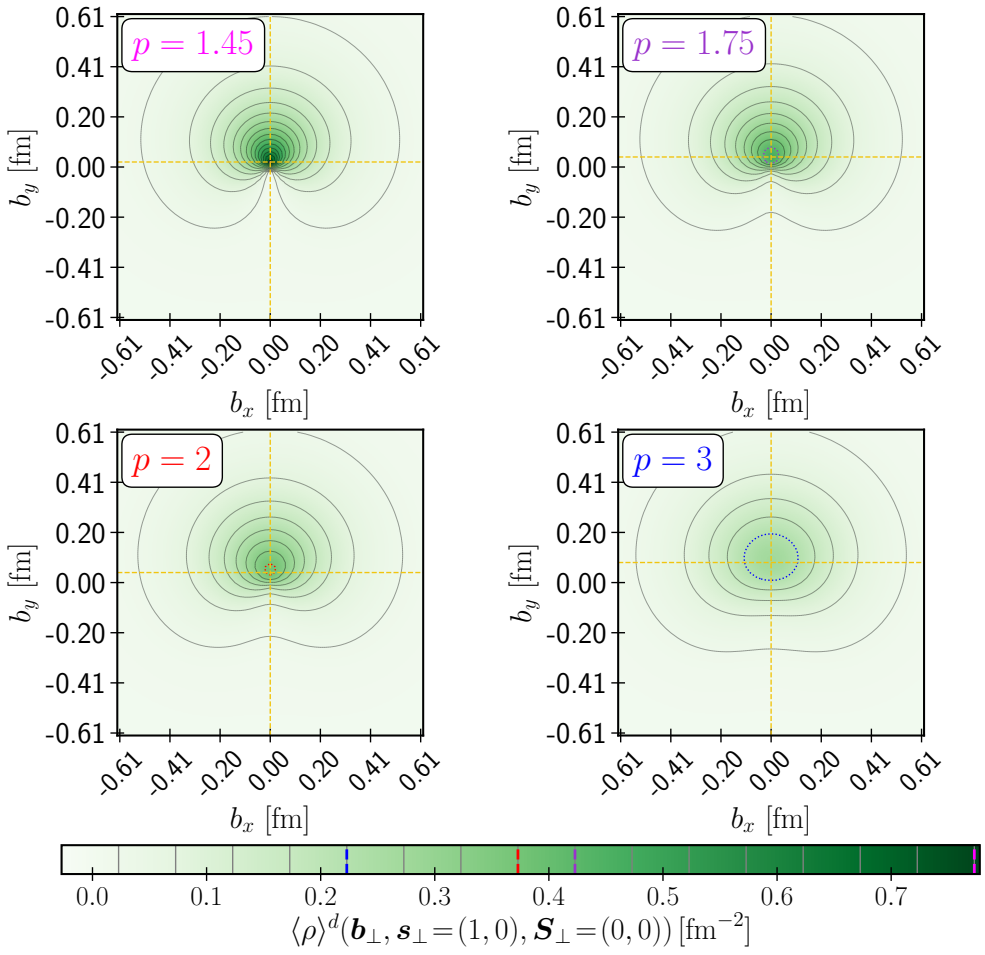

Figure 2.23: The p-dependence of the transverse spin density for a transversely polarized d-quark in an unpolarized nucleon. The yellow cross indicates the maximum of the density. The black contour lines are drawn equidistantly with a difference of 0.05. Taken from Ref [5].

However, we discovered that some integrated quantities have a much milder p-dependence, namely the half $\boldsymbol{b}_\perp$-integrated moments shown below

$$\langle\rho\rangle_+^q(\boldsymbol{s}_\perp, \boldsymbol{S}_\perp) = \frac{1}{Z_\rho}\int_{-\infty}^{+\infty} \mathrm{d}b_x \int_{0}^{+\infty} \mathrm{d}b_y \, \langle\rho\rangle^q(\boldsymbol{b}_\perp, \boldsymbol{s}_\perp, \boldsymbol{S}_\perp)\,, \tag{2.48a}$$

$$\langle\rho\rangle_-^q(\boldsymbol{s}_\perp, \boldsymbol{S}_\perp) = \frac{1}{Z_\rho}\int_{-\infty}^{+\infty} \mathrm{d}b_x \int_{-\infty}^{0} \mathrm{d}b_y \, \langle\rho\rangle^q(\boldsymbol{b}_\perp, \boldsymbol{s}_\perp, \boldsymbol{S}_\perp)\,, \tag{2.48b}$$

with the normalization factor

$$Z_\rho = \int_{-\infty}^{+\infty} \mathrm{d}b_x \int_{-\infty}^{+\infty} \mathrm{d}b_y \, \langle\rho\rangle^q(\boldsymbol{b}_\perp, \boldsymbol{s}_\perp, \boldsymbol{S}_\perp)\,. \tag{2.49}$$

The integrated moment $\langle\rho\rangle_+^q(\boldsymbol{s}_\perp, \boldsymbol{S}_\perp)$ is the probability, weighted with the longitudinal momentum fraction x, for finding a quark with flavor q in the upper part ($b_y \geq 0$) of the impact parameter space and $\langle\rho\rangle_-^q(\boldsymbol{s}_\perp, \boldsymbol{S}_\perp)$ is the x-weighted probability for finding a quark with flavor q in the lower part ($b_y \leq 0$). These integrated moments are a measure for the asymmetry of the transverse spin density. They depend much less on the value of p than $\langle\rho\rangle^q(\boldsymbol{b}_\perp, \boldsymbol{s}_\perp, \boldsymbol{S}_\perp)$ does. This is demonstrated in Fig. 2.24, where $\langle\rho\rangle_+^d$ and $\langle\rho\rangle_-^d$ are shown as functions of p for the transverse spin combination in Eq. (2.46a). Doubling p, both integrated moments change by only 5% and 15%, respectively. We find this mild p-dependence for all considered transverse spin and flavor combinations and consider these integrated moments as the better candidates for reliable lattice estimates.

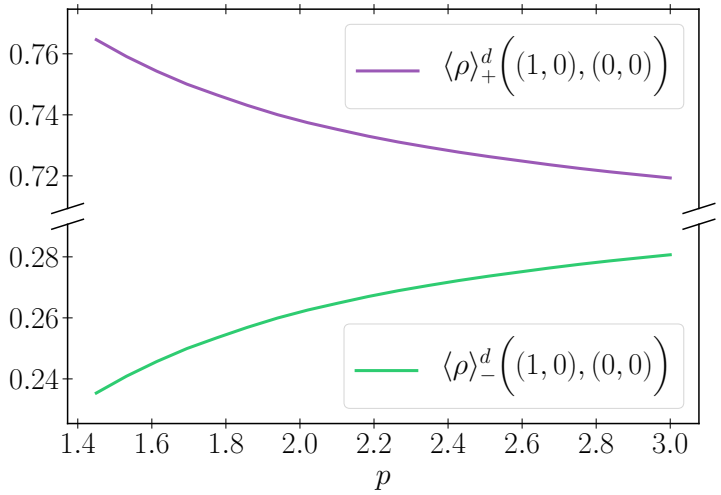

Figure 2.24: Dependence of $\langle\rho\rangle_+^d(\boldsymbol{s}_\perp, \boldsymbol{S}_\perp)$ and $\langle\rho\rangle_-^d(\boldsymbol{s}_\perp, \boldsymbol{S}_\perp)$ on the power p of the pole ansatz. The combination of transverse spins is $\boldsymbol{s}_\perp = (1, 0)$ and $\boldsymbol{S}_\perp = (0, 0)$. The errors are statistical only. The systematics due to the uncertainty of the power p amount to about 0.02. Taken from Ref [5].

Our results for $\langle\rho\rangle^q_\pm$ for up and down quark for our two transverse spin combinations (Eq. (2.46)) are shown in Fig. 2.25. The errors shown are statistical only. The figure corresponds to the power $p = 2$, and one may add systematic errors of about 0.02 due to the p-dependence; see Fig. 2.24. The numerical values are listed in Table 2.6. We see the probability of a transversely polarized u- or d-quark in an unpolarized nucleon is higher ($\sim 70\%$) in the $b_y > 0$ part of the impact parameter space than in the $b_y < 0$ part ($\sim 30\%$). For a transversely polarized nucleon, however, the probabilities of an unpolarized u- or d-quark differ: The unpolarized d-quark is more likely in the $b_y < 0$ part (67%), while a u-quark is more likely in the $b_y > 0$ part (60%) of the impact parameter space.

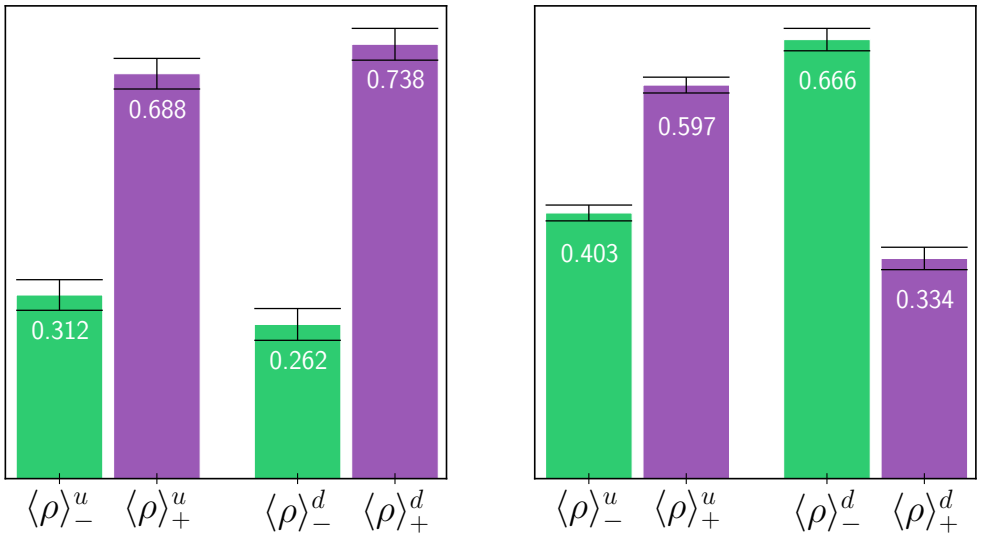

Figure 2.25: Probability (weighted with x) for finding a u- or d-quark in the upper/lower part ($b_y \lessgtr 0$) of the impact parameter space; left for a transversely polarized quark in an unpolarized nucleon; right for an unpolarized quark in a transversely polarized nucleon.

	$\boldsymbol{s}_\perp = (1\,,0)$ $\boldsymbol{S}_\perp = (0\,,0)$	$\boldsymbol{s}_\perp = (0\,,0)$ $\boldsymbol{S}_\perp = (1\,,0)$
$\langle\rho\rangle^u_-$	0.312 (26)	0.403 (12)
$\langle\rho\rangle^u_+$	0.688 (26)	0.597 (12)
$\langle\rho\rangle^d_-$	0.262 (27)	0.666 (17)
$\langle\rho\rangle^d_+$	0.738 (27)	0.334 (17)

Table 2.6: The half $\boldsymbol{b}_\perp$-integrated moments for $p = 2$, also shown in Fig. 2.25. The errors are statistical. The systematic error of the p-dependence is about 0.02.

3

Stochastic three-point functions

In this chapter, we present a new method to calculate lattice three-point functions. It is based on a factorization of the entire correlation function into two parts which are referred to as "spectator" and "insertion". Our method provides a serious alternative to the traditional sequential propagator method [56] which comes in two variants. The first is referred, as "sequential source through the operator" and the second is referred to as "fixed sink". Both methods require to fix certain parameters of the three-point correlation function. The "sequential source through the operator method" uses a fixed current for the inversion, i.e., the insertion operator, its timeslice and its momentum are fixed. Other parameters, like the sink timeslice and the interpolators can be chosen freely. The "fixed sink" method requires to fix the interpolating fields, the projection operator, the sink momentum, the sink timeslice and the flavor of the current used. This method has no restrictions regarding to the insertion operator, the timeslice as well as the current or source momentum. Both methods, however, yield rather restricted[1] sets of three-point functions. Our new stochastic method does not have restrictions of that kind. Once spectator and insertion are computed properly in a first step, one can use them in a second step, after the lattice measurement, to construct a three-point function with all spin indices open[2]. The three-point function with open indices can be used to generate a family of three-point functions by contracting the open indices with suitable polarization and γ-matrices. This two-step approach is new and extends previous works on stochastic methods for the computation of hadronic matrix

[1] The methods are not restrictive in principle, however, they are to expensive too be used for the creation of larger sets of three-point functions.

[2] Also flavor and momenta indices are open to a large extent.

elements [69, 70, 71, 72, 73].

To reduce the additional statistical error, originating from the stochastic estimator we implement forward-backward averaging by generating correlation functions of the hadron and the time reversed hadron. This step is of great importance because it comes with a marginal computational overhead and reduces the resulting statistical uncertainty considerably. We highlight that our method is capable to produce three-point functions with several source-sink separations at once. This provides a solid basis for excited states analysis of hadronic matrix elements which is an important subject and investigated by many groups [58, 74, 75, 76, 77, 78, 79, 80, 81, 82, 83, 84, 85]. Our new approach is most beneficial if one considers to compute many different momentum combinations and/or multiple hadrons. This is especially true if one aims to construct meson and baryon three-point functions because the insertion is designed such that it can be used for both types of hadrons. Moreover, we are able to calculate three-point functions with one covariant symmetric derivative. In this case, only the insertion is affected and the spectators remain fully unchanged. Our method is very convenient for the computation of GFFs because we are able to produce three-point functions with many combinations of polarizations and momenta. The combinations can be used for averaging which helps to obtain GFFs with smaller statistical uncertainties. Further, we are able to study SU(3) flavor symmetry breaking which requires multiple baryonic interpolators [86]. Our implementation makes it also possible to study physics which is governed by three-point correlation functions with flavor changing currents.

3.1 Generic baryon interpolators

In order to create and destroy baryon states on the lattice we use objects which are commonly called interpolators. We restrict ourself to color singlet interpolators containing three local quark fields which have the generic from for annihilation and creation interpolators

$$\mathcal{B}(x_4', \boldsymbol{x}')^{\tau'}_{ABC} \equiv \epsilon_{a'b'c'} \, (\Gamma_1)^{\tau'\alpha'} \, (\Gamma_2)^{\beta'\gamma'} \, \Psi_A(x_4', \boldsymbol{x}')^{\alpha'}_{a'} \, \Psi_B(x_4', \boldsymbol{x}')^{\beta'}_{b'} \, \Psi_C(x_4', \boldsymbol{x}')^{\gamma'}_{c'} \tag{3.1}$$

$$\overline{\mathcal{B}}(x_4, \boldsymbol{x})^{\tau}_{CBA} \equiv \epsilon_{abc} \, (\overline{\Gamma}_2)^{\gamma\beta} \, (\overline{\Gamma}_1)^{\alpha\tau} \, \overline{\Psi}_C(x_4, \boldsymbol{x})^{\gamma}_{c} \, \overline{\Psi}_B(x_4, \boldsymbol{x})^{\beta}_{b} \, \overline{\Psi}_A(x_4, \boldsymbol{x})^{\alpha}_{a} \tag{3.2}$$

and are parametrized by the flavor indices A, B, C and the matrices Γ_1 and Γ_2. The spin indices (superscript Greek letters) of the matrices are contracted with the indices of the quark fields (Ψ) where we use the Einstein sum convention. Color indices, represented by subscript Latin letters, are contracted (Einstein sum convention) with

the totally antisymmetric tensor. Furthermore, we define

$$\overline{\Psi}(x_4, \boldsymbol{x})^{\alpha}_{a} \equiv \Psi^*(x_4, \boldsymbol{x})^{\mu}_{a} \, (\gamma_4)^{\mu\alpha} \, . \tag{3.3}$$

The generic baryon creation interpolator is constructed according to (cf. Eq.(3.1, 3.2))

$$\overline{\mathcal{B}}(x_4, \boldsymbol{x})^{\tau}_{CBA} \equiv \mathcal{B}^*_{ABC}(x_4, \boldsymbol{x})^{\mu} \, (\gamma_4)^{\mu\tau} \, . \tag{3.4}$$

This requires the evaluation of complex conjugation of three Grassmann valued quark fields. Here we us, the convention $(\Psi_A \Psi_B)^* = \Psi^*_B \Psi^*_A$, where no additional minus sign occurs and exploit Eq. (3.3). An explicit calculation yields the following relations (using $\gamma_4 \gamma_4 = 1$)

$$\overline{\Gamma}_1 = \gamma_4 \Gamma_1^{\dagger} \gamma_4 \, , \quad \overline{\Gamma}_2 = \gamma_4 \Gamma_2^{\dagger} \gamma_4 \, . \tag{3.5}$$

In this work we use the γ-matrices defined in appendix A.1.

3.1.1 Example (Nucleon)

The generic baryon interplators can take the form of all interpolators which are commonly used in lattice QCD. For instance, one can set $A = u$, $B = u$, $C = d$, $\Gamma_1 = 1$ and $\Gamma_2 = C\gamma_5$ to obtain a spin 1/2 nucleon annihilation interplator

$$\mathcal{B}(x'_4, \boldsymbol{x'})^{\tau'}_{uud} = \epsilon_{a'b'c'} \, (1)^{\tau'\alpha'} \, (C\gamma_5)^{\beta'\gamma'} \, \Psi_u(x'_4, \boldsymbol{x'})^{\alpha'}_{a'} \, \Psi_u(x'_4, \boldsymbol{x'})^{\beta'}_{b'} \, \Psi_d(x'_4, \boldsymbol{x'})^{\gamma'}_{c'} \, . \tag{3.6}$$

The corresponding creation interpolator is defined by Eq. (3.2) and Eq. (3.5).

3.2 Generic current interpolator

In addition to the generic baryon annihilation and creation interpolators we define a generic current interpolator

$$\mathcal{J}(y_4, \boldsymbol{y})_{DE} \equiv \overline{\Psi}_D(y_4, \boldsymbol{y})^{\mu}_{d} \, (\Gamma_3)^{\mu\nu} \, \Psi_E(y_4, \boldsymbol{y})^{\nu}_{d} \, . \tag{3.7}$$

It is parametrized by two generic flavor indices D and E. We remark, that for $D \neq E$ one has a flavor changing current. Similar to the case of the generic baryon interpolators we use the matrix Γ_3 as a placeholder.

3.2.1 Example

The generic current interpolator can be used to construct a set of actual current interpolators. For instance, the vector current with $\overline{u}u$-flavor is obtained by $D = E = u$ and $\Gamma_3 = \gamma_4$.

3.3 Time reversed interpolators

The time reversal operation $\mathcal{T}$ is a discrete symmetry on the lattice and plays a crucial role in this work. The action of $\mathcal{T}$ on the quark fields is given by

$$\Psi_F(x_4,\,\boldsymbol{x})^{\alpha}_{a} \;\xrightarrow{\mathcal{T}}\; (\gamma_4\,\gamma_5)^{\alpha\beta}\,\Psi_F(-x_4\,,\boldsymbol{x})^{\beta}_{a}\,, \tag{3.8a}$$

$$\overline{\Psi}_F(x_4\,,\boldsymbol{x})^{\alpha}_{a} \;\xrightarrow{\mathcal{T}}\; \overline{\Psi}_F(-x_4\,,\boldsymbol{x})^{\beta}_{a}\,(\gamma_5\,\gamma_4)^{\beta\alpha}\,. \tag{3.8b}$$

Applying $\mathcal{T}$ to the generic current interpolator yields the time reversed current (cf. Eq. (3.7))

$$\mathcal{J}(y_4\,,\boldsymbol{y}) \xrightarrow{\mathcal{T}}\; \overline{\Psi}_D(-y_4\,,\boldsymbol{y})^{\mu}_{d}\,(\,\gamma_5\,\gamma_4\,\Gamma_3\,\gamma_4\,\gamma_5\,)^{\mu\nu}\;\Psi_E(-y_4\,,\boldsymbol{y})^{\nu}_{d}\,. \tag{3.9}$$

This demonstrates, that the action of $\mathcal{T}$ can be absorbed in the definition of Γ_3

$$(\Gamma_3)^{\mu\nu} \;\xrightarrow{\mathcal{T}}\; (\gamma_5\,\gamma_4\,\Gamma_3\,\gamma_4\,\gamma_5)^{\mu\nu}\,. \tag{3.10}$$

3.4 Time reversed matrices

As for the current, discussed above, one can apply $\mathcal{T}$ to the generic baryon interpolators in Eqs. (3.1, 3.2). The results of all calculations[3] are summarized in Table 3.1.

	Γ_1	Γ_2	$\overline{\Gamma}_1$	$\overline{\Gamma}_2$	Γ_3
$\mathcal{T}$	$\Gamma_1\gamma_4\gamma_5$	$\gamma_5\gamma_4\Gamma_2\gamma_4\gamma_5$	$\gamma_5\gamma_4\overline{\Gamma}_1$	$\gamma_5\gamma_4\overline{\Gamma}_2\gamma_4\gamma_5$	$\gamma_5\gamma_4\Gamma_3\gamma_4\gamma_5$

Table 3.1: Replacement rules for Γ-matrices.

3.5 Example: Generic Wick contractions

This section is meant as an introduction to techniques used for the computation of stochastic three-point functions with open spin indices which is addressed later. However, the used techniques can be understood more easily in the simpler case of two-point functions. The generic interpolators play a fundamental role for both cases. We start form a momentum space two-point correlation function

$$C(\boldsymbol{p}'|x_4',x_4) \equiv \left\langle \sum_{\boldsymbol{x}'} \mathcal{P}^{\tau\tau'} \left\langle \mathcal{B}(x_4',\boldsymbol{x}')^{\tau'}_{ABC}\,\overline{\mathcal{B}}(x_4,\boldsymbol{x})^{\tau}_{CBA} \right\rangle_W \mathrm{e}^{-\mathrm{i}\boldsymbol{p}'\cdot(\boldsymbol{x}'-\boldsymbol{x})} \right\rangle\,, \tag{3.11}$$

expressed in terms of the generic baryon interplators defined in Eqs. (3.1, 3.2). We introduced a not further specified parity projection operator $\mathcal{P}$. The big brackets

[3] We explicitly use $\gamma_5^T = \gamma_5$ and $\gamma_4^T = \gamma_4$.

$\langle \ldots \rangle$ are used to denote the ensemble average and $\langle \ldots \rangle_W$ denotes the Wick contraction. The generic baryon interpolators in Eq. (3.11) contain Γ-matrices which are not affected by the Wick contraction. This motivates the following factorization

$$C(\boldsymbol{p}', |x_4', x_4) = \mathcal{P}^{\tau\tau'} \, \mathcal{S}^{\tau'\alpha'\beta'\gamma'\gamma\beta\alpha\tau} \Big\langle \mathcal{C}(\boldsymbol{p}', |x_4', x_4)^{\alpha'\alpha\beta\beta'\gamma'\gamma} \Big\rangle \,, \tag{3.12}$$

with the spin tensor $\mathcal{S}$

$$\mathcal{S}^{\tau'\alpha'\beta'\gamma'\gamma\beta\alpha\tau} = (\Gamma_1)^{\tau'\alpha'} \, (\Gamma_2)^{\beta'\gamma'} \, (\overline{\Gamma}_2)^{\gamma\beta} \, (\overline{\Gamma}_1)^{\alpha\tau} \,, \tag{3.13}$$

and the momentum space two-point function with open spin indices

$$\begin{aligned} &\mathcal{C}(\boldsymbol{p}' \,|\, x_4', x_4)^{\alpha'\alpha\beta'\beta\gamma'\gamma} \equiv \sum_{\boldsymbol{x}'} \mathrm{e}^{-\mathrm{i}\boldsymbol{p}'\cdot(\boldsymbol{x}'-\boldsymbol{x})} \\ &\times \epsilon_{a'b'c'} \, \epsilon_{abc} \Big\langle \Psi_A(x')^{\alpha'}_{a'} \, \Psi_B(x')^{\beta'}_{b'} \, \Psi_C(x')^{\gamma'}_{c'} \, \overline{\Psi}_C(x)^{\gamma}_{a} \, \overline{\Psi}_B(x)^{\beta}_{b} \, \overline{\Psi}_A(x)^{\alpha}_{c} \Big\rangle_W \,, \end{aligned} \tag{3.14}$$

using $x = (x_4, \boldsymbol{x})$.

3.5.1 Observation I

The Wick contraction in the second line of Eq. (3.14) plays a fundamental role in this work. Generally speaking, a Wick contraction is a combinatorial problem where annihilation operators must be contracted with creation operators yielding a set of quark propagators. The contraction procedure has to be repeated for all possible combinations. It is important to understand the following: *To be able to calculate the contractions one has to know the flavors of the field operators*. For now, let us assume $A = B = C = u$ which yields

$$\begin{aligned} &\sum_{\boldsymbol{x}'} \Big\{ \epsilon_{a'b'c'} \, \epsilon_{abc} \, \Big\langle \Psi_u(x')^{\alpha'}_{a'} \, \Psi_u(x')^{\beta'}_{b'} \, \Psi_u(x')^{\gamma'}_{c'} \, \overline{\Psi}_u(x)^{\gamma}_{c} \, \overline{\Psi}_u(x)^{\beta}_{b} \, \overline{\Psi}_u(x)^{\alpha}_{a} \, \Big\rangle_W \Big\} \, \mathrm{e}^{-\mathrm{i}\boldsymbol{p}'\cdot(\boldsymbol{x}'-\boldsymbol{x})} = \\ &\sum_{\boldsymbol{x}'} \Big\{ \epsilon_{a'b'c'} \, \epsilon_{abc} \, (+1) G_u(x'|x)^{\alpha'\gamma}_{a'c} \, (-1) G_u(x'|x)^{\beta'\beta}_{b'b} \, (+1) G_u(x'|x)^{\gamma'\alpha}_{c'a} \\ &\quad + \epsilon_{a'b'c'} \, \epsilon_{abc} \, (+1) G_u(x'|x)^{\alpha'\gamma}_{a'c} \, (+1) G_u(x'|x)^{\beta'\alpha}_{b'a} \, (+1) G_u(x'|x)^{\gamma'\beta}_{c'b} \\ &\quad + \epsilon_{a'b'c'} \, \epsilon_{abc} \, (-1) G_u(x'|x)^{\alpha'\beta}_{a'b} \, (-1) G_u(x'|x)^{\beta'\gamma}_{b'c} \, (+1) G_u(x'|x)^{\gamma'\alpha}_{c'a} \\ &\quad + \epsilon_{a'b'c'} \, \epsilon_{abc} \, (-1) G_u(x'|x)^{\alpha'\beta}_{a'b} \, (+1) G_u(x'|x)^{\beta'\alpha}_{b'a} \, (+1) G_u(x'|x)^{\gamma'\gamma}_{c'c} \\ &\quad + \epsilon_{a'b'c'} \, \epsilon_{abc} \, (+1) G_u(x'|x)^{\alpha'\alpha}_{a'a} \, (-1) G_u(x'|x)^{\beta'\gamma}_{b'c} \, (+1) G_u(x'|x)^{\gamma'\beta}_{c'b} \\ &\quad + \epsilon_{a'b'c'} \, \epsilon_{abc} \, (+1) G_u(x'|x)^{\alpha'\alpha}_{a'a} \, (+1) G_u(x'|x)^{\beta'\beta}_{b'b} \, (+1) G_u(x'|x)^{\gamma'\gamma}_{c'c} \Big\} \, \mathrm{e}^{-\mathrm{i}\boldsymbol{p}'\cdot(\boldsymbol{x}'-\boldsymbol{x})} \,. \end{aligned} \tag{3.15}$$

This calculation shows, that a (non-trivial) Wick contraction of six field operators gives a sum of products of propagators with contraction specific signs (± 1). The Wick contraction acts non-trivially on the spin and color indices of the field operators and the propagators. The non-trivial color index structure is removable by exploiting the

symmetry properties of the two epsilon tensors. We introduce two sign correction factors (red) in front of the epsilon tensors

$$
\begin{aligned}
&\sum_{x'} \Big\{ \epsilon_{a'b'c'}\, \epsilon_{abc} \left\langle \Psi_u(x')^{\alpha'}_{a'}\, \Psi_u(x')^{\beta'}_{b'}\, \Psi_u(x')^{\gamma'}_{c'}\, \overline{\Psi}_u(x)^{\gamma}_{c}\, \overline{\Psi}_u(x)^{\beta}_{b}\, \overline{\Psi}_u(x)^{\alpha}_{a} \right\rangle_W \Big\}\, \mathrm{e}^{-\mathrm{i}\boldsymbol{p}'\cdot(\boldsymbol{x}'-\boldsymbol{x})} = \\
&\sum_{x'} \Big\{ (+1)\epsilon_{a'\,b'\,c'}(-1)\epsilon_{a\,b\,c}(+1) G_u(x'|x)^{\alpha'\,\gamma}_{a'\,a}(-1) G_u(x'|x)^{\beta'\,\beta}_{b'\,b}(+1) G_u(x'|x)^{\gamma'\,\alpha}_{c'\,c} \\
&\quad +(+1)\epsilon_{a'\,b'\,c'}(+1)\epsilon_{a\,b\,c}(+1) G_u(x'|x)^{\alpha'\,\gamma}_{a'\,a}(+1) G_u(x'|x)^{\beta'\,\alpha}_{b'\,b}(+1) G_u(x'|x)^{\gamma'\,\beta}_{c'\,c} \\
&\quad +(+1)\epsilon_{a'\,b'\,c'}(+1)\epsilon_{a\,b\,c}(-1) G_u(x'|x)^{\alpha'\,\beta}_{a'\,a}(-1) G_u(x'|x)^{\beta'\,\gamma}_{b'\,b}(+1) G_u(x'|x)^{\gamma'\,\alpha}_{c'\,c} \\
&\quad +(+1)\epsilon_{a'\,b'\,c'}(-1)\epsilon_{a\,b\,c}(-1) G_u(x'|x)^{\alpha'\,\beta}_{a'\,a}(+1) G_u(x'|x)^{\beta'\,\alpha}_{b'\,b}(+1) G_u(x'|x)^{\gamma'\,\gamma}_{c'\,c} \\
&\quad +(+1)\epsilon_{a'\,b'\,c'}(-1)\epsilon_{a\,b\,c}(+1) G_u(x'|x)^{\alpha'\,\alpha}_{a'\,a}(-1) G_u(x'|x)^{\beta'\,\gamma}_{b'\,b}(+1) G_u(x'|x)^{\gamma'\,\beta}_{c'\,c} \\
&\quad +(+1)\epsilon_{a'\,b'\,c'}(+1)\epsilon_{a\,b\,c}(+1) G_u(x'|x)^{\alpha'\,\alpha}_{a'\,a}(+1) G_u(x'|x)^{\beta'\,\beta}_{b'\,b}(+1) G_u(x'|x)^{\gamma'\,\gamma}_{c'\,c} \Big\}\, \mathrm{e}^{-\mathrm{i}\boldsymbol{p}'\cdot(\boldsymbol{x}'-\boldsymbol{x})} .
\end{aligned}
\tag{3.16}
$$

This example allows us to explain how we use abstract tensor notation to give a closed expression for the Wick contraction in Eq. (3.14) without defining the flavor indices. Note that a tensor T_{abc} can be formally symmetrized by

$$
T_{\{abc\}} = \frac{1}{3!} \sum_{\pi\in\Sigma_3} T_{\pi(a)\,\pi(b)\,\pi(c)} \,, \tag{3.17}
$$

where π denotes an element of the symmetric group Σ_3 on three elements and $\{abc\}$ means symmetrization over the three indices. This kind of notation allows us to express Eq. (3.14) as

$$
\begin{aligned}
&\mathcal{C}(\boldsymbol{p}' \mid x'_4, x_4)^{\alpha'\alpha\beta'\beta\gamma'\gamma} \equiv \sum_{\omega\in\Omega} \epsilon'(\omega)\epsilon(\omega) \prod_{j=1}^{3} \sigma_j(\omega) \\
&\times \left(\sum_{x'} \epsilon_{a'b'c'}\, \epsilon_{abc}\, G_{\omega(A)}(x'|x)^{\omega(\alpha')\,\omega(\alpha)}_{a'\,a}\; G_{\omega(B)}(x'|x)^{\omega(\beta')\,\omega(\beta)}_{b'\,b}\; G_{\omega(C)}(x'|x)^{\omega(\gamma')\,\omega(\gamma)}_{c'\,c}\; \mathrm{e}^{-\mathrm{i}\boldsymbol{p}'\cdot(\boldsymbol{x}'-\boldsymbol{x})} \right) .
\end{aligned}
\tag{3.18}
$$

The right hand side of Eq. (3.18) contains a sum over all Wick contractions ω. How many Wick contractions are actually present is uniquely determined by the values of the three flavor indices A, B and C. Hence, we write $\omega \in \Omega$ which is a short hand notation for $\Omega \equiv \Omega(\{A, B, C\})$. The signs in Eq. (3.16) are realized by $\epsilon'(\omega)$, $\epsilon(\omega)$ and $\sigma_j(\omega)$. For notational convenience and later reference we define an overall sign function

$$
\sigma(\omega) \equiv \epsilon'(\omega)\epsilon(\omega) \prod_{j=1}^{3} \sigma_j(\omega) \,. \tag{3.19}
$$

3.5.2 Observation II

The two-point function with open spin in Eq. (3.18) can be written as,

$$\mathcal{C}(\boldsymbol{p}' \mid x_4', x_4)^{\alpha'\alpha\beta'\beta\gamma'\gamma} \equiv \sum_{\omega\in\Omega} \sigma(\omega)\, T(\boldsymbol{p}' \mid x_4', x_4)^{\omega(\alpha')\omega(\alpha)\omega(\beta')\omega(\beta)\omega(\gamma')\omega(\gamma)}_{\omega(A)\omega(B)\omega(C)} , \tag{3.20}$$

where we defined the two-point function tensor T

$$\begin{aligned} &T(\boldsymbol{p}' \mid x_4', x_4)^{\omega(\alpha')\omega(\alpha)\omega(\beta')\omega(\beta)\omega(\gamma')\omega(\gamma)}_{\omega(A)\omega(B)\omega(C)} \equiv \epsilon_{a'b'c'}\, \epsilon_{abc} \\ &\times \sum_{x'} G_{\omega(A)}(x'|x)^{\omega(\alpha')\,\omega(\alpha)}_{a'\,a}\; G_{\omega(B)}(x'|x)^{\omega(\beta')\,\omega(\beta)}_{b'\,b}\; G_{\omega(C)}(x'|x)^{\omega(\gamma')\,\omega(\gamma)}_{c'\,c}\; \mathrm{e}^{-\mathrm{i}\boldsymbol{p}'\cdot(\boldsymbol{x}'-\boldsymbol{x})} . \end{aligned} \tag{3.21}$$

The remarkable point about this ansatz is the following. By measuring

$$\begin{aligned} &T(\boldsymbol{p}' \mid x_4', x_4)^{\alpha'\alpha\beta'\beta\gamma'\gamma}_{ABC} \equiv \epsilon_{a'b'c'}\, \epsilon_{abc} \\ &\times \sum_{x'} G_A(x'|x)^{\alpha'\alpha}_{a'a}\; G_B(x'|x)^{\beta'\beta}_{b'b}\; G_C(x'|x)^{\gamma'\gamma}_{c'c}\; \mathrm{e}^{-\mathrm{i}\boldsymbol{p}'\cdot(\boldsymbol{x}'-\boldsymbol{x})} \end{aligned} \tag{3.22}$$

on a set of gauge configurations one can construct any baryon two-point correlator

$$\begin{aligned} C(\boldsymbol{p}', |x_4', x_4) &= \mathcal{P}^{\tau\tau'}\, \mathcal{S}^{\tau'\alpha'\beta'\gamma'\gamma\beta\alpha\tau} \Big\langle \mathcal{C}(\boldsymbol{p}', |x_4', x_4)^{\alpha'\alpha\beta\beta'\gamma'\gamma} \Big\rangle , \\ C(\boldsymbol{p}', |x_4', x_4) &= \mathcal{P}^{\tau\tau'}\, \mathcal{S}^{\tau'\alpha'\beta'\gamma'\gamma\beta\alpha\tau} \sum_{\omega\,\in\,\Omega} \sigma(\omega) \Big\langle T(\boldsymbol{p}' \mid x_4', x_4)^{\omega(\alpha')\omega(\alpha)\omega(\beta')\omega(\beta)\omega(\gamma')\omega(\gamma)}_{\omega(A)\omega(B)\omega(C)} \Big\rangle . \end{aligned} \tag{3.23}$$

The two-point function tensor T, defined in Eq. (3.22) can be generated by a set of point-to-all propagators with different flavors sourced at x. In this case one can set the temporal source position to $x_4 = 0$ which is justified by translational invariance.

3.5.3 Observation III

In contrast to traditional approaches one can compute the Wick contractions after the lattice measurement of T (cf. Eq. (3.22)) by virtue of Eq. (3.23). This is accomplished by the computation of the ω-functions which are bijective functions acting on the set of spin and flavor indices

$$\begin{aligned} &\omega : S_{\text{spin}} \otimes S_{\text{flavor}} \to S_{\text{spin}} \otimes S_{\text{flavor}} , \\ &S_{\text{spin}} = \{\alpha' , \alpha , \beta' , \beta , \gamma' , \gamma\} , \\ &S_{\text{flavor}} = \{A , B , C\} . \end{aligned}$$

They do not act on color indices due to the sign correction function. This is important for implementations because it reduces the number of open indices considerably. Finally one must also calculate the overall sign correction function $\sigma(\omega)$.

3.5.4 Practical remarks for generic Wick contractions

To compute the sign correction functions $\epsilon'(\omega)$, $\epsilon(\omega)$, $\sigma_j(\omega)$ and the ω-functions we developed a **Python** package called *wick* [87]. The listing 3.5.1 gives an example for how the *wick* package is used. The shown code implements Eq. (3.16). We use *wick* as a library for the computation of stochastic three-point.

Listing 3.5.1: Implementation of Eq. (3.16) using the *wick* package.

```
from wick import core
from wick.flavors import U
from wick.tensor import Tensor, TotallyAntiSymmetric as TAS
from wick.field_operators import Annihilator as Ao, Creator as Co

# Epsion tensors
c1 = (r'a^\prime', r'b^\prime', r'c^\prime')
t1 = Tensor(r'\epsilon', ColorSym=TAS).add_color_index(*c1)
c2 = ( r'a', r'b', r'c')
t2 = Tensor(r'\epsilon', ColorSym=TAS).add_color_index(*c2)

# Annihilation fields
f1 = U(Ao(), spin=r"\alpha^\prime",color=r"a^\prime",position=r"x^\prime")
f2 = U(Ao(), spin=r"\beta^\prime", color=r"b^\prime",position=r"x^\prime")
f3 = U(Ao(), spin=r"\gamma^\prime",color=r"c^\prime",position=r"x^\prime")

# Creation fields
f4 = U(Co(), spin=r"\gamma",       color=r"c",       position=r"x")
f5 = U(Co(), spin=r"\beta",        color=r"b",       position=r"x")
f6 = U(Co(), spin=r"\alpha",       color=r"a",       position=r"x")

# Calculate wick contraction, show all signs
contractions = core.wick_contraction(
  # Tensors
  t1, t2,                  # Add as many you need
  # Fields
  f1, f2, f3, f4, f5, f6, # Add as many you need
  # Options
  remove_disconnected=True,
  collect_signs=False,
  symmetries=[
    {
      'tensor': t1,
      'target_space': 'color',
      'target_order': t1.get_color_indices()
    },
    {
      'tensor': t2,
      'target_space': 'color',
      'target_order': t2.get_color_indices()
    },
  ]
)
# Replace jupyter with latex to obtain a plain latex equation
from wick.rendering.jupyter.contractions import View
View(contractions).create_view()
```

From line 7 to 10 we create two epsilon tensors. The six field operators are instantiated (line 12 to 20) and the Wick contraction is computed in line 23. The function "core.wick_contraction" has several options which we do not discuss here. However, we remark that the "symmetries" option is important for this example, it removes the non-trivial color structure with the two totally antisymmetric epsilon tensors "t1" and "t2" (cf. Eq. (3.15) and Eq. (3.16)). The contraction result can be displayed in a **Jupyter** notebook. Alternatively one can render a raw Latex equation.

3.5.5 Practical remarks for generic spin contractions

This section as a continuation of the last subsection ($A = B = C = u$). In particular we demonstrate how we accomplish the contraction with the matrices

$$C(\boldsymbol{p}', |x_4', x_4) = (\mathcal{P})^{\tau\tau'}(\Gamma_1)^{\tau'\alpha'}(\Gamma_2)^{\beta'\gamma'}(\overline{\Gamma}_2)^{\gamma\beta}(\overline{\Gamma}_1)^{\alpha\tau}\left\langle \mathcal{C}(\boldsymbol{p}', |x_4', x_4)^{\alpha'\alpha\beta\beta'\gamma'\gamma} \right\rangle \tag{3.25}$$

where we used Eq. (3.23) and the definition of the spin tensor Eq. (3.13). Note that Eq. (3.16) can be expressed in terms of the two-point correlation tensor

$$\begin{aligned}\mathcal{C}(\boldsymbol{p}', |x_4', x_4)^{\alpha'\alpha\beta\beta'\gamma'\gamma} &= T(x'|x)^{\alpha'\gamma\beta'\beta\gamma'\alpha}_{uuu} + T(x'|x)^{\alpha'\gamma\beta'\alpha\gamma'\beta}_{uuu} + T(x'|x)^{\alpha'\beta\beta'\gamma\gamma'\alpha}_{uuu} \\ &+ T(x'|x)^{\alpha'\beta\beta'\alpha\gamma'\gamma}_{uuu} + T(x'|x)^{\alpha'\alpha\beta'\gamma\gamma'\beta}_{uuu} + T(x'|x)^{\alpha'\alpha\beta'\beta\gamma'\gamma}_{uuu}\,.\end{aligned} \tag{3.26}$$

For reasons that will become clear soon we rename our spin indices with ASCII letters

$$\begin{aligned}\mathcal{C}(\boldsymbol{p}', |x_4', x_4)^{efdghc} &= T(x'|x)^{ecgdhf}_{uuu} + T(x'|x)^{ecgfhd}_{uuu} + T(x'|x)^{edgchf}_{uuu} \\ &+ T(x'|x)^{edgfhc}_{uuu} + T(x'|x)^{efgchd}_{uuu} + T(x'|x)^{efgdhc}_{uuu}\,.\end{aligned} \tag{3.27}$$

and do the same for Eq. (3.26) where we further define the matrices, momenta and Euclidean times to our disposal

$$\begin{aligned}C(\mathbf{0}|15, 0) = &\left(\frac{1+\gamma_4}{2}\right)^{ab}\left(1\right)^{be}\left(\gamma_2\gamma_4\gamma_5\right)^{gh}\left(\gamma_4\left(\gamma_2\gamma_4\gamma_5\right)^{\dagger}\gamma_4\right)^{cd}\left(\gamma_4(1)^{\dagger}\gamma_4\right)^{fa} \\ &\times\left\langle \mathcal{C}(\boldsymbol{p}', |x_4', x_4)^{efdghc} \right\rangle.\end{aligned} \tag{3.28}$$

Eq. (3.28) is implemented in Listing 3.5.2 (without loop over the number of measurements). We exploit the "numpy.einsum" function [88] to perform the contractions.

3.5.6 Summary

In this sub-section we demonstrated the main ideas of our two-step approach. To keep things simple we considered baryon two-point functions. However, the introduced concepts are applicable to hadronic three-point function as well. The following section is dedicated to finding the three-point function tensor T.

Listing 3.5.2: Implementation of Eq. (3.28) for $A = B = C = u$.

```
from numpy import einsum; from numpy.random import rand
from rioi.reader.stoch3pt.contractions.gamma_mat import Factory

def load_two_point_tensor_uuu(p_prime, x_4_prime , x_4):
  return rand(4,4,4,4,4,4) + 1.0j*rand(4,4,4,4,4,4)
# Setup matrices
m1 = Factory.create_from_string("(gi + gt)/2")
m2 = Factory.create_from_string("gi") # gi -> identiy
m3 = Factory.create_from_string("gy*gt*g5")
m4 = Factory.create_from_string("gt*H(gy*gt*g5)*gt")
m5 = Factory.create_from_string("gt*H(gi)*gt") # H -> hermitian conjugation
# Setup contractions
t = load_two_point_tensor((0,0,0), 15, 0)
signs, idx  = (1,1,1,1,1,1) , "ab,be,gh,cd,fa"
omegas = (
  f"{idx},ecgdhf", f"{idx},ecgfhd", f"{idx},edgchf",
  f"{idx},edgfhc", f"{idx},efgchd", f"{idx},efgdhc",
)
# Perform contractions
result = 0.0 + 0.0j
for sigma, omega in zip(signs, omegas):
  result  += sigma *  numpy.einsum(omega, m1, m2, m3, m4, m5, t)
```

3.6 Stochastic timeslice-to-all propagator

Let us now introduce another version of a lattice propagator, namely the stochastic timeslice-to-all propagator. This kind of propagator plays a crucial role for the computation of stochastically estimated three-point correlation functions. The key idea is to consider a set of randomly chosen complex $\mathbb{Z}_2$ noise vectors [89, 90]

$$\eta_i(x_4, \boldsymbol{x})_a^\alpha \equiv \begin{cases} \mathbb{Z}_2 \times \mathrm{i}\mathbb{Z}_2 & \text{if} \quad x_4 = x_4' \\ 0 & \text{otherwise} \end{cases} \tag{3.29}$$

with $i \in \{1, \ldots, N_{\text{sto}}\}$. Almost all elements of η_i are zero, only for time slice x_4' we have non-zero values. We say the noise vector η_i is seeded on time slice x_4'. For $N_{\text{sto}} \to \infty$ the average of all noise vectors yields the null-vector since all four complex numbers are equally distributed

$$\frac{1}{N_{\text{sto}}} \sum_{i=1}^{N_{\text{sto}}} \eta_i(x_4, \boldsymbol{x})_a^\alpha = 0_a^\alpha + \mathcal{O}\left(N_{\text{sto}}^{-\frac{1}{2}}\right). \tag{3.30}$$

One can use the set of noise vectors to define an estimator for the unit-matrix

$$\frac{1}{N_{\text{sto}}} \sum_{i=1}^{N_{\text{sto}}} \eta_i(x_4, \boldsymbol{x})_a^\alpha \, \eta_i^*(z_4, \boldsymbol{z})_c^\gamma = \delta_{x_4' x_4} \delta_{x_4' z_4} \delta_{\boldsymbol{x}\boldsymbol{z}} \delta_{\alpha\gamma} \delta_{ac} + \mathcal{O}\left(N_{\text{sto}}^{-\frac{1}{2}}\right). \tag{3.31}$$

In the following we demonstrate how we use the set of noise vectors to obtain a stochastic timeslice-to-all propagator. Therefore let us consider the linear problem

$$\sum_{y_4,\,\boldsymbol{y}} D_F(x_4,\boldsymbol{x}|y_4,\boldsymbol{y})^{\alpha\beta}_{ab}\, s_{F,i}(y_4,\boldsymbol{y})^{\beta}_{b} \;=\; \eta_i(x_4,\boldsymbol{x})^{\alpha}_{a}\,. \tag{3.32}$$

On the left hand side of this equation we have the known sparse Dirac operator D_F with flavor F and on the right hand side we consider a noise vector η_i which was generated according to Eq. (3.29). In a first step we generate a set of solution vectors $\{s_{F,i}\}$ by solving Eq. (3.32). This gives a set, namely $\{s_{F,i}\,,\eta_i\}$ which can be used to create a stochastic timeslice-to-all propagator. This is done as follows. One multiplies Eq. (3.32) from the right with $N_{\text{sto}}^{-1}\,\eta_i^*(z_4,\boldsymbol{z})^{\gamma}_{c}$ and performs a sum over the stochastic index i

$$\sum_{y_4\,\boldsymbol{y}} D_F(x_4,\boldsymbol{x}|y_4,\boldsymbol{y})^{\alpha\beta}_{ab}\;\left(N_{\text{sto}}^{-1}\sum_{i=1}^{N_{\text{sto}}} s_{F,i}(y_4,\boldsymbol{y})^{\beta}_{b}\cdot\eta_i^*(z_4,\boldsymbol{z})^{\gamma}_{c}\right) \;=\; N_{\text{sto}}^{-1}\sum_{i=1}^{N_{\text{sto}}}\eta_i(x_4,\boldsymbol{x})^{\alpha}_{a}\cdot\eta_i^*(z_4,\boldsymbol{z})^{\gamma}_{c}\cdot$$

$$\sum_{y_4\,\boldsymbol{y}} D_F(x_4',\boldsymbol{x}|y_4,\boldsymbol{y})^{\alpha\beta}_{ab}\;\left(N_{\text{sto}}^{-1}\sum_{i=1}^{N_{\text{sto}}} s_{F,i}(y_4,\boldsymbol{y})^{\beta}_{b}\cdot\eta_i^*(x_4',\boldsymbol{x}')^{\gamma}_{c}\right) \;\approx\; \delta_{\boldsymbol{x}\boldsymbol{x}'}\delta_{\alpha\gamma}\delta_{ac}\,. \tag{3.33}$$

The right hand side of this equations approaches the unit matrix for $N_{sto}\to\infty$. This means that the left hand side contains the inverse of the Dirac operator D_F for a fixed time slice x_4'

$$G_F(y_4,\boldsymbol{y}|x_4',\boldsymbol{x}')^{\beta\gamma}_{bc} = N_{\text{sto}}^{-1}\sum_{i=1}^{N_{\text{sto}}} s_{F,i}(y_4,\boldsymbol{y})^{\beta}_{b}\cdot\eta_i^*(x_4',\boldsymbol{x}')^{\gamma}_{c} + \mathcal{O}\left(N_{\text{sto}}^{-\frac{1}{2}}\right)\,. \tag{3.34}$$

3.7 Factorized baryon three-point function

We define the baryon momentum space three-point correlation function in terms of the generic interpolators (cf. Eqs. (3.1 ,3.2 ,3.7))

$$\begin{aligned} &C(\boldsymbol{p}',\boldsymbol{q}\,|\,x_4',y_4,x_4) = \\ &\times\left\langle \mathcal{P}^{\tau\tau'}\sum_{\boldsymbol{x}'\boldsymbol{y}}\left\langle \mathcal{B}(x_4',\boldsymbol{x}')^{\tau'}_{ABC}\,\mathcal{J}(y_4,\boldsymbol{y})_{DE}\;\overline{\mathcal{B}}(x_4,\boldsymbol{x})^{\tau}_{CBA}\right\rangle_W \mathrm{e}^{-\mathrm{i}\boldsymbol{p}'\cdot(\boldsymbol{x}'-\boldsymbol{x})}\;\mathrm{e}^{+\mathrm{i}\boldsymbol{q}\cdot(\boldsymbol{y}-\boldsymbol{x})}\right\rangle\,. \end{aligned} \tag{3.35}$$

We call $\boldsymbol{p}'$ the sink momentum and $\boldsymbol{q}$ the insertion momentum. Momentum conservation then automatically projects out the source momentum $\boldsymbol{p}=\boldsymbol{p}'-\boldsymbol{q}$. The spin factorized three-point function is given by

$$C(\boldsymbol{p}',\boldsymbol{q}\,|\,x_4',y_4,x_4) = \mathcal{P}^{\tau\tau'}\;\mathcal{S}^{\tau'\alpha'\beta'\gamma'\mu\nu\gamma\beta\alpha\tau}\left\langle \mathcal{C}(\boldsymbol{p}',\boldsymbol{q}\,|\,x_4',y_4,x_4)^{\alpha'\,\alpha\,\beta'\,\beta\,\gamma'\,\mu\,\nu\,\gamma}\right\rangle \tag{3.36}$$

with the spin tensor according to Eqs. (3.1 ,3.2 ,3.7)

$$\mathcal{S}^{\tau'\alpha'\beta'\gamma'\mu\nu\gamma\beta\alpha\tau} = (\Gamma_1)^{\tau'\alpha'}\ (\Gamma_2)^{\beta'\gamma'}\ (\Gamma_3)^{\mu\nu}\ (\overline{\Gamma}_2)^{\gamma\beta}\ (\overline{\Gamma}_1)^{\alpha\tau} \tag{3.37}$$

and the three-point function with open spin indices

$$\begin{aligned}\mathcal{C}(\boldsymbol{p}', \boldsymbol{q} \,|\, x_4', y_4, x_4)^{\alpha'\alpha\beta'\beta\gamma'\mu\nu\gamma} &\equiv \sum_{\boldsymbol{x}'\boldsymbol{y}} \mathrm{e}^{-\mathrm{i}\boldsymbol{p}'\cdot(\boldsymbol{x}'-\boldsymbol{x})}\ \mathrm{e}^{+\mathrm{i}\boldsymbol{q}\cdot(\boldsymbol{y}-\boldsymbol{x})}\ \epsilon_{a'b'c'}\ \epsilon_{abc} \\ &\times \left\langle \Psi_A(x')^{\alpha'}_{a'}\, \Psi_B(x')^{\beta'}_{b'}\, \Psi_C(x')^{\gamma'}_{c'}\, \overline{\Psi}_D(y)^{\mu}_{d}\, \Psi_E(y)^{\nu}_{d}\, \overline{\Psi}_C(x)^{\gamma}_{a}\, \overline{\Psi}_B(x)^{\beta}_{b}\, \overline{\Psi}_A(x)^{\alpha}_{c} \right\rangle_W .\end{aligned} \tag{3.38}$$

3.8 Connected baryon three-point Wick contractions

In this section we continue the factorization approach and study the generic structure of the Wick contractions defined in Eq. (3.38). We do not assume a specific flavor setup but ignore disconnected contributions which originate from the contraction of the operators on position y in case of $D = E$. These contributions can be taken into account in a separate analysis step. Without loss of generality, we consider the annihilation operator $\Psi_E(y)^{\nu}_{d}$. It must be contracted with a $\overline{\Psi}$ operator defined at the space-time position x yielding a propagator connecting the points $y \leftarrow x$. A non-trivial contraction requires that $\overline{\Psi}$ has flavor E which gives rise to a propagator with flavor E. Next, let us pick $\overline{\Psi}_D(y)^{\mu}_{d}$ which has to be contracted with a Ψ operator located at x' yielding a propagator with flavor D connecting the points $x' \leftarrow y$. The two remaining non-trivial contractions must produce propagators connecting $x' \leftarrow x$. However, we can not deduce anything about the flavors of the two propagators. Again, we can utilize abstract tensor notation to find a closed expression. Note that each propagator (four in total) has a certain contraction specific sign. We introduce sign functions $\sigma_j(\omega)$ with $j \in \{1, 2, 3, 4\}$ and remove the non-trivial color dependency with $\epsilon'(\omega)$ and $\epsilon(\omega)$. This yields

$$\begin{aligned}\mathcal{C}(\boldsymbol{p}', \boldsymbol{q} \,|\, x_4', y_4, x_4)^{\alpha'\alpha\beta'\beta\gamma'\mu\nu\gamma} &= \sum_{\omega\in\Omega} \epsilon'(\omega)\,\epsilon(\omega) \prod_{j=1}^{4} \sigma_j(\omega)\ \epsilon_{a'b'c'}\ \epsilon_{abc} \\ &\times \sum_{\boldsymbol{x}'\boldsymbol{y}} \Big\{ G_{\omega(A)}\big(x_4', \boldsymbol{x}' \,\big|\, x_4, \boldsymbol{x}\big)^{\omega(\alpha')\,\omega(\alpha)}_{a'a} \cdot G_{\omega(B)}\big(x_4', \boldsymbol{x}' \,\big|\, x_4, \boldsymbol{x}\big)^{\omega(\beta')\,\omega(\beta)}_{b'b} \\ &\cdot G_D\big(x_4', \boldsymbol{x}' \,\big|\, y_4, \boldsymbol{y}\big)^{\omega(\gamma')\,\mu}_{c'd} \cdot G_E\big(y_4, \boldsymbol{y} \,\big|\, x_4, \boldsymbol{x}\big)^{\nu\omega(\gamma)}_{dc} \Big\}\ \mathrm{e}^{-\mathrm{i}\boldsymbol{p}'(\boldsymbol{x}'-\boldsymbol{x})}\ \mathrm{e}^{+\mathrm{i}\boldsymbol{q}\cdot(\boldsymbol{y}-\boldsymbol{x})}\end{aligned} \tag{3.39}$$

The expression, as it is shown in Eq. (3.39) can not be directly implemented because the propagator with flavor D depends simultaneously on the spatial positions $\boldsymbol{x}'$ and $\boldsymbol{y}'$. Performing the required sum over $\boldsymbol{x}'$ and $\boldsymbol{y}'$ is an unfeasible numerical task. Furthermore, let us remark that the operator insertion timeslice y_4 can take any

position in the interval $x_4' > y_4 > x_4$. However, one can circumvented this problem with a stochastic time-slice-to-all propagator (cf. Eq. (3.34)). To make use of it, one inverts the propagation direction using γ_5-hermiticity

$$G_D(x_4', \boldsymbol{x'}|y_4, \boldsymbol{y})^{\omega(\gamma')\mu}_{c'd} = \frac{1}{N_{\text{sto}}} \sum_{i=1}^{N_{\text{sto}}} \eta_i(x_4', \boldsymbol{x'})^{\rho'}_{c'} \cdot (\gamma_5)^{\rho'\,\omega(\gamma')} \cdot (\gamma_5)^{\mu\rho} \cdot s^*_{D,i}(y_4, \boldsymbol{y})^{\rho}_{d} \,. \tag{3.40}$$

Inserting Eq. (3.40) into Eq. (3.39) yields

$$\begin{aligned}
&\mathcal{C}(\boldsymbol{p}', \boldsymbol{q}|x_4', y_4, x_4)^{\alpha'\alpha\beta'\beta\gamma'\mu\nu\gamma} = \sum_{\omega\in\Omega} \frac{\sigma(\omega)}{N_{\text{sto}}} \sum_{i=1}^{N_{\text{sto}}} \epsilon_{a'b'c'}\epsilon_{abc} \Bigg\{ \\
&\left[\sum_{\boldsymbol{x'}} G_{\omega(A)}\left(x_4', \boldsymbol{x'} \mid x_4, \boldsymbol{x}\right)^{\omega(\alpha')\omega(\alpha)}_{a'a} G_{\omega(B)}\left(x_4', \boldsymbol{x'} \mid x_4, \boldsymbol{x}\right)^{\omega(\beta')\omega(\beta)}_{b'b} \eta_i\left(x_4', \boldsymbol{x'}\right)^{\rho'}_{c'} \left(\gamma_5\right)^{\rho'\omega(\gamma')} \mathrm{e}^{-\mathrm{i}\boldsymbol{p}'(\boldsymbol{x'}-\boldsymbol{x})} \right] \\
&\left[\sum_{\boldsymbol{y}} \left(\gamma_5\right)^{\mu\rho} s^*_{D,i}\left(y_4, \boldsymbol{y}\right)^{\rho}_{d} G_E\left(y_4, \boldsymbol{y} \mid x_4, \boldsymbol{x}\right)^{\nu\omega(\gamma)}_{dc} \mathrm{e}^{+\mathrm{i}\boldsymbol{q}\cdot(\boldsymbol{y}-\boldsymbol{x})} \right] \Bigg\} \,,
\end{aligned} \tag{3.41}$$

with the overall sign function $\sigma(\omega)$.

3.9 Spectator and insertion

Previously we derived a closed expression for all connected baryon three-point functions. The right hand side of this equation can be split into two parts, depending on $(x_4', \boldsymbol{x'})$, $(y_4, \boldsymbol{y})$ respectively. We call the part dependent on $(x_4', \boldsymbol{x'})$ the "spectator"

$$\begin{aligned}
&S_{AB}(\boldsymbol{p}', x_4', x_4)^{\alpha'\alpha\beta'\beta\gamma'}_{ic} \equiv \\
&\sum_{\boldsymbol{x'}} \epsilon_{a'b'c'}\, \epsilon_{abc}\, G_A\left(x_4', \boldsymbol{x'} \mid x_4, \boldsymbol{x}\right)^{\alpha'\alpha}_{a'a} G_B\left(x_4', \boldsymbol{x'} \mid x_4, \boldsymbol{x}\right)^{\beta'\beta}_{b'b} \eta_i\left(x_4', \boldsymbol{x'}\right)^{\rho'}_{c'} \left(\gamma_5\right)^{\rho'\,\gamma'} \mathrm{e}^{-\mathrm{i}\boldsymbol{p}'(\boldsymbol{x'}-\boldsymbol{x})} \,.
\end{aligned} \tag{3.42}$$

The second part, called "insertion", depends only on $(y_4, \boldsymbol{y})$

$$I_{DE}(\boldsymbol{q}, y_4, x_4)^{\mu\nu\gamma}_{ic} \equiv \sum_{\boldsymbol{y}} \left(\gamma_5\right)^{\mu\rho} s^*_{D,i}\left(y_4, \boldsymbol{y}\right)^{\rho}_{d} G_E\left(y_4, \boldsymbol{y} \mid x_4, \boldsymbol{x}\right)^{\nu\gamma}_{dc} \mathrm{e}^{+\mathrm{i}\boldsymbol{q}\cdot(\boldsymbol{y}-\boldsymbol{x})} \,. \tag{3.43}$$

Spectator and insertion can be measured on the lattice and used afterwards to construct the stochastic correlation tensor (SCT)

$$T(\boldsymbol{p}', \boldsymbol{q}, x_4', y_4, x_4)^{\alpha'\alpha\beta'\beta\gamma'\mu\nu\gamma}_{ABDE} = \frac{1}{N_{\text{sto}}} \sum_{i=1}^{N_{\text{sto}}} \left(S_{AB}(\boldsymbol{p}', x_4', x_4)^{\alpha'\alpha\beta'\beta\gamma'}_{ic} \times I_{DE}(\boldsymbol{q}, y_4, x_4)^{\mu\nu\gamma}_{ic} \right) \,. \tag{3.44}$$

This object is the building block of all connected baryon three-point functions because one can use it to construct any baryon three-point function with open spin indices

$$\mathcal{C}(\boldsymbol{p}', \boldsymbol{q}|x_4', y_4, x_4)^{\alpha'\alpha\beta'\beta\gamma'\mu\nu\gamma} = \sum_{\omega\in\Omega} \sigma(\omega) T(\boldsymbol{p}', \boldsymbol{q}, x_4', y_4, x_4)^{\omega(\alpha')\omega(\alpha)\omega(\beta')\omega(\beta)\omega(\gamma')\mu\nu\omega(\gamma)}_{\omega(A)\omega(B)DE} . \quad (3.45)$$

Finally, one can compute a specific baryon three-point function

$$C(\boldsymbol{p}', \boldsymbol{q} \,|\, x_4', y_4, x_4) \equiv \mathcal{P}^{\tau\tau'} \, \mathcal{S}^{\tau'\alpha'\beta'\gamma'\mu\nu\gamma\beta\alpha\tau} \, \mathcal{C}(\boldsymbol{p}', \boldsymbol{q}|x_4', y_4, x_4)^{\alpha'\alpha\beta'\beta\gamma'\mu\nu\gamma} \quad (3.46)$$

by contracting Eq. (3.45) with a user defined projector $\mathcal{P}$ and spin tensor $\mathcal{S}$.

3.10 Lattice setup for spectator and insertion

For the discussion in this section we provide a diagrammatic (c.f. Fig. 3.1) representation of the SCT which is composed of spectator and insertion. All three point-to-all propagators are constructed according to Eq. (1.69). To that end, a single source, with randomly chosen spatial components and temporal position x_4, is used. The stochastic timeslice-to-all propagator is constructed from noise and solution vectors. Noise vectors are seeded on the sink timeslice x_4' and the solution vectors are computed according to Eq. (3.32).

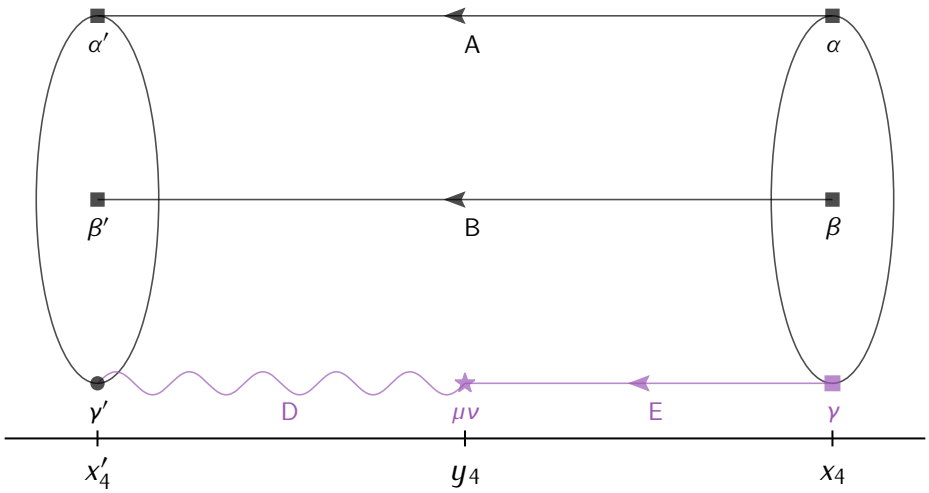

Figure 3.1: Diagrammatic representation of the SCT (c.f. Eq. (3.44)). The Euclidean time flows from right to left. The creation and annihilation interplators are depicted as ellipses, according to Eqs. (3.2 3.1), respectively. Lines with arrows represent point-to-all propagators with generic flavors indices A,B, D and E. Squares are used, to indicate indices, associated with point-to-all propagators. The index, corresponding to the noise vector, is depicted as circle and the operator insertion timeslice y_4 is shown as star. A wiggly line is used to represent the stochastic timeslice-to-all propagator.

We remark, that the Euclidean times, x_4' and x_4, are fixed. However, the operator insertion timeslice y_4, shown Fig. 3.1 can take any value in the interval $x_4' > y_4 > x_4$. This is visualized in Fig. 3.2

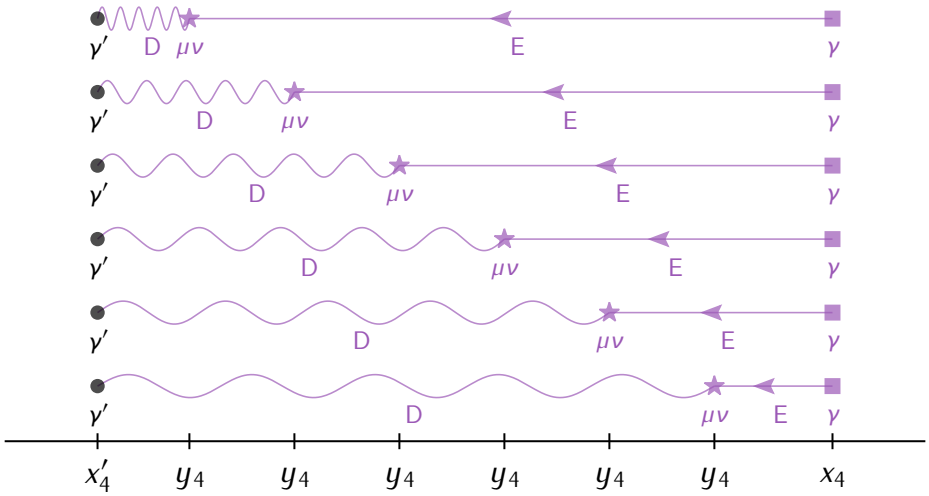

Figure 3.2: Insertion with multiple operator insertion timeslice y_4.

In the following we examine the setup of the generic flavor indices. Therefore, we restrict ourselves to the case of two mass-degenerated light quarks ($l \in \{u, d\}$) and one (heavier) strange quark (s). This assumption leads to the following combinations:

$$\begin{aligned} &\text{case 1}: \quad (A,\, B) = (l, l)\,, \quad &&\text{case 3}: \quad (A,\, B) = (l, s)\,, \\ &\text{case 2}: \quad (A,\, B) = (s, s)\,, \quad &&\text{case 4}: \quad (A,\, B) = (s, l)\,, \end{aligned}$$

for the point-to-all propagators of the spectator. Case 4 can be constructed from case 3. This can be used to reduce the amount of disk space needed for storing the results. At present, this optimization has not been implemented. For the flavor indices of the insertion we obtain the following combinations

$$\begin{aligned} &\text{case 1}: \quad (D,\, E) = (l, l)\,, \quad &&\text{case 3}: \quad (D,\, E) = (l, s)\,, \\ &\text{case 2}: \quad (D,\, E) = (s, s)\,, \quad &&\text{case 4}: \quad (D,\, E) = (s, l)\,. \end{aligned}$$

Cases 3 and 4 can be used for the construction of a flavor changing current. Which flavor combinations one uses for the spectator and the insertion depends on the context of the desired project and needs to be investigated beforehand. Further, it is important to understand, that one has to distinguish between flavor u and d at Wick contraction level (cf. Eq. (3.45)). Only in the data generation stage u and d are not distinguishable. There are, in principle, no restrictions on the spectator momentum $\boldsymbol{p}'$ and the insertion momentum $\boldsymbol{q}$. However, it makes no sense to compute the spectator and the insertion with arbitrary high momenta because we expect that the signal

of the resulting three-point function will become noisy. Further, we know that the continuum dispersion relation will loose its validity for too large momenta. Therefore, we introduce a cut-off at

$$\left(\frac{2\pi}{aN_S}\right) Q_{\text{max}} < 2\,\text{GeV}$$

where N_S is the spatial lattice extent and a the lattice spacing. The restriction for the insertion and spectator momentum is given by

$$\left(\frac{aN_S}{2\pi}\right)^2 \boldsymbol{q}^2 \leq Q^2_{\text{max}}\,, \quad \left(\frac{aN_S}{2\pi}\right)^2 \boldsymbol{p}'^2 \leq P'^2_{\text{max}}\,, \quad P'^2_{\text{max}} \leq \text{floor}\left(\left[\frac{\sqrt{Q^2_{\text{max}}}}{2}+1\right]^2\right)\,,$$

where Q^2_{max} and P'^2_{max} are dimensionless integer numbers. When combining the spectator and the insertion part one should use combinations which satisfy the condition

$$\left(\frac{aN_S}{2\pi}\right)^2 \left(\boldsymbol{q}-\boldsymbol{p}'\right)^2 \leq P'^2_{\text{max}}\,.$$

3.11 Projection operators

So far we have not specified which projection operator $\mathcal{P}$ can be used for the computation of the connected baryon three-point functions defined in Eq. (3.35). In fact, the correct choice of $\mathcal{P}$ depends on the baryon interpolator. For simplicity, we consider the case $\boldsymbol{p}' = \boldsymbol{q} = \boldsymbol{0}$ where we can use

$$\mathcal{P} = \mathcal{P}^{\pm} = \frac{1 \pm \gamma_4}{2}\,, \tag{3.47}$$

to compute matrix elements for unpolarized octet baryons ($\Gamma_1 = 1$ and $\Gamma_2 = C\gamma_5$). The projector defined in Eq. (3.47) obeys the usual properties

$$\mathcal{P}^{\pm}\mathcal{P}^{\pm} = \mathcal{P}^{\pm}\,, \quad \mathcal{P}^{\pm}\mathcal{P}^{\mp} = 0\,, \quad \mathcal{P}^{+} + \mathcal{P}^{-} = 1$$

and projects to positive or negative parity respectively. For polarized octet baryons the situation is different. Typically one is interested in polarization asymmetries with respect to the spin quantization axis k. In this case, one can use the combined projector

$$\mathcal{P}^{\pm}_{k\updownarrow} = \frac{1}{2}(\pm 1 + \gamma_4)\, i\gamma_k\gamma_5\,. \tag{3.48}$$

This projector, for instance, can be used to obtain the three-point function corresponding to the nucleon tensor charge. The situation for decuplet baryons (spin 3/2) is more elaborate due to mixing with spin 1/2 contributions. In principle one can construct a

decuplet baryon by setting

$$\Gamma_1 = 1\,, \quad \Gamma_2 = \gamma_{k\pm} = \frac{1}{4}\epsilon_{klm}(\gamma_j \mp \gamma_m)\,.$$

The spin 3/2 contribution of the corresponding interpolator can be projected out with

$$\mathcal{P}^{+}_{k\uparrow} = \frac{1}{2}\mathcal{P}^{+}(1 + i\gamma_k\gamma_5)\,, \quad \mathcal{P}^{-}_{k\downarrow} = \frac{1}{2}\mathcal{P}^{-}(1 - i\gamma_k\gamma_5)\,,$$

where $\pm$ denotes the parity projection.

3.12 Chapter summary

Let us highlight the most important points of this chapter. We started our new approach by defining generic baryon creation and annihilation interpolators in Eqs. (3.1, 3.2). The interpolators are defined such that any color singlet local three-quark interpolator can be realized by choosing appropriate values for the three flavor indices A, B, C and two matrices Γ_1, Γ_2. In addition, we defined a generic current interpolator in Eq. (3.7). This interpolator is parametrized by two flavor indices D and E as well as one matrix Γ_3. We used the generic interpolators to define the momentum space three-point correlation function in Eq. (3.35). Subsequently, we derived an expression, defined in Eq. (3.41), which is valid for all connected baryon three-point functions. Using a stochastic timeslice-to-all propagator we factorized this expression into two parts, the spectator and the insertion. In the following we demonstrated, that we are able to compute any connected baryon three-point function, after the measurement of the spectator and the insertion. This is possible because our new approach allows us to compute the Wick contraction in a second analysis stage. This, however, requires the contraction of the SCT with user defined matrices specified by the ω-functions.

4

Improved stochastic three-point functions

In the previous chapter we demonstrated the main ideas of our new approach to compute three-point functions. This chapter sets the focus on improvements implemented for production runs. We demonstrate our forward-backward averaging strategy to reduce the statistical errors. Furthermore, we explain in more detail how we obtain three-point functions with multiple source sink distances at once and explain briefly how a stochastic measurement works, including the necessary XML file. This is supplemented by a brief discussion of our smearing approach. Furthermore, we demonstrate, how we incorporate a covariant derivative into the stochastic three-point function measurement. Subsequently, we briefly introduce the meson spectator. It can be used in combination with the insertion to compute meson three-point functions as well. We conclude this chapter with performance measurements and plots which compare stochastic three-point functions to three-point functions obtained from the fixed sink sequential source method. Finally, we summarize all important equations.

4.1 SCT with forward and backward contributions

On top of the gauge noise, present in all lattice QCD calculations, we are facing additional noise due to the stochastically estimated propagator. Our strategy to reduce it is to use a variation of the SCT which incorporates the forward and backward contributions of the point-to-all propagators. To achieve this, we mirror the SCT with respect to the source position axis, as shown in Fig. 4.1.

To indicate the forward and backward position we label the sink positions with a superscript f/b

$$x'^{f} = \left(x_4'^{f},\, \boldsymbol{x}'^{f}\right) , \quad x'^{b} = \left(x_4'^{b},\, \boldsymbol{x}'^{b}\right) , \quad \text{with} \quad x_4'^{f} > x_4'^{b} .$$

Let us remark, that no additional point-to-all propagators are needed for the backward case. The propagators, used for the forward case, already contain backward contributions $x_4'^{b} \leftarrow x_4$. However, one must compute two sets of noise and solution vectors, sourced at x'^{f} and x'^{b} respectively. The sets of noise vectors are constructed according to

$$\eta_i^f(x_4, \boldsymbol{x})_a^\alpha \equiv \begin{cases} \mathbb{Z}_2 \times \mathrm{i}\mathbb{Z}_2 & , \text{ if } x_4 = x_4'^{f} \\ 0 & , \text{ otherwise} . \end{cases} \quad \eta_i^b(x_4, \boldsymbol{x})_a^\alpha \equiv \begin{cases} \mathbb{Z}_2 \times \mathrm{i}\mathbb{Z}_2 & , \text{ if } x_4 = x_4'^{b} \\ 0 & , \text{ otherwise} . \end{cases} \tag{4.1}$$

This type of noise seeding is referred as "single seeding". Compared to the forward only case we need to compute additional backward solution vectors (s_i^b). This leads to a considerable extra effort. To get rid of the introduced overhead, we extended our production code by a seeding method which is referred to as "double seeding". Instead of constructing two sets, according to Eq. (4.1), we construct only one set of noise vectors

$$\eta_i(x_4, \boldsymbol{x})_a^\alpha \equiv \begin{cases} \mathbb{Z}_2 \times \mathrm{i}\mathbb{Z}_2 & , \text{ if } x_4 = x_4'^{f} \text{ or } x_4 = x_4'^{b} \\ 0 & , \text{ otherwise} . \end{cases} \tag{4.2}$$

These noise vectors are simultaneously seeded on the forward and backward sink timeslice, hence the name "double seeding". The conditions under which this type of seeding is justified is discussed in the next section. Regardless of the actual seeding type, we construct the stochastic timeslice-to-all propagator with forward and backward direction according to

$$G_D(x_4'^{f/b}, \boldsymbol{x}'^{f/b} | y_4^{f/b}, \boldsymbol{y}^{f/b})_{c'd}^{\gamma'\mu} = \frac{1}{N_{\mathrm{sto}}} \sum_{i=1}^{N_{\mathrm{sto}}} \eta_i(x_4'^{f/b}, \boldsymbol{x}'^{f/b})_{c'}^{\rho'} \cdot (\gamma_5)^{\rho'\gamma'} \cdot (\gamma_5)^{\mu\rho} \cdot s_{D,i}^*(y_4^{f/b}, \boldsymbol{y}^{f/b})_d^\rho . \tag{4.3}$$

The solution vectors are obtained according to Eq. (3.32) and the factorization of the stochastic three-point function into the spectator and the insertion parts is not affected[1]. We obtain for the spectator with forward and backward noise

$$S_{AB}(\boldsymbol{p}', x_4'^{f/b}, x_4)_{ic}^{\alpha'\alpha\beta'\beta\gamma'} \equiv \epsilon_{a'b'c'}\, \epsilon_{abc} \sum_{\boldsymbol{x}'} \mathrm{e}^{-\mathrm{i}\boldsymbol{p}'(\boldsymbol{x}'-\boldsymbol{x})}$$
$$\times \left(G_A\left(x_4'^{f/b}, \boldsymbol{x}' \mid x_4, \boldsymbol{x}\right)_{a'a}^{\alpha'\alpha} \cdot G_B\left(x_4'^{f/b}, \boldsymbol{x}' \mid x_4, \boldsymbol{x}\right)_{b'b}^{\beta'\beta} \cdot \eta_i\left(x_4'^{f/b}, \boldsymbol{x}'\right)_{c'}^{\rho'} \cdot \left(\gamma_5\right)^{\rho'\gamma'} \right) , \tag{4.4}$$

[1]The Γ matrices are different for the backward case. This is discussed later in more detail.

and the insertion with forward and backward insertions $y_4^{f/b}$

$$I_{DE}(\boldsymbol{q}, y_4^{f/b}, x_4)_{ic}^{\mu\nu\gamma} \equiv \sum_{\boldsymbol{y}} \left(\gamma_5\right)^{\mu\rho} \cdot s_{D,i}^{*}\left(y_4, \boldsymbol{y}\right)_{d}^{\rho} \cdot G_E\left(y_4'^{f/b}, \boldsymbol{y} \mid x_4, \boldsymbol{x}\right)_{dc}^{\nu\gamma} \cdot \mathrm{e}^{+\mathrm{i}\boldsymbol{q}\cdot(\boldsymbol{y}-\boldsymbol{x})} \,. \quad (4.5)$$

The stochastic correlation tensor with forward and backward contributions, shown in Fig. 4.1, is obtained as follows

$$\begin{aligned} &T(\boldsymbol{p}', \boldsymbol{q}, x_4'^{f/b}, y_4^{f/b}, x_4)_{ABDE}^{\alpha'\alpha\beta'\beta\gamma'\mu\nu\gamma} = \\ &\frac{1}{N_{\text{sto}}} \sum_{i=1}^{N_{\text{sto}}} \left(S_{AB}\left(\boldsymbol{p}', x_4'^{f/b}, x_4\right)_{ic}^{\alpha'\alpha\beta'\beta\gamma'} \times I_{DE}\left(\boldsymbol{q}, y_4^{f/b}, x_4\right)_{ic}^{\mu\nu\gamma} \right) \,. \end{aligned} \quad (4.6)$$

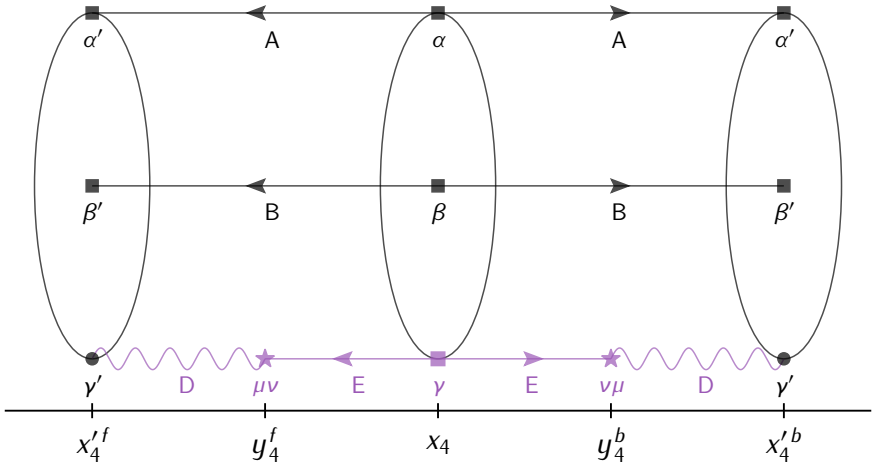

Figure 4.1: SCT with forward ($x_4'^{f}$) and backward ($x_4'^{b}$) sink timeslices. The part shown on the right is new and extents the forward only SCT which is depicted in Fig. 3.1. The presence of forward and backward sinks gives rise to a distinction between forward (y_4^{f}) and backward (y_4^{b}) operator insertion timeslices.

4.1.1 Double seeding remarks

The double seeding approach is extremely beneficial in terms of the computational cost. It reduces the number of solution vector inversions, which is a significant contribution to the overall production cost, by a factor of 1/2. However, one has to keep in mind that this approach is only valid as long as

$$x_4'^{f} - x_4 \qquad \text{and} \qquad x_4 - x_4'^{b}$$

are chosen large enough. The origin of the problem is sketched in Fig. 4.2. To figure out whether the double seeding approach is justified one can perform a test measurement. For instance, one can compare double seeded stochastic three-point functions to three-point functions computed with the sequential source method. Alternatively

one can directly compare three-point functions obtained from single and double seeding. So far we have not seen any significant effects caused by the double seeded. Our production code is capable to use both methods.

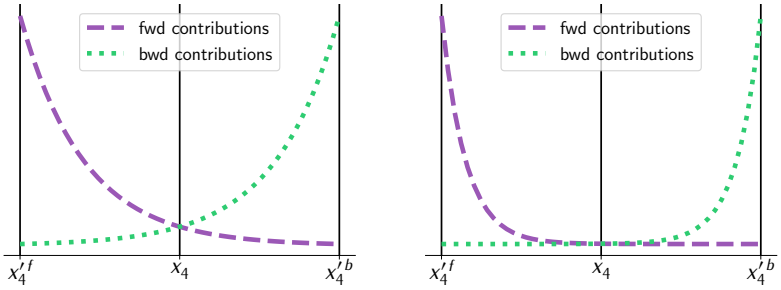

Figure 4.2: The left panel shows a bad setup. The source-sink separations is not large enough. Forward and backward contributions do overlap at the source position x_4. The right panel shows a good setup. Source and sinks are chosen such that no visible overlap occurs at x_4 .

4.2 Forward-backward averaged three-point functions

Previously, we demonstrated the construction of the SCT with forward and backward contributions. In this section we focus on the second step of our two-step approach, namely, the construction of forward and backward three-point functions. Therefore, we assume that the specatator and the insertion have been measured on the lattice.

The construction of forward and backward three-point functions is surprisingly simple because only the spin matrices must be adjusted according to our discussion in section 3.3. With that in mind we define a forward and a backward spin tensor

$$\begin{aligned}
\mathcal{S}_f^{\tau'\alpha'\beta'\gamma'\mu\nu\gamma\beta\alpha\tau} &= (\Gamma_1)^{\tau'\alpha'}\,(\Gamma_2)^{\beta'\gamma'}\,(\Gamma_3)^{\mu\nu}\,(\overline{\Gamma}_2)^{\gamma\beta}\,(\overline{\Gamma}_1)^{\alpha\tau}\,,\\
\mathcal{S}_b^{\tau'\alpha'\beta'\gamma'\mu\nu\gamma\beta\alpha\tau} &= (\Gamma_1\gamma_4\gamma_5)^{\tau'\alpha'}\,(\gamma_5\gamma_4\Gamma_2\gamma_4\gamma_5)^{\beta'\gamma'}\,(\gamma_5\gamma_4\Gamma_3\gamma_4\gamma_5)^{\mu\nu}\,(\gamma_5\gamma_4\overline{\Gamma}_2\gamma_4\gamma_5)^{\gamma\beta}\,(\gamma_5\gamma_4\overline{\Gamma}_1)^{\alpha\tau}\,.
\end{aligned}$$

Forward and backward three-point correlation functions are constructed according to

$$\begin{aligned}
C(\boldsymbol{p}', \boldsymbol{q} \mid x_4'^{f/b}, y_4^{f/b}, x_4) = \mathcal{P}^{\tau\tau'}\,\mathcal{S}_{f/b}^{\tau'\alpha'\beta'\gamma'\mu\nu\gamma\beta\alpha\tau}\\
\times \sum_{\omega\in\Omega}\sigma(\omega)\left\langle T(\boldsymbol{p}', \boldsymbol{q}, x_4'^{f/b}, y_4^{f/b}, x_4)^{\omega(\alpha')\omega(\alpha)\omega(\beta')\omega(\beta)\omega(\gamma')\mu\nu\omega(\gamma)}_{\omega(A)\omega(B)DE}\right\rangle .
\end{aligned} \tag{4.7}$$

We remark that the ω-functions are the same for forward and backward direction. In practice one can use Eq. (4.7) to construct a forward and a backward Bootstrap ensemble for a particular three-point function. The resulting Bootstrap ensembles can be used for averaging.

4.3 SCT with multiple baryon source positions

Until now, we restricted ourselves to a single source position x, symmetrically placed between forward and backward sink (cf. Fig. 4.1). This yields, by construction, the same number of operator insertions $y_4^{f/b}$ which is important for forward-backward averaging. In the following, we describe, how we extent our framework to compute the SCT with multiple source positions $x^{\{s\}}$. For simplicity, let us consider a SCT with two sources ($s = 2$) which are asymmetrically positioned as demonstrated in Fig. 4.3. This setup leads to two distinct source-sink separations. Note that the operator insertion time-slices y_4^f, in Fig. 4.3a, is the average partner of y_4^b, plotted in Fig. 4.3b and y_4^b, in Fig. 4.3a, is the average partner of y_4^f in Fig. 4.3b. Our production code allows an arbitrary number of source positions, but, it is up to the user to define a meaningful setup. To that end, we provide a condition which yields a valid forward-backward averaging setup. We therefore label the temporal source positions

$$x_4'^f > x_4^{\{1\}} > x_4^{\{2\}} > \ldots > x_4^{\{s-1\}} > x_4^{\{s\}} > x_4'^b \,, \tag{4.8}$$

where s is an even number. To construct pairs of source positions, suitable for forward-backward averaging, the following conditions must hold

$$\begin{aligned}
&\text{Source pair 1} \quad : \quad x_4'^f - x_4^{\{1\}} \overset{!}{=} x_4^{\{s\}} - x_4'^b \,, \\
&\text{Source pair 2} \quad : \quad x_4'^f - x_4^{\{2\}} \overset{!}{=} x_4^{\{s-1\}} - x_4'^b \,, \\
&\quad \vdots \\
&\text{Source pair s/2} \quad : \quad x_4'^f - x_4^{\{s/2\}} \overset{!}{=} x_4^{\{s/2+1\}} - x_4'^b \,.
\end{aligned}$$

Spectator and insertion with multiple source positions are given by

$$\begin{aligned}
&S_{AB}(\boldsymbol{p}', x_4'^{f/b}, x_4^{\{s\}})_{ic}^{\alpha'\alpha\beta'\omega\beta\gamma'} \equiv \epsilon_{a'b'c'}\,\epsilon_{abc} \sum_{\boldsymbol{x}'} \mathrm{e}^{-\mathrm{i}\boldsymbol{p}'(\boldsymbol{x}'-\boldsymbol{x}^{\{s\}})} \\
&\times \left(G_A\big(x_4'^{f/b}, \boldsymbol{x}' \,\big|\, x_4^{\{s\}}, \boldsymbol{x}^{\{s\}}\big)_{a'a}^{\alpha'\alpha} \cdot G_B\big(x_4'^{f/b}, \boldsymbol{x}' \,\big|\, x_4^{\{s\}}, \boldsymbol{x}^{\{s\}}\big)_{b'b}^{\beta'\beta} \cdot \eta_i\big(x_4'^{f/b}, \boldsymbol{x}'\big)_{c'}^{\rho'} \cdot \big(\gamma_5\big)^{\rho'\gamma'} \right) ,
\end{aligned} \tag{4.9}$$

$$\begin{aligned}
&I_{DE}(\boldsymbol{q}, y_4^{f/b}, x_4^{\{s\}})_{ic}^{\mu\nu\gamma} \equiv \sum_{\boldsymbol{y}} \mathrm{e}^{+\mathrm{i}\boldsymbol{q}\cdot(\boldsymbol{y}-\boldsymbol{x}^{\{s\}})} \\
&\times \left(\big(\gamma_5\big)^{\mu\rho} \cdot s_{D,i}^*\big(y_4, \boldsymbol{y}\big)_d^{\rho} \cdot G_E\big(y_4'^{f/b}, \boldsymbol{y} \,\big|\, x_4^{\{s\}}, \boldsymbol{x}^{\{s\}}\big)_{dc}^{\nu\gamma} \right) .
\end{aligned} \tag{4.10}$$

In order to compute spectator and insertion, as defined in Eq. (4.9) and Eq. (4.10) extra sets of point-to-all propagators are needed. This increases the overall computational

cost, however, we can still use the noise and solution vectors without modification. As we will see later, the construction of solution vectors is the dominant part in terms of generation costs.

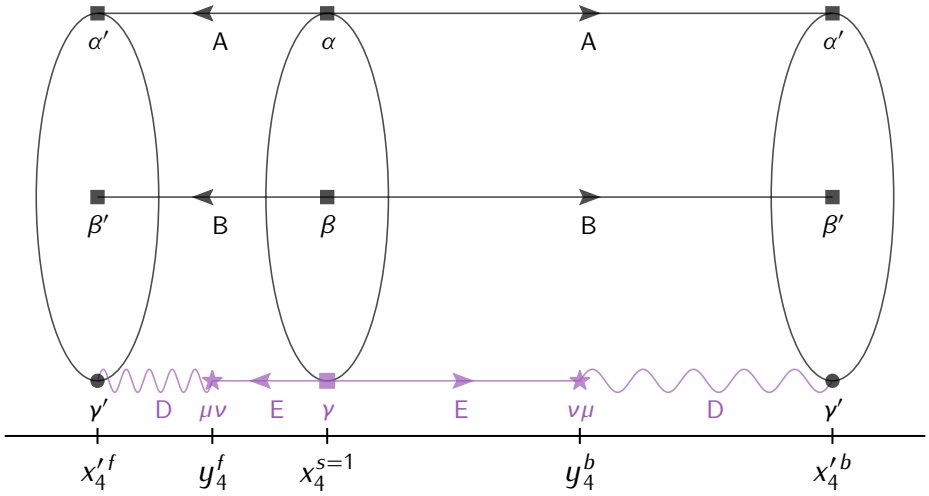

(a) SCT with temporal source at $x_4^{\{1\}}$

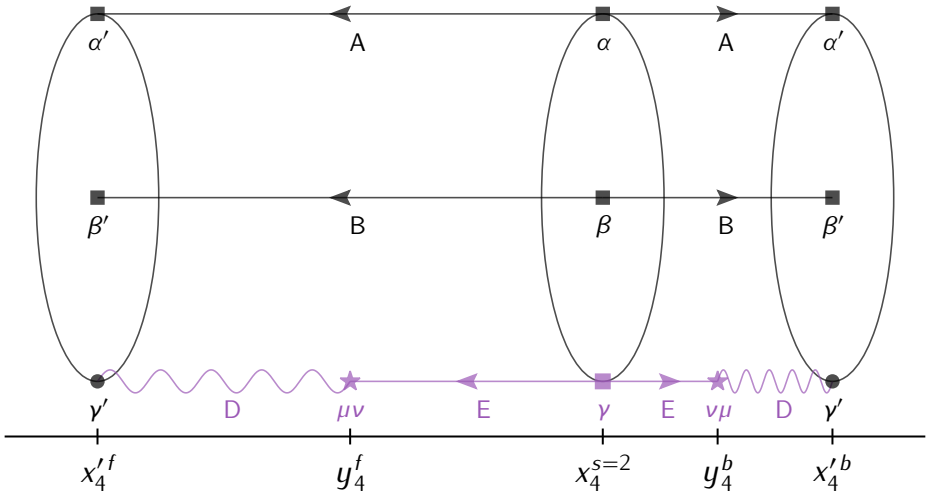

(b) SCT with temporal source at $x_4^{\{2\}}$

Figure 4.3: SCT with two asymmetric temporal source positions $x_4^{\{1\}}$ and $x_4^{\{2\}}$.

4.4 Setup of a stochastic measurement

For the generation of the spectator and the insertion we use a combination of LibHadronAnalysis (LHA) [91] and QDP++/Chroma [92] where Chroma is the main application and LHA is used as a library. The different software components are used as follows. QDP++/Chroma is used to generate the input data for LHA. For instance, it generates the propagators, noise and solution vectors which are needed

to compute the spectator and the insertion (cf. Eq. (4.9) and Eq. (4.10)). At a certain point, they are passed to LHA which performs the actual computation, i.e. it performs the contractions as defined in Eq. (4.9) and Eq. (4.10). Finally, LHA passes the results, i.e. spectator and insertion, back to Chroma which stores them on disc.

To run the stochastic code one must construct a Chroma input XML file. To that end, we developed *chromaxml* [93] which is a fully script-able Python framework to generate Chroma XML input files. The backend for it is the Python module *jinja2* which is a fast, expressive, extensible templating engine. Chromaxml comes with several advantages like missing parameter checks and an object id management system which creates Chroma object ids automatically. What this means will be discussed below. Due to lack of space, we do not provide code which demonstrates the construction of a stochastic three-point function measurement. However, we show a simpler example in Listing 4.4.1, which is sufficient to understand the logic.

Listing 4.4.1: Example code demonstrating the usage of chromaxml to create a inline measurement.

```
1  import chromaxml.generator.inline_measurements as cgen
2
3  root = cgen.InlineMeasurement(
4    cfg_type="WEAK_FIELD", cfg_file="DUMMY",
5    hdf5_file= "myfile.h5", nrow=[24, 24, 24, 48]
6  )
7  source_id = root.add_measurement(
8    cgen.Source(
9      source="POINT_SOURCE", quark_smearing="NO_SMEAR",
10     gauge_id=gauge_id, t_srce=[0, 0, 0, 24]
11   )
12 )
13 prop_id0 = root.add_measurement(
14   cgen.Propagator(
15     fermion_action="UNPRECONDITIONED_CLOVER", inverter="IDFLS_INVERTER",
16     gauge_id=gauge_id, source_id=source_id,
17     Kappa=0.13620, clovCoeff=1.92,
18     FermState="SIMPLE_FERMBC", BlockSize="6 6 6 4",
19     NDflModes=32, KappaDfl=0.13620
20   )
21 )
22 prop_id1 = root.add_measurement(
23   cgen.Propagator(
24     fermion_action="WILSON", inverter="CG_INVERTER",
25     gauge_id=gauge_id, source_id=source_id,
26     Kappa=0.13620, FermState="SIMPLE_FERMBC",
27   )
28 )
29 print(root.render())# Create XML file for your measurment.
```

From line 3 to 6 we setup the root inline measurement. Subsequently, a point source is added to the root measurement. The "add_measurement" function in line 7 returns an object id which can be used for referencing. We use it for the creation of

propagators (line 13 to 28). Using introspection techniques, we are able inform the user if a necessary parameter is missing. This is implemented via an exception. For instance, if "Kappa" in line 17 was not defined by the user. Changing the fermion action and the inverter of a propagator is an easy task, as demonstrated from line 13 to 28.

Currently we are able to generate input files for 27 inline measurement. To implement a new inline measurement one has to provide a corresponding template. We refer the interested reader to the example folder in [93]. The template for the propagator inline measurement is shown in Listing 4.4.2.

Listing 4.4.2: Template for the propagator inline measurement.

```
<elem>
  <Name>PROPAGATOR</Name>
  <Frequency>1</Frequency>
  <Param>
    <version>10</version>
    <quarkSpinType>{{ quarkSpinType }}</quarkSpinType>
    <obsvP>false</obsvP>
    <numRetries>1</numRetries>
    {{ PartialFermionAction }}
    {{ PartialInvertParam }}
  </Param>
  <NamedObject>
    <gauge_id>{{ gauge_id }}</gauge_id>
    <source_id>{{ source_id }}</source_id>
    <prop_id>@@AUTO_ID@@</prop_id>
  </NamedObject>
</elem>
```

We distinguish between to types of templates. The first type is a Chroma inline measurement and the second type is a "partial". A partial can be part of an inline measurement, in other words, it is a sub template. For instance the "PartialInvertParam" in Listing 4.4.2. It is a template by its own and shown in Listing 4.4.3.

Listing 4.4.3: InvertParm is a partial, hence no inline measurement by its own. It is a sub template and appears in other templates.

```
<InvertParam>
    <invType>CG_INVERTER</invType>
    <RsdCG>{{ Residual }}</RsdCG>
    <MaxCG>1000</MaxCG>
</InvertParam>
```

Note that "Residual" in Listing 4.4.3 has a sensible default value. However, in certain cases this value must be changed. It can be overridden in the corresponding inline measurement, in our case in Listing 4.4.2. To allow the user to judge the outcome we supplement each generated XML file with a comment section. The comment section of Listing 4.4.2 is shown in Listing 4.4.4. It provides an compact overview of the measurement and can be used to identify default values.

Listing 4.4.4: Compact summary of the user defined chroma measurement appended at the end of each generated XML file.

```
<!-- Auto generated IDS of your measurement:

MAKE_SOURCE[
SourceSourceType@POINT_SOURCE SmearingParamwvf_kind@NONE using
 {
    'gauge_id': 'default_gauge_field',
    't_srce'  : [0, 0, 0, 24]
  }
]
Hash: acd1df5f546d5cff7425bfa407b3792e594d0ac7

PROPAGATOR[
FermionActionFermAct@UNPRECONDITIONED_CLOVER
InvertParaminvType@IDFLS_INVERTER using
  {
    'BlockSize': '6 6 6 4',
    'FermState': 'SIMPLE_FERMBC',
    'Kappa'    : 0.1362,
    'KappaDfl' : 0.1362,
    'NDflModes': 32,
    'Residual' : 1e-12,
    'clovCoeff': 1.92,
    'gauge_id' : 'default_gauge_field',
    'source_id': 'acd1df5f546d5cff7425bfa407b3792e594d0ac7'
  }
]
Hash: 8e1a9f7b93a125b684a29947e64620c180a9dff0

PROPAGATOR[
FermionActionFermAct@WILSON InvertParaminvType@CG_INVERTER using
 {
   'FermState' : 'SIMPLE_FERMBC',
   'Kappa'     : 0.1362,
   'Residual'  : 1e-12,
   'gauge_id'  : 'default_gauge_field',
   'source_id' : 'acd1df5f546d5cff7425bfa407b3792e594d0ac7'
   }
]
Hash: 91438e6817bb1143337afb1a6670a32230e73c04

-->
```

4.5 Smeared stochastic three-point functions

In this section we explain how we compute smeared stochastic three-point correlation functions. The actual smearing method, used for link and quark smearing is not important here. We start our discussion with the point-to-all propagators which are part of the stochastic correlation tensor shown in Fig. 4.4.

Point-to-all propagators with generic flavor index A and B can be arbitrarily smeared at source and sink. However, it is important[2] that the point-to-all propagator with flavor index E is local at the sink because a smeared propagator would yield a non-local operator. The smearing of the stochastic time-slice-to-all propagator works differently. Acutally there are several possibilities to smear the stochastic propagator, however, so far we have used only the following. In a first step we compute the noise vectors and use them to construct the spectator

$$S_{AB}(\boldsymbol{p}', x_4'^{f/b}, x_4^{\{s\}})_{ic}^{\alpha'\alpha\beta'\omega\beta\gamma'} \equiv \epsilon_{a'b'c'}\,\epsilon_{abc} \sum_{x'} \mathrm{e}^{-\mathrm{i}\boldsymbol{p}'(\boldsymbol{x}'-\boldsymbol{x}^{\{s\}})}$$
$$\times \left(G_A\big(x_4'^{f/b}, \boldsymbol{x}' \mid x_4^{\{s\}}, \boldsymbol{x}^{\{s\}}\big)_{a'a}^{\alpha'\alpha} \cdot G_B\big(x_4'^{f/b}, \boldsymbol{x}' \mid x_4^{\{s\}}, \boldsymbol{x}^{\{s\}}\big)_{b'b}^{\beta'\beta} \cdot \underbrace{\eta_i\big(x_4'^{f/b}, \boldsymbol{x}'\big)_{c'}^{\rho'}}_{\text{unsmeared}} \cdot \big(\gamma_5\big)^{\rho'\gamma'} \right) . \tag{4.11}$$

In a second step we smear the set of noise vectors and perform the inversion as defined in Eq. (3.32). The resulting set of solution vectors is than used to construct the insertion

$$I_{DE}(\boldsymbol{q}, y_4^{f/b}, x_4^{\{s\}})_{ic}^{\mu\nu\gamma} \equiv \sum_{y} \mathrm{e}^{+\mathrm{i}\boldsymbol{q}\cdot(\boldsymbol{y}-\boldsymbol{x}^{\{s\}})}$$
$$\times \left(\big(\gamma_5\big)^{\mu\rho} \cdot \underbrace{S_{D,i}^{*}\big(y_4, \boldsymbol{y}\big)_{d}^{\rho}}_{\text{inverted on smeared noise vectors}} \cdot G_E\big(y_4'^{f/b}, \boldsymbol{y} \mid x_4^{\{s\}}, \boldsymbol{x}^{\{s\}}\big)_{dc}^{\nu\gamma} \right) . \tag{4.12}$$

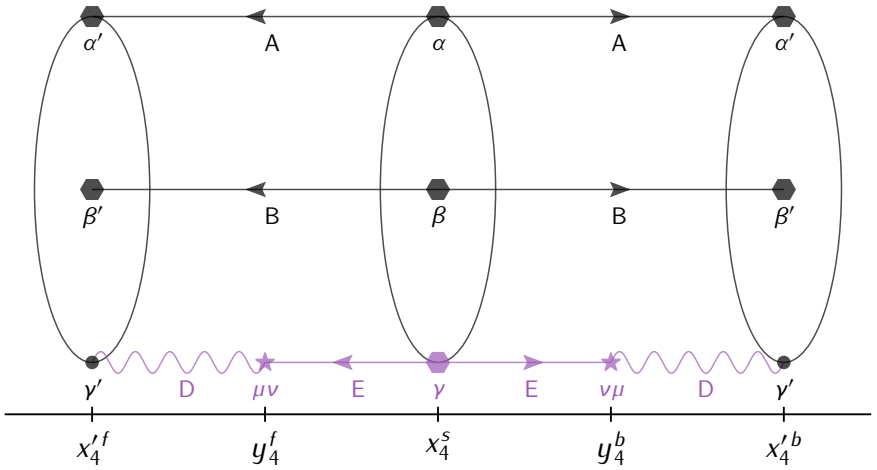

Figure 4.4: Visualization of a smeared stochastic correlation tensor. Smearing iterations, applied to the source and sink of point-to-all propagators are shown as hexagons.

[2]Our production code is not capable to check this condition at runtime.

4.6 Stochastic three-point functions with derivative

The possibility to compute stochastic three-point functions with one covariant derivative is an important improvement. It can be used to obtain matrix elements, needed for the extraction of GFFs on the lattice. In this section, we briefly explain some details how the covariant derivative is incorporated into the stochastic method. We start with the definition of the generic current interpolator

$$\mathcal{J}^{\mu_1}(y_4, \boldsymbol{y})_{DE} \equiv (\Gamma_3)^{\mu\nu} \overline{\Psi}_D(y_4, \boldsymbol{y})^{\mu}_{d} \overleftrightarrow{D}^{\mu_1}_{dc} \Psi_E(y_4, \boldsymbol{y})^{\nu}_{c} \,, \tag{4.13}$$

containing the covariant symmetric derivative

$$\overleftrightarrow{D}^{\mu_1}_{dc} = \frac{1}{2} \left(\overrightarrow{D}^{\mu_1}_{dc} - \overleftarrow{D}^{\mu_1}_{dc} \right) \,, \tag{4.14}$$

which will be replaced by a symmetric discretized version on the lattice. The presence of $\overleftrightarrow{D}^{\mu_1}$ in Eq. (4.13) does not affect the Wick contraction nor the factorization of the three-point function into the spectator and the insertion part. However, one has to introduce[3] an extra minus sign for the backward three-point function with temporal derivative ($\mu_1 = 4$). The spectator part is not affected, but the insertion part must be modified

$$\begin{aligned} I^{\mu_1}_{DE}(\boldsymbol{q}, y_4, x_4)^{\mu\nu\gamma}_{ic} = \frac{1}{2} \sum_{\boldsymbol{y}} \Bigg\{ & \left(\left[\gamma_5 \, s_{D,i}(y_4, \boldsymbol{y}) \right]^{\dagger} \right)^{\mu}_{d} \cdot \left(\overrightarrow{D}_{\mu_1} G_E(y_4, \boldsymbol{y} \mid x_4, \boldsymbol{x}) \right)^{\nu\gamma}_{dc} \\ - & \left(\left[\overrightarrow{D}_{\mu_1} \gamma_5 \, s_{D,i}(y_4, \boldsymbol{y}) \right]^{\dagger} \right)^{\mu}_{d} \cdot \left(G_E(y_4, \boldsymbol{y} \mid x_4, \boldsymbol{x}) \right)^{\nu\gamma}_{dc} \Bigg\} \, \mathrm{e}^{+\mathrm{i}\boldsymbol{q}\cdot(\boldsymbol{y}-\boldsymbol{x})} \,. \end{aligned} \tag{4.15}$$

The computation of the insertion with derivative is more expensive compared to the version without derivative due to

$$\overrightarrow{D}_{\mu_1} \gamma_5 \, s_{D,i}(y_4, \boldsymbol{y}) \quad \text{and} \quad \overrightarrow{D}_{\mu_1} G_E(y_4, \boldsymbol{y} \mid x_4, \boldsymbol{x}) \,. \tag{4.16}$$

4.7 Implementation details of spectator and insertion

The spectator, as well as the insertion is generated by a fork of LibHadronAnalysis [91]. LHA is used as a library and is integrated in the QDP++/Chroma [92] framework. A full introduction into LHA would exceed the scope of this work, however, we discuss

[3] This is automatized in our software stack.

some points. LHA is optimized for the computation of the spectator

$$S_{AB}(\boldsymbol{p}', x_4'^{f/b}, x_4^{\{s\}})_{ic}^{\alpha'\alpha\beta'\omega\beta\gamma'} \equiv \epsilon_{a'b'c'}\,\epsilon_{abc} \sum_{\boldsymbol{x}'} \mathrm{e}^{-\mathrm{i}\boldsymbol{p}'(\boldsymbol{x}'-\boldsymbol{x}^{\{s\}})}$$
$$\times \left(G_A\big(x_4'^{f/b}, \boldsymbol{x}' \mid x_4^{\{s\}}, \boldsymbol{x}^{\{s\}}\big)_{a'a}^{\alpha'\alpha} \cdot G_B\big(x_4'^{f/b}, \boldsymbol{x}' \mid x_4^{\{s\}}, \boldsymbol{x}^{\{s\}}\big)_{b'b}^{\beta'\beta} \cdot \eta_i\big(x_4'^{f/b}, \boldsymbol{x}'\big)_{c'}^{\rho'} \cdot \big(\gamma_5\big)^{\rho'\gamma'} \right)$$

LHA uses the source positions ($x^{\{s\}}$) as well as the forward and backward parts ($x_4'^{f/b}$) of all used components (propagator, noise, etc.) as parallelization index. The maximal number of MPI ranks which compute the spectator in parallel is thus $2 \times N_{\mathrm{src}}$. For example, the spectators shown in Fig. 4.3 with source positions $x_4^{\{1\}}$ and $x_4^{\{1\}}$ are computed simultaneously. This is achieved by an input data (e.g. phases, propagators and noise vectors) redistributes among the availably MPI ranks. During this redistribution LHA converts the data to a SIMD friendly layout and changes the loop order compared to QDP++/Chroma where only relevant parts from the Chroma owned memory are copied. Let us now come to the insertion without covariant derivative

$$I_{DE}\big(\boldsymbol{q}, y_4^{f/b}, x_4^{\{s\}}\big)_{ic}^{\mu\nu\gamma} = \sum_{\boldsymbol{y}} \gamma_5^{\mu\rho} \cdot s_{D,i}^{*}\big(y_4^{f/b}, \boldsymbol{y}\big)_{d}^{\rho} \cdot G_E\big(y_4^{f/b}, \boldsymbol{y} \mid x_4^{\{s\}}, \boldsymbol{x}^{\{s\}}\big)_{dc}^{\nu\gamma} \cdot \mathrm{e}^{+\mathrm{i}\boldsymbol{q}\cdot(\boldsymbol{y}-\boldsymbol{x}^{\{s\}})}\,.$$

LHA performs the computation of the insertion in parallel. It uses, for a given source position ($x^{\{s'\}}$), the operator insertion ($y^{f/b}$) as parallelization index. For instance, the insertion parts ($y^{f/b}$) shown in Fig. 4.3a are computed simultaneously. The redistribution of the input data (propagators, solution vectors, etc.), from Chroma to LHA is done such that each MPI rank has approximately the same number of tasks to work with. Insertions with covariant derivatives are treated the same way. However, an extra loop, in the corresponding Chroma inline measurement is needed for the derivative directions μ_1. Due to the symmetrization in Eq. (4.15), one can expect that LHA needs twice the time compared to the case where no derivative occurs. This factor, however, is not significant. The production of the necessary input data, for instance Eq. (4.16), are the dominant time consuming parts. More details about the performance of are presented in section 4.9.

4.8 Stochastic three-point functions for mesons

In this section we briefly highlight that the insertion part is constructed such that one can (re-)use it for the computation of meson-three-point correlation functions. We implement the meson spectator as follows

$$S_A\left(\boldsymbol{p}', x_4'^{f/b}, x_4^{\{s\}}\right)_{ic}^{\alpha\,\alpha'\,\gamma'} = \sum_{\boldsymbol{x}'} \mathrm{e}^{-\mathrm{i}\boldsymbol{p}'\cdot(\boldsymbol{x}'-\boldsymbol{x}^{\{s\}})} \times \left(\gamma_5 \cdot G_A^\dagger\left(x_4'^{f/b}, \boldsymbol{x}' \mid x^{\{s\}}, \boldsymbol{x}^{\{s\}}\right) \cdot \gamma_5\right)_{ca'}^{\alpha\,\alpha'} \cdot \eta_i\left(x_4'^{f/b}, \boldsymbol{x}'\right)_{a'}^{\rho'} \cdot \left(\gamma_5\right)^{\rho'\gamma'} . \tag{4.17}$$

Compared to the baryon spectator it has one propagator less (we have 6 fields hence 3 propagators in total). We further exploit γ_5-hermiticity in Eq. (4.17) to changed the propagation direction of the point-to-all propagator. This is necessary since meson three-point functions have closed loops. The SCT for the meson is given by and visualized in Fig. 4.5.

$$T^{\mu_1}(\boldsymbol{p}', \boldsymbol{q}, x_4'^{f/b}, y_4^{f/b}, x_4^{\{s\}})_{ADE}^{\alpha'\alpha\gamma'\mu\nu\gamma} = \frac{1}{N_{\mathrm{sto}}} \sum_{i=1}^{N_{\mathrm{sto}}} \left(S_A\left(\boldsymbol{p}', x_4'^{f/b}, x_4^{\{s\}}\right)_{ic}^{\alpha'\alpha\gamma'} \times I_{DE}^{\mu_1}\left(\boldsymbol{q}, y_4^{f/b}, x_4^{\{s\}}\right)_{ic}^{\mu\nu\gamma} \right) \tag{4.18}$$

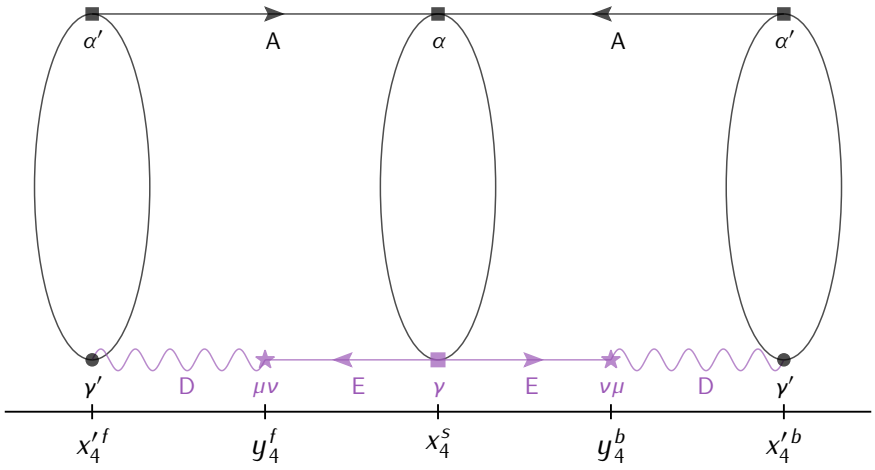

Figure 4.5: Stochastic correlation tensor for mesons.

4.9 Performance

We briefly discuss the performance of the stochastic code which is based on [94]. The measurements were carried out on a single gauge configuration of the CLS ensemble H101 ($32^3 \times 96$, $a \approx 0.086$ fm) which is a $N_f = 2+1$ ensemble with non-perturbatively

$\mathcal{O}(a)$ improved Wilson fermions and tree-level improved Symanzik gauge action using open boundary conditions in time. The pion and kaon mass is about 420 MeV. The benchmarks were performed on the QPACE3 supercomputer of the SFB/TR 55 at the Jülich Supercomputing Centre. The machine is based on Intel Xeon Phi (KNL) processors connected via Intel Omni-Path. The measurement includes the computation of the baryon spectator, meson spectator and the insertion without derivative where we use 50 single-seeded noise vectors in forward as well as 50 single-seeded noise vectors in the backward direction. We use a single source position ($s = 1$) located at $x_4^{\{1\}} = 30\text{a}$ with a source sink distance of $x_4'^f - x_4^{\{1\}} = x_4^{\{1\}} - x_4'^b = 10\text{a}$.

In this test we study two extreme cases given in terms of the computed momenta. In the first scenario, we consider

$$K_{00}: \quad \boldsymbol{k}_{p'}^2 = 0 \quad \text{and} \quad \boldsymbol{k}_q^2 = 0$$

with $\boldsymbol{p}' = 2\pi \boldsymbol{k}_{p'}/L$ and $\boldsymbol{q} = 2\pi \boldsymbol{k}_q/L$ which leads to a single momentum combination. In the second scenario we investigate the case

$$K_{88}: \quad \boldsymbol{k}_{p'}^2 \in \{0 \ldots 8\} \quad \text{and} \quad \boldsymbol{k}_q^2 \in \{0 \ldots 8\}$$

which yields $93 \cdot 93$ possible different momentum combinations. The results are summarized in Fig. 4.6 showing the distribution of spent computer time for the individual steps to obtain the spectators and the insertion.

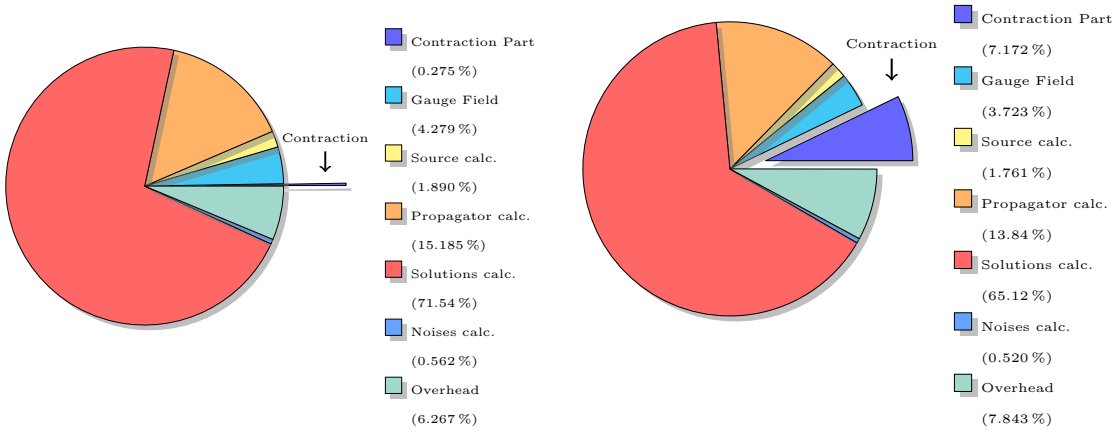

(a) Setup K_{00} (b) Setup K_{88}

Figure 4.6: Distribution of used computer time for the individual steps to obtain the spectators and the insertion. The contraction part refers to the time which is consumed by LHA in order to calculate the spectators and the insertion. Figure taken from [94].

The dominant time-consuming part, for both momentum scenarios, is given by the creation of the solutions vectors. For setup K_{00} the actual computation of the spectators and the insertion (denoted as "Contraction Part") is neglectable. The overall

computation time for setup K_{00} (530 seconds) and Setup K_{88} (575 seconds) is roughly the same. Hence it is possible to produce data for a large number of momenta[4] without increasing the computation time significantly.

This measurement uses a single source position, however, we are able to give the following statement for multiple source-sink separations. An additional source position gives rise to three additional point-to-all propagators and would double the "Propagator calc." time in Fig. 4.6. The time spent in the "Contraction" is expected to be unchanged for baryon and meson spectators due to the parallelization of LHA. For the insertion without derivative we expect a linear increase of the contraction time with the number of source positions. Further, one can expect that the time to compute the insertion with symmetric (factor 2) covariant derivative is roughly eight times longer than without derivative. However, one has to keep in mind that the terms shown in Eq. (4.16) bust be computed beforehand.

Our performance measurement indicates that the overall performance of LHA is best in the case of many momentum combinations and several source-sink distances. Readers who are interested in a direct comparison between the sequential method for meson three-point functions and the stochastic counterpart are refereed to [94] where it is shown that the stochastic code is faster by at least a factor of 1.5 in the high momentum setup Setup K_{88}.

4.10 Disk space requirements of spectator and insertion

In this section we derive expressions which parametrize the necessary disk space to store the spectator and the inerstion parts. We summarized all necessary parameters in Table 4.1. The size of the spectator and the insertion, for a single smearing setup is

$$\text{Size}\left[S_{AB}\left(\boldsymbol{p}', x_4'^{f/b}, x_4^{\{s\}}\right)_{ic}^{\alpha'\alpha\beta'\beta\gamma'}\right] = \frac{N_F^{\text{spe}} \times N_{\boldsymbol{p}'} \times N_{\text{snk}} \times N_{\text{src}} \times N_{\text{sto}} \times N_{\text{c}} \times N_{\text{s}}^5 \times 16}{10^9}\,\text{GB}\,, \tag{4.19}$$

$$\text{Size}\left[I_{DE}^{\mu_1}\left(\boldsymbol{q}, y_4^{f/b}, x_4^{\{s\}}\right)_{ic}^{\mu\nu\gamma}\right] = \frac{N_{\mu_1} \times N_F^{\text{ins}} \times N_{\boldsymbol{q}} \times (x_4'^f/a - x_4'^b/a - 2) \cdot N_{\text{src}} \times N_{\text{sto}} \times N_{\text{c}} \times N_{\text{s}}^3 \times 16}{10^9}\,\text{GB}\,. \tag{4.20}$$

Assuming the maximum values in Table (4.1), we find, that 4.5 GB and 68.6 GB per gauge configurations are needed to store the spectator and the insertion respectively. For the insertion we assumed $N_{\mu_1} = 5$ and set $(x_4'^f/a - x_4'^b/a - 2) = 30$. This

[4] This increase the disk space consumption.

shows, that depending on the actual setup, the required disk space is relatively large compared to traditional methods.

Symbol	(Typical) value	Number of	Section
N_s	4	spin indices	-
N_c	3	color indices	-
N_sto	$50 - 100$	stochastic estimators	3.6
$N_{\boldsymbol{p}'}$	$1 - 57$	spectator momenta	3.10
$N_{\boldsymbol{q}}$	$1 - 93$	insertion momenta	3.10
N_F^spe	$1 - 4$	spectator flavor combinations	3.10
N_F^ins	$1 - 4$	insertion flavor combinations	3.10
N_src	$1 - 4$	source positions $x_4^{\{s\}}$	4.3
N_snk	2	sink positions $x_4'^{f/b}$	4.3
$N_{y_4^{f/b}}$	$N_\mathrm{src} \cdot (x_4'^f/a - x_4'^b/a - 2)$	$y_4^{f/b}$ insertions times	4.3
N_{μ_1}	4 (+1)	derivative directions (+1 for no derivative)	4.6

Table 4.1: List of parameters and their (typical) values in order to parametrize the disk space of the spectator and the insertion.

4.11 Remarks for stochastic three-point functions

In terms of production runs, it is most beneficial to compute the meson spectator, the baryon spectator and the insertion in a single run. Our code, however, is able to compute each stochastic component (baryon spectator, meson spectator, insertion) separately. This feature can be used to calculate missing flavor combinations, i.e., combinations which were not computed in the initial measurement. In the following we discuss when one should use the stochastic method compared to the sequential method for the generation of three-point functions. This, however, can not be answered generically for all possible applications. For a given project one has to estimate the production cost for both methods in order to come to a decision. For applications which require three-point functions with

- many momentum combinations
- or many flavor combinations
- or many source-sink separations

is highly likely, that the stochastic method performs better than the sequential method.

4.12 Final expressions

In the previous sections we have improved our method to be suitable for state of the art computations of three-point functions. In this section we present the final formulas.

For the insertion as well as for the spectator we do not label the propagators, noise and solution vectors with additional indices describing the smearing types and iterations. However, one has to keep in mind that these might be present. This is important if one attempts to count the disk space/memory consumption.

4.12.1 Stochastic correlation tensor for baryons

The stochastic correlation tensor with all improvements for the baryon is presented below

$$T^{\mu_1}(\boldsymbol{p}', \boldsymbol{q}, x_4'^{f/b}, y_4^{f/b}, x_4^{\{s\}})^{\alpha'\alpha\beta'\beta\gamma'\mu\nu\gamma}_{ABDE} = \frac{1}{N_{\text{sto}}} \sum_{i=1}^{N_{\text{sto}}} \left(S_{AB}\left(\boldsymbol{p}', x_4'^{f/b}, x_4^{\{s\}}\right)^{\alpha'\alpha\beta'\beta\gamma'}_{ic} \times I^{\mu_1}_{DE}\left(\boldsymbol{q}, y_4^{f/b}, x_4^{\{s\}}\right)^{\mu\nu\gamma}_{ic} \right) \tag{4.21}$$

and visualized in Fig. 4.7. When there is no covariant derivative, one can drop the index μ_1.

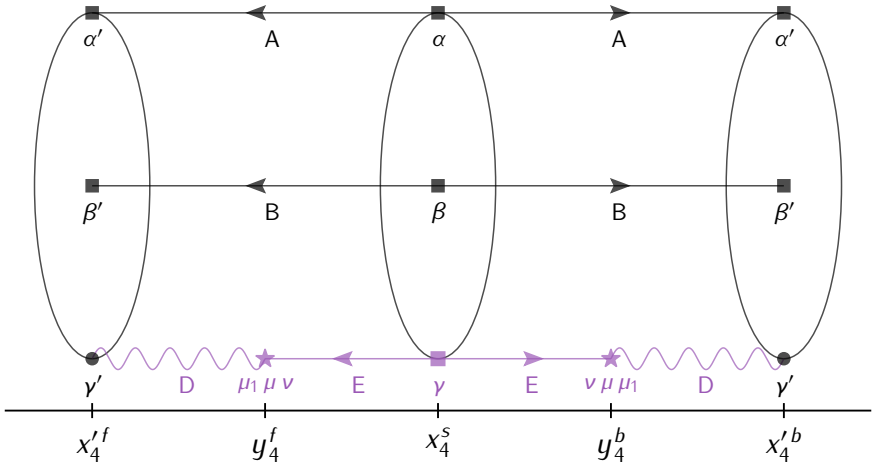

Figure 4.7: Stochastic correlation tensor for baryons.

4.12.2 Baryon three-point function with open indices

Baryon three-point functions with open spin indices are obtained according to

$$\mathcal{C}^{\mu_1}\left(\boldsymbol{p}', \boldsymbol{q}, x_4'^{f/b}, y_4^{f/b}, x_4^{\{s\}}\right)^{\alpha'\alpha\beta'\beta\gamma'\mu\nu\gamma} = \sum_{\omega\in\Omega} \sigma(\omega) \left\langle T^{\mu_1}\left(\boldsymbol{p}', \boldsymbol{q}, x_4'^{f/b}, y_4^{f/b}, x_4^{\{s\}}\right)^{\omega(\alpha')\omega(\alpha)\omega(\beta')\omega(\beta)\omega(\gamma')\mu\nu\omega(\gamma)}_{\omega(A)\omega(B)DE} \right\rangle . \tag{4.22}$$

4.12.3 Baryon three-point function

Our final expression for stochastic baryonic three-point functions is

$$C^{\mu_1}\left(\boldsymbol{p}', \boldsymbol{q}, x_4'^{f/b}, y_4^{f/b}, x_4^{\{s\}}\right) = \mathcal{P}^{\tau\tau'} \cdot \mathcal{S}_{f/b}^{\tau'\alpha'\beta'\gamma'\mu\nu\gamma\beta\alpha\tau} \cdot \mathcal{C}^{\mu_1}\left(\boldsymbol{p}', \boldsymbol{q}, x_4'^{f/b}, y_4^{f/b}, x_4^{\{s\}}\right)^{\alpha'\alpha\beta'\beta\gamma'\mu\nu\gamma} \tag{4.23}$$

For the reader's convenience we provide the definitions

$$\begin{aligned}
\mathcal{S}_f^{\tau'\alpha'\beta'\gamma'\mu\nu\gamma\beta\alpha\tau} &= (\Gamma_1)^{\tau'\alpha'}(\Gamma_2)^{\beta'\gamma'}(\Gamma_3)^{\mu\nu}(\overline{\Gamma}_2)^{\gamma\beta}(\overline{\Gamma}_1)^{\alpha\tau}\,, \\
\mathcal{S}_b^{\tau'\alpha'\beta'\gamma'\mu\nu\gamma\beta\alpha\tau} &= (\Gamma_1\gamma_4\gamma_5)^{\tau'\alpha'}(\gamma_5\gamma_4\Gamma_2\gamma_4\gamma_5)^{\beta'\gamma'}(\gamma_5\gamma_4\Gamma_3\gamma_4\gamma_5)^{\mu\nu}(\gamma_5\gamma_4\overline{\Gamma}_2\gamma_4\gamma_5)^{\gamma\beta}(\gamma_5\gamma_4\overline{\Gamma}_1)^{\alpha\tau}\,,
\end{aligned}$$

where we use $\overline{\Gamma}_1 = \gamma_4\Gamma_1^\dagger\gamma_4$ and $\overline{\Gamma}_2 = \gamma_4\Gamma_2^\dagger\gamma_4$ according to Eqs. (3.5).

4.13 Qualitative comparison

In this section we show a qualitative comparison of stochastic and sequential three-point functions. The comparison is only qualitative because the shown three-point functions are taken from real productions runs where the sources of the sequential three-point functions do not coincided with the forward sources used of the stochastic method. We restrict ourselves to a single source-sink distance and the nucleon with $\overline{u}u$ current measured on 1543 configurations of the $N203$ CLS ensemble. We consider the forward limit, e.g., the two momenta $\boldsymbol{p}$ and $\boldsymbol{q}$ are set to zero. Stochastic three-point functions are constructed from $N_{\text{sto}} = 100$ stochastic estimates and using the double seeding method. The obtained three-point functions, shown in Fig. 4.8 are shifted to the origin and the operator insertion timeslice, plotted on the x-axes, is called τ.

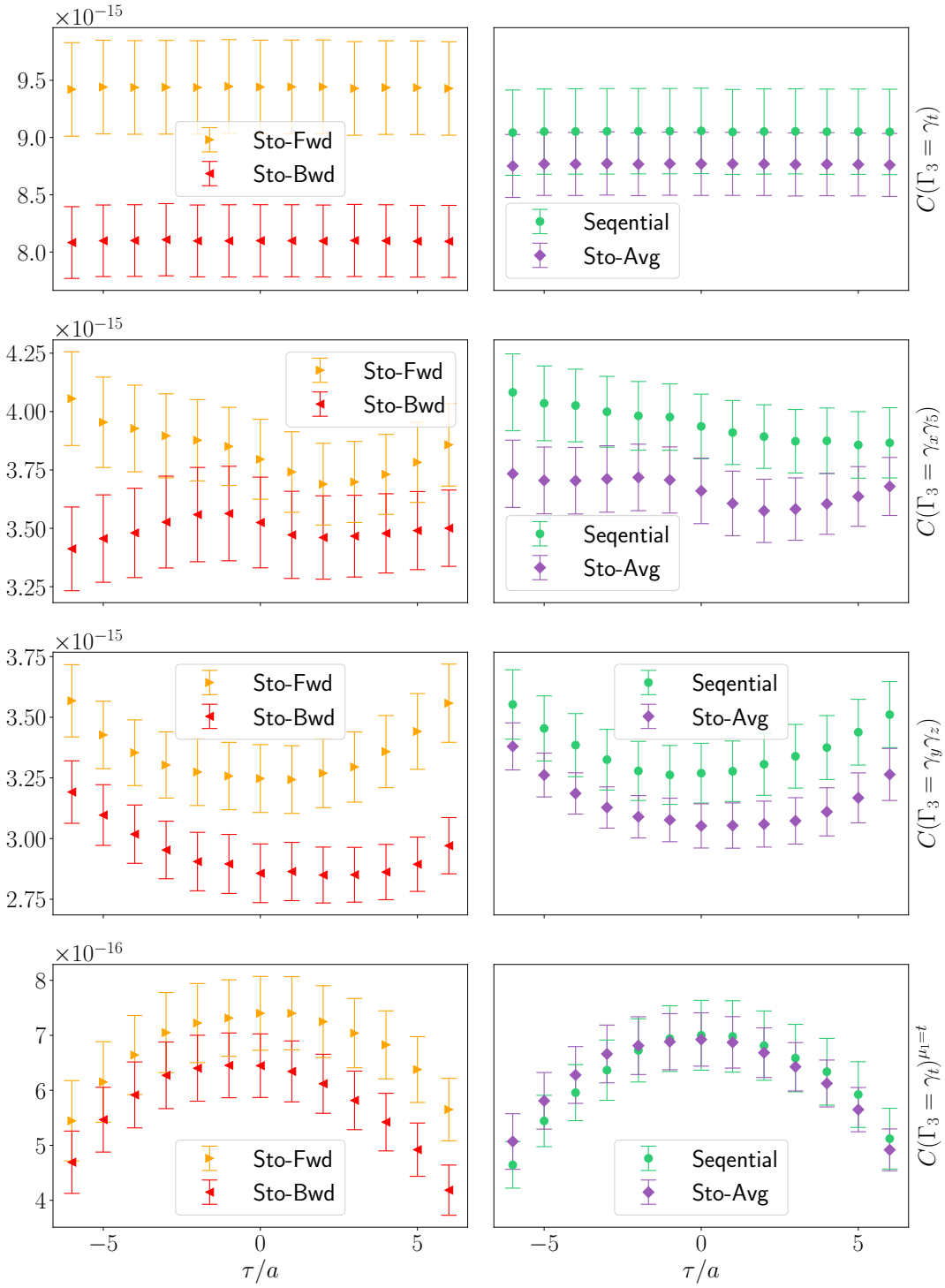

Figure 4.8: Comparison of stochastic and sequential three-point functions. The left panels show the individual forward-backward contributions of the stochastic method and the right panel compares the sequential three-point functions to the forward-backward averaged stochastic three-point functions. From top to bottom we present different currents parametrized by Γ_3. The first three plot show three-point functions which correspond to the vector, axial and tensor current. The bottommost panel shows a three-point function with covariant derivative in temporal direction ($\mu_1 = t$). The polarizations of all three-point functions are suitable chosen.

5

Software and hardware stack for stochastic three-point functions

This chapter provides a small overview of the software and hardware stack which is used to effectively construct stochastic three-point functions. A serious effort was made to make the construction steps[1] as fast and easy as possible which has a decisive impact on the time to publication. This is mandatory because our stochastic approach produces relatively large amounts of data (spectator and insertion) and the correct post processing is non-trivial, in contrast to traditional methods. The produced software stack is written such that daily tasks as fitting three-point functions is achievable with $\mathcal{O}(50)$ lines of Python code. This is indeed a key requirement to profit form stochastic three-point functions because it allows people to produce results within a relatively short time.

5.1 Constructing stochastic three-point functions

This section demonstrates the main steps and concepts to construct a baryon three-point function after the measurement of the spectator and the insertion. We restrict ourself to a proton three-point function and assume that the flavor setup of spectator and the insertion was made properly (cf. section 3.10). Further, we demonstrate only the construction for the forward case. Most of the steps discussed below are automatized such that no manual interaction is necessary. However, we discuss them in great detail to provide the reader the basis to understand our new approach.

[1] The steps after the measurement of spectator and insertions.

Step I: Define the flavors

Define the flavor indices of the generic interpolators defined in Eqs. (3.1, 3.2, 3.7)

$$A = u, \qquad B = u, \qquad C = d, \qquad D = u, \qquad E = u, \tag{5.1}$$

to obtain a proton three-point function with $\bar{u}u$-flavor.

Step II: Calculate the Wick contraction

Compute the Wick contraction for the flavor set-up according to Eq. (5.1). For this task we provide a python package called *openGFF* [95] which is a wrapper around the *wick* package [87]. The necessary steps are shown in Listing 5.1.1. We instantiate the generic baryon interpolators and compute the Wick contraction (line 8-13). For consistency reasons we only allow flavors as input and hide spin, color and space-time positions. The ω-functions are computed in line 13 and the result are presented as comments from line 14 to 16. Subsequently, we calculate the sign correction functions $\sigma(\omega)$ (line 16) and store the flavor indices of the SCT (line 18).

Listing 5.1.1: Calculation of ω, $\sigma(\omega)$ and the flavor indices of the SCT.

```
1  from opengff.interpolators.baryon import BaryonAnnihilator, BaryonCreator
2  from opengff.interpolators.baryon import BaryonCurrent
3  from opengff.interpolators.baryon import BaryonSpinProjection
4  from opengff.stoch3pt.contraction import BaryonContraction
5  from wick.flavors import U, D
6  # Perfom the wick contraction
7  wick_contraction = BaryonContraction(
8    BaryonAnnihilator(U,U,D),
9    BaryonCurrent(U,U),
10   BaryonCreator(D,U,U),
11   BaryonSpinProjection()
12 )
13 omegas = wick_contraction.einsum_strings()
14 # [ 'ab,cd,be,fa,gh,ij,gdhceijf', 'ab,cd,be,fa,gh,ij,gfhceijd',
15 #   'ab,cd,be,fa,gh,ij,edhcgijf', 'ab,cd,be,fa,gh,ij,efhcgijd']
16 signs = wick_contraction.signs() # Calculate $\sigma(\omega)$
17 # [-1, -1, -1, -1]
18 flavors = wick_contraction.propagator_flavors() # SCT flavor structure
19 # ['u', 'd', 'u', 'u']
```

Step III: Define the content of $\mathcal{S}$ and $\mathcal{P}$

Projection to positive parity is done by $\mathcal{P} = \mathcal{P}^+$. To obtain a proton three-point function, corresponding to the vector charge, we define the following Dirac matrices $\Gamma_1 = 1$, $\Gamma_2 = C\gamma_5$, $\Gamma_3 = \gamma_4$, yielding the spin tensor

$$\mathcal{S}^{\tau'\alpha'\beta'\gamma'\mu\nu\gamma\beta\alpha\tau} \to (1)^{\tau'\alpha'} \, (C\gamma_5)^{\beta'\gamma'} \, (\gamma_4)^{\mu\nu} \, (\gamma_4(C\gamma_5)^\dagger\gamma_4)^{\gamma\beta} \, (\gamma_4(1)^\dagger\gamma_4)^{\alpha\tau} \, .$$

Step IV: Create the SCT with spectator and insertion

Define the momenta, for instance $\boldsymbol{p}' = \boldsymbol{q} = \boldsymbol{0}$. Note that the flavor indices of the SCT are already known due to the previous step. Further, define the Euclidean times $x_4'^f$, y_4^f and x_4^f. To that end, assume that the baryon sink is at $x_4'^f = 50a$ and the baryon source position is $x_4 = 35a$. The operator insertion y_4^f can take values according to $x_4'^f > y_4^f > x_4^f$. For simplicity, we consider only $y_4^f = 40a$. Construct the SCT as shown below

$$T(\boldsymbol{0}, \boldsymbol{0}, 50a, 40a, 35a)^{\alpha'\alpha\beta'\beta\gamma'\mu\nu\gamma}_{uduu} = \\ \frac{1}{N_{\text{sto}}} \sum_{i=1}^{N_{\text{sto}}} \left(S_{ud}(\boldsymbol{0}, 50a, 35a)^{\alpha'\alpha\beta'\beta\gamma'}_{ic} \times l_{uu}(\boldsymbol{q}, 40a, 35a)^{\mu\nu\gamma}_{ic} \right) . \tag{5.2}$$

Step V: Contract the SCT

Construct the three-point function by loading the SCT, as defined in Eq. (5.2) and perform the contraction with the spin tensor and the projection operator. The necessary code is shown in Listing 5.1.2 which is meant as a continuation of Listing 5.1.1.

Listing 5.1.2: Construction code to obtain a proton three-point function.

```
# Continuation of previous Listing
from numpy import einsum
from numpy.random import rand
from rioi.reader.stoch3pt.contractions.gamma_mat import Factory

def load_sct(p_prime, q, x_prime, y, x, A, B, D, E):
  x = rand(4,4,4,4,4,4,4,4)
  return x + 1.0j * x

# Create matrices
m1 = Factory.create_from_string("(gi + gt)/2")
m2 = Factory.create_from_string("gi")
m3 = Factory.create_from_string("gy*gt*g5")
m4 = Factory.create_from_string("gt")
m5 = Factory.create_from_string("gt*H(gy*gt*g5)*gt")
m6 = Factory.create_from_string("gt*H(gi)*gt")

# Load data from disc (flavors defined in prev. Listing)
t = load_sct((0,0,0), (0,0,0), 50, 40 ,35, *flavors)

# Perform contractions
result = 0.0 + 0.0j
for sigma, omega in zip(signs, omegas):
    result  += sigma *  einsum(omega, m1, m2, m1, m4, m5, m6, t)
```

Note that the variables "signs", "omegas" and "flavors" are defined in Listing 5.1.1. We do not comment the individual lines of code, however, we like to highlight the great flexibility of our new approach. Listing 5.1.2 is an implementation of

$$
\begin{aligned}
&C(\mathbf{0},\mathbf{0}\,|\,50a,40a,35a) = \\
&\times \Big(\frac{1+\gamma_4}{2}\Big)^{\tau\tau'} (1)^{\tau'\alpha'} \left(C\gamma_5\right)^{\beta'\gamma'} \left(\gamma_4\right)^{\mu\nu} \left(\gamma_4(C\gamma_5)^{\dagger}\gamma_4\right)^{\gamma\beta} \left(\gamma_4(1)^{\dagger}\gamma_4\right)^{\alpha\tau} \\
&\times \Bigg[- T(\mathbf{0},\mathbf{0},50a,40a,35a)^{\beta'\beta\gamma'\gamma\alpha'\mu\nu\alpha}_{u\,d\,u\,u} - T(\mathbf{0},\mathbf{0},50a,40a,35a)^{\beta'\alpha\gamma'\gamma\alpha'\mu\nu\beta}_{u\,d\,u\,u} \\
&\quad - T(\mathbf{0},\mathbf{0},50a,40a,35a)^{\alpha'\beta\gamma'\gamma\beta'\mu\nu\alpha}_{u\,d\,u\,u} - T(\mathbf{0},\mathbf{0},50a,40a,35a)^{\alpha'\alpha\gamma'\gamma\beta'\mu\nu\beta}_{u\,d\,u\,u} \Bigg] .
\end{aligned}
$$

5.2 Actual implementation

Previously, we worked out the core steps for the construction of stochastic baryon three-point functions which serves as basis for the following discussion. The discussed steps are summarized in Fig. 5.1.

In this section, we introduce several software packages which are supposed to simplify the work with stochastic three-point functions. We highlight, that our implementation enables the user to work with stochastic three-point functions on a usual desktop computer. This however, requires a server-client infrastructure due to the following consideration. The steps I-III, discussed in the last section, can be easily performed on a desktop computer. However, step IV requires strong IO capacities because the operation

$$
\begin{aligned}
&T(\mathbf{0},\mathbf{0},50a,40a,35a)^{\alpha'\alpha\beta'\beta\gamma'\mu\nu\gamma}_{uduu} = \\
&\frac{1}{N_{\text{sto}}} \sum_{i=1}^{N_{\text{sto}}} \Big(S_{ud}(\mathbf{0},50a,35a)^{\alpha'\alpha\beta'\beta\gamma'}_{ic} \times I_{uu}(\boldsymbol{q},40a,35a)^{\mu\nu\gamma}_{ic} \Big) ,
\end{aligned}
$$

must be performed for each of the N_{conf} measurements of the spectator and the insertion (cf. section 4.10). The implemented server-client infrastructure works as follows. The steps I-III are performed on a desktop computer but step IV and V are handled by an IO-Server, equipped with a fast connection to the storage system which servers the spectator and insertion files. The communication between the server and client is implemented using two software packages *rioc*[2] and *rios*[3]. The communication, between server and client requires a request, sent from the client to the server. It can be produced by the *openGFF* package. The Listing 5.2.1 is supposed to demonstrate a

[2]Regensburg IO client [96].

[3]Regensburg IO server [97].

baryon three-point function request, which is hared coded for demonstration purposes only. This example assumes, that *rios* is running on the IO-Server which uses a TCP socket and listens to port 50124. The actual request, is sent to the server in line 39 and triggers the computation of steps IV-V, discussed in section 5.1. The corresponding result, i.e., the baryon three-point function is sent to the client (line 39). Let us remark, that the authentication between *rios* and *rioc* is currently done by a simple magic number check. This is sufficient, because the IO-Server is only reachable within the physics network of the university. In case one wants to have communication over the Internet one can easily implement a challenge-response step which proves the identity of the client.

Listing 5.2.1: Example request for a stochastic baryon three-point function.

```
1  import rioc.client
2  request = {
3    "reader": "Stoch3ptBaryonReader",
4    "version": "1",
5    "task": {
6      "read": {
7        "db": {"task", "store"},
8        "file_dict": {"1": "[1,3,3,4,5]",},
9        "momentum_list": "[((0, 0, 0),(0, 0, 0)),((0, 0, 1),(0, 1, 0)),]",
10       "atomic_request": {
11          # Measurement Specific Request
12          "ensemble": "H102",
13          "num_sto": "100",
14          "noise_smearing_spe": "None",
15          "noise_smearing_ins": "One",
16          "noise_seeding": "Single",
17          # Contraction Sepcific Request
18          "propagator_one_flavor_spectator": "U",
19          "propagator_two_flavor_spectator": "U",
20          "solution_flavor": "D",
21          "propagator_one_flavor_insertion": "D",
22          "del_mu": "0",
23          "del_mu_sign": "1",
24          "direction": "1",
25          "spin_content": "[ '-0.5j*(+gi+gt)*gx*g5', 'gt*H(gy*gt*g5)*gt',
26          'gi', 'gt*H(gi)*gt', 'gy*gt*g5', 'gx*g5']",
27          "contraction_signs": "[-1, -1]",
28          "einsum_strings": "['ab,cd,be,fa,gh,ij,edgfhijc',
29          'ab,cd,be,fa,gh,ij,efgdhijc']",
30          # Analysis Specific Request
31          "channel": "real",
32          "source_sink_distance": "10",
33       },
34     },
35   },
36 }
37 io_server_ip="127.0.0.1"
38 client  = rioc.client.RiosClient(host=io_server_ip, port=50124)
39 data = client.get_data(request) # data.shape = (momenta, config, time)
```

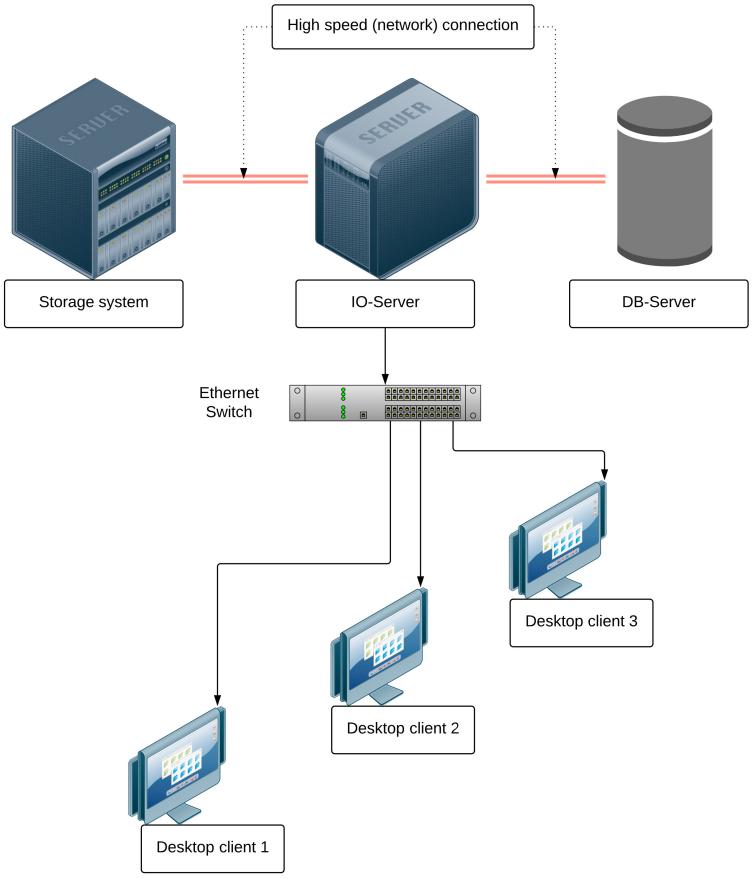

Figure 5.1: Used infrastructure to achieve high speed and usability for the construction of stochastic three-point functions. The computation of the Wick contractions is done on the IO server according to a request from a client created on a desktop computer. Each client is connected to the IO-Server over a usual office network connection (or over the Internet). The IO-Server must have a fast connection to the storage system in order to load the spectator and insertion files as fast as possible. The DB-Server is used to store three-point functions such that a second request does not trigger the computation of the SCT again. This step gives high speed-ups for repeated requests.

5.3 Implementation details

The last section roughly sketches our server-client setup for the computation of stochastic three-point functions. In this section, we discuss some improvements and details of the implementation. We consider the IO-Server which receives a request from a client. In this case, the following happens. The IO-Server computes a hash of the request which servers as an unique key for the three-point function behind this request. To save time for repetitive requests we implement check-pointing which is done by a DB-Server. The IO-Server passes the hash to a DB-Server which returns the three-point function in case that it was computed before. Subsequently, the three-point function is passed from the DB-Server to the IO-Server to the client. This improvement increases the usability of our server-client infrastructure because

it reduces the response time. The origin of the speed-up is the acceleration of the computation for Eqs. (4.21, 4.22, 4.23) which is performed on the IO-Server. For a single stochastic three-point function, measured on the $N401$ CLS ensemble, $\mathcal{O}(7.7)$ seconds are needed for its construction[4]. The IO-Server currently performs trivial parallelization, i.e., parallelization over the different measurements. However, even for 24 parallel jobs it takes 353 seconds to compute a three-point function for all 1100 configurations. Due to check-pointing, this computation must be performed only once. In the following we explain the check-pointing in more detail. To that end, let us consider the example request shown in Listing 5.2.1. We remark, that we do not check-point the whole request. To be able to explain this let us clarify our notation in line 8 of the Listing (5.2.1). The "file_dict" contains information about the considered Monte Carlo stream (1) and the spectator and insertion files, which are mapped to integer numbers. This replacement is used to get rid of file names, which may change over the time and thus potentially change the value of the hash. The mapping, between numbers and files is done on the IO-Server and can be modified with care, if necessary. The "momentum_list", shown in line 9 of Listing (5.2.1) defines a list of ($\boldsymbol{p}'$, $\boldsymbol{q}$) pairs, i.e., the momenta of the three-point function.

For each Monte Carlo stream, each measurement, each momentum pair and the "atomic_request", defined in Listing (5.2.1), we compute a hash and construct the three-point functions accordingly. The size of the three-point function, and thus the check-point size is

$$\text{Size}[C] = \text{Number of insertions} \times 8\,\text{Byte}\,.$$

This further implies, that the amount of data which needs to be transferred over the network (or the Internet) to the client computer is

$$N_{\text{conf}} \times N_{(\boldsymbol{p}',\boldsymbol{q})} \times \text{Number of insertions} \times 8\,\text{Byte}\,,$$

where $N_{(\boldsymbol{p}',\boldsymbol{q})}$ denote the number of momentum pairs. This yields 0.24 Megabyte per momentum combination where we assumed $N_{\text{conf}} = 2000$ and a source-sink separation of $15a$ Finally, let us highlight that the described setup is capable to send other types of lattice data to the client computer. By preparing a suitable request, one can receive stochastic three-point functions meson (HDF5), two-point functions baryon (HDF5), two-point functions meson (HDF5), and momentum averaged two-point functions baryon (lime, $N_f = 2$). The different lattice data formats, are implemented in the *rioi* (Regensburg IO interface) package [98]. It is used by *rios* and serves as an abstraction layer for IO tasks.

[4]This number corresponds to our current setup in Regensburg. I would like to thank Simon Weishäupl for producing the timing.

6
Final summary and outlook

In this work we considered two main topics. First, we have calculated all quark GFFs, corresponding to operators with one derivative, of the nucleon GPDs at leading twist-2. Our lattice calculation includes the dominating connected contributions and neglects contributions from disconnected diagrams. The available gauge ensembles cover a wide range of quark masses and volumes. However, the three available lattice spacings only vary from 0.081 fm down to 0.060 fm. Within errors, all GFFs show a mild dependence on the quark mass, lattice spacing and volume.

We have compared two different fitting strategies for the GFFs and found that the direct fit method appears to be more reliable. With this method the number of fit parameters is reduced to the relevant degrees of freedom. We recommend to use this method in future studies. We have also studied the total angular momentum and the transverse spin density of quarks in the nucleon. Both quantities can be extracted from fits to our GFF data. For the total angular momentum we obtain a similar estimate in the isovector case as ETMC in Ref. [65]. From Ref. [65] we know that these are small. Nevertheless, in the isoscalar case they should definitely be taken into account. For the second moment of the transverse spin density we have found that its distribution in impact parameter space strongly depends on the t-dependence of the GFF data. The shape of the distribution depends on the value of p that is used within a p-pole ansatz. High precision data at small and large values of $-t$ would be required to eliminate this ambiguity. For integrated moments this situation improves. In Fig. 2.25 we provide lattice estimates for the x-weighted probabilities of a transversely polarized (unpolarized) light quark in the upper or lower part of the impact parameter space, within an unpolarized (transversely polarized) nucleon.

We remark that recently new methods have been proposed to obtain information

on parton distribution functions (PDFs), distribution amplitudes (DAs), transverse momentum dependent PDFs (TMDPDFs) and GPDs that is complementary to the computation of Mellin moments with respect to Bjorken-x from expectation values of local currents within external states, see, e.g., Refs. [99, 100, 101, 102, 103, 104]. In these approaches Euclidean correlation functions are computed and then matched within collinear factorization to light cone distribution functions, employing continuum perturbative QCD.

In the second part of this work we introduced a new approach to calculate hadronic three-point functions. Key ingredient is a stochastic timeslice-to-all propagator to factorize the three-point correlation function into the spectator and the insertion. This offers the great advantage to compute connected three-point functions with arbitrary γ-matrices, projection operators, flavors and momentum combinations after the generation of the insertion and the spectator. The efficiency of our implementation is substantially enhanced by the fact that the most computational demanding part, namely the insertion is designed such that it can be used for the calculation of meson and baryon three-point functions. To that end one has to generate the corresponding spectators which is less demanding. We further improve our method by exploiting time-reversal symmetry to calculate the backward propagating three-point functions as well. This reduces the statistical errors of the desired three-point correlation function after forward-backward averaging. Due to an efficient data layout conversion from Chroma to LHA we are able to compute multiple source-sink separations in parallel with reasonable overhead compared to a single source-sink distance. Most strikingly, the number of computed momentum combinations has only a marginal effect to the overall runtime.

The great flexibility and efficiency of our new approach comes not for free. In fact, there are two main drawbacks. The first is the relatively large disk space usage for the spectator and the insertion. However, it should be noted, that the price of disk space decreases with time. Secondly, the construction of three-point functions becomes more complex because it is mandatory to compute the Wick contractions in a second step. However, we hide this complexity with a modern and sophisticated analysis framework. It would be interesting to calculate GFFs with our new method. The necessary spectators and insertions are already computed on a large number of CLS ensembles. With our new method one is not restricted to the nucleon. For instance on could compute the transverse spin density for the Σ particle as done in [105]. Further, it is worth to investigate whether our new method yields better results for GFFs because the set of available momentum combinations is larger compared to the sequential source method. In combination with multiple source-sink separations one can hope to parametrize excited states for the calculation of GFFs. However, a decisive impact can only be achieved if disconnected contributions are taken into

account.

In terms of the construction of stochastic three-point functions one can improve the situation by discarding the idea that all post analysis steps (after the generation of spectator and insertion) are performed in-house. This approach has the serious disadvantage of wasting time by copying the data from one location to another. Actually one should immediately start with the construction of stochastic three-point functions, directly after the measurement of spectator and insertion. This reduces the time to publication and possible mistakes can be identified in an early stage. Furthermore, one can use the resources of the computing center. Our software stack for the construction of stochastic three-point functions can be run everywhere. Assuming that the security policy of the computing center allows a TCP connection one could start the analysis server *rios* on a dedicated virtual server. By virtue of *rioc* one could receive the requested stochastic three-point function on any desktop computer. This setup is especially advantageous if collaborators are geographically separated. Due the implemented checkpointing on the server, everybody would profit.

A Appendix

A.1 γ-matrix conventions

The Euclidean γ-matrices satisfy

$$\{\gamma_\mu, \gamma_\nu\} = 2\,\delta_{\mu\nu}\,, \quad \gamma_\mu^\dagger = \gamma_\mu\,,$$

For all numerical purposes, we use the chiral basis of the γ-matrices (Chroma basis)

$$\gamma_x = \gamma_1 = \begin{pmatrix} 0 & 0 & 0 & i \\ 0 & 0 & i & 0 \\ 0 & -i & 0 & 0 \\ -i & 0 & 0 & 0 \end{pmatrix} \qquad \gamma_y = \gamma_2 = \begin{pmatrix} 0 & 0 & 0 & -1 \\ 0 & 0 & 1 & 0 \\ 0 & 1 & 0 & 0 \\ -1 & 0 & 0 & 0 \end{pmatrix}$$

$$\gamma_z = \gamma_3 = \begin{pmatrix} 0 & 0 & i & 0 \\ 0 & 0 & 0 & -i \\ -i & 0 & 0 & 0 \\ 0 & i & 0 & 0 \end{pmatrix} \qquad \gamma_t = \gamma_4 = \begin{pmatrix} 0 & 0 & 1 & 0 \\ 0 & 0 & 0 & 1 \\ 1 & 0 & 0 & 0 \\ 0 & 1 & 0 & 0 \end{pmatrix}$$

Further we define $\sigma_{\mu\nu} \equiv \frac{i}{2}[\gamma_\mu, \gamma_\nu]$ and $\gamma_5 \equiv \gamma_1\gamma_2\gamma_3\gamma_4 = \mathrm{Diag}(+1, +1, -1, -1)$.

A.2 Used gauge ensembles for the computation of GFFs

In Table A.1 we summarize parameters of the $N_f = 2$ lattice ensembles used for the calculation of nucleon GFFs. For more information about our setup we refer to Ref. [50]

Ensemble	β	a [fm]	κ	V	m_π [GeV]	m_N [GeV]	Lm_π	N_{conf}	t'/a
I	5.20	0.081	0.13596	$32^3 \times 64$	0.2795(18)	1.091(08)	3.69	1986(4)	13
II	5.29	0.071	0.13620	$24^3 \times 48$	0.4264(20)	1.289(15)	3.71	1999(2)	15
III			0.13620	$32^3 \times 64$	0.4222(13)	1.247(06)	4.90	1998(2)	15,17
IV			0.13632	$32^3 \times 64$	0.2946(14)	1.071(11)	3.42	2023(2)	7(1),9(1),11(1),13,15,17
V				$40^3 \times 64$	0.2888(11)	1.079(09)	4.19	2025(2)	15
VI				$64^3 \times 64$	0.2895(07)	1.072(05)	6.71	1232(2)	15
VII			0.13640	$48^3 \times 64$	0.1597(15)	0.968(19)	2.78	3442(2)	15
VIII				$64^3 \times 64$	0.1497(13)	0.944(17)	3.47	1593(3)	9(1),12(2),15
IX	5.40	0.060	0.13640	$32^3 \times 64$	0.490(02)	1.302(11)	4.81	1123(2)	17
X			0.13647	$32^3 \times 64$	0.4262(20)	1.262(09)	4.18	1999(2)	17
XI			0.13660	$48^3 \times 64$	0.2595(09)	1.010(09)	3.82	2177(2)	17

Table A.1: Latin numerals in the first column serve as ensemble identifiers. After the number of configurations N_{conf} we list in parentheses the number of independent (randomly chosen) source positions that we average over within each gauge configuration. Wherever this is indicated by parentheses after the sink-source separation t'/a, a smaller number of sources was used for this value.

Acknowledgements

I would like to express my sincere gratitude to Andreas Schäfer for giving me the opportunity to work on his chair and for his support. Further, I want to thank Gunnar Bali, Sara Collins, Meinulf Göckeler, Andreas Schäfer and André Sternbeck for their joint effort to our publication about Nucleon generalized form factors from two-flavor lattice QCD. I would like to thank Gunnar Bali, Sara Collins, Benjamin Gläßle and Johannes Najjar which helped me to get started as well as for the time they spent in answering my questions. Additionally, I would like to thank all peoples from the RQCD and QCDSF collaborations for generating the necessary gauge ensembles. Likewise, I want to thank all people who are involved in providing the necessary infrastructure like Andreas Schäfer, the Gauss Centre for Supercomputing, SuperMUC at the Leibniz Supercomputing Centre, iData-Cool, QPACE-n, Lurch and Glurch. Further, I gratefully acknowledge all people who spent their time in writing code as Simon Heybrock for his excellent work on LibHadronAnalysis which provides the back-end for the computation of stochastic three-point functions. In particular, I take great pleasure in acknowledging gratitude to Simon Mages, Florian Rappl, Piotr Korcyl, Jakob Simeth, Daniel Richtmann, Marius Löffler Stefan Solbrig, Peter Georg, Simon Weishäupl, Thomas Wurm and Philipp Wein. Finally, I thank my wife Tanja for keeping my back free such that I was able to focus on my work.

References

[1] Kenneth G. Wilson. "Confinement of quarks". In: *Phys. Rev. D* 10 (8 1974), pp. 2445–2459. DOI: 10.1103/PhysRevD.10.2445. URL: https://link.aps.org/doi/10.1103/PhysRevD.10.2445.

[2] Martin Luscher and Stefan Schaefer. "Lattice QCD without topology barriers". In: *JHEP* 07 (2011), p. 036. DOI: 10.1007/JHEP07(2011)036. arXiv: 1105.4749 [hep-lat].

[3] Simon Mages et al. "Lattice QCD on nonorientable manifolds". In: *Phys. Rev.* D95 (2017), p. 094512. DOI: 10.1103/PhysRevD.95.094512. arXiv: 1512.06804 [hep-lat].

[4] Gunnar Bali et al. "Nucleon generalized form factors from lattice QCD with nearly physical quark masses". In: *PoS* LATTICE2015 (2016), p. 118. DOI: 10.22323/1.251.0118. arXiv: 1601.04818 [hep-lat]. URL: http://inspirehep.net/record/1415956/files/arXiv:1601.04818.pdf.

[5] Gunnar Bali et al. "Nucleon generalized form factors from two-flavor lattice QCD". In: *Phys. Rev. D* 100 (1 2019), p. 014507. DOI: 10.1103/PhysRevD.100.014507. URL: https://link.aps.org/doi/10.1103/PhysRevD.100.014507.

[6] Konrad Osterwalder and Robert Schrader. "Axioms for Euclidean Green's functions". In: *Communications in Mathematical Physics* 31.2 (1973), pp. 83–112. ISSN: 1432-0916. DOI: 10.1007/BF01645738. URL: https://doi.org/10.1007/BF01645738.

[7] R.F. Streater and A.S. Wightman. *PCT, spin and statistics, and all that*. 1989. ISBN: 978-0-691-07062-9.

[8] Konrad Osterwalder and Robert Schrader. "Axioms for Euclidean Green's Functions. 2." In: *Commun. Math. Phys.* 42 (1975), p. 281. DOI: 10.1007/BF01608978.

[9] Christof Gattringer and Christian B. Lang. "Quantum chromodynamics on the lattice". In: *Lect. Notes Phys.* 788 (2010), pp. 1–343. DOI: 10.1007/978-3-642-01850-3.

[10] Kenneth G. Wilson. "Quarks and Strings on a Lattice". In: *New Phenomena in Subnuclear Physics: Proceedings, International School of Subnuclear Physics, Erice, Sicily, Jul 11-Aug 1 1975. Part A*. [,0069(1975)]. 1975, p. 99.

[11] H.B. Nielsen and M. Ninomiya. "Absence of neutrinos on a lattice: (I). Proof by homotopy theory". In: *Nuclear Physics B* 185.1 (1981), pp. 20 –40. ISSN: 0550-3213. DOI: https://doi.org/10.1016/0550-3213(81)90361-8. URL: http://www.sciencedirect.com/science/article/pii/0550321381903618.

[12] H.B. Nielsen and M. Ninomiya. "Absence of neutrinos on a lattice: (II). Intuitive topological proof". In: *Nuclear Physics B* 193.1 (1981), pp. 173 –194. ISSN: 0550-3213. DOI: https://doi.org/10.1016/0550-3213(81)90524-1. URL: http://www.sciencedirect.com/science/article/pii/0550321381905241.

[13] H.B. Nielsen and M. Ninomiya. "A no-go theorem for regularizing chiral fermions". In: *Physics Letters B* 105.2 (1981), pp. 219 –223. ISSN: 0370-2693. DOI: https://doi.org/10.1016/0370-2693(81)91026-1. URL: http://www.sciencedirect.com/science/article/pii/0370269381910261.

[14] Paul H. Ginsparg and Kenneth G. Wilson. "A Remnant of Chiral Symmetry on the Lattice". In: *Phys. Rev.* D25 (1982), p. 2649. DOI: 10.1103/PhysRevD.25.2649.

[15] Albert C. Lewis. "H. Grassmann's 1844 Ausdehnungslehre and Schleiermacher's Dialektik". In: *Annals of Science* 34.2 (1977), pp. 103–162. URL: https://doi.org/10.1080/00033797700200171.

[16] Simon Duane et al. "Hybrid Monte Carlo". In: *Physics Letters B* 195.2 (1987), pp. 216 –222. ISSN: 0370-2693. DOI: https://doi.org/10.1016/0370-2693(87)91197-X. URL: http://www.sciencedirect.com/science/article/pii/037026938791197X.

[17] D.H. Weingarten and D.N. Petcher. "Monte Carlo integration for lattice gauge theories with fermions". In: *Physics Letters B* 99.4 (1981), pp. 333 –338. ISSN: 0370-2693. DOI: https://doi.org/10.1016/0370-2693(81)90112-X.

[18] Martin Lüscher. *Computational Strategies in Lattice QCD*. 2010. arXiv: 1002.4232 [hep-lat].

[19] Martin Hasenbusch. "Exploiting the hopping parameter expansion in the hybrid Monte Carlo simulation of lattice QCD with two degenerate flavors of Wilson fermions". In: *Phys. Rev.* D97.11 (2018), p. 114512. DOI: 10.1103/PhysRevD.97.114512. arXiv: 1805.03560 [hep-lat].

[20] S. Gusken. "A Study of smearing techniques for hadron correlation functions". In: *Nucl. Phys. Proc. Suppl.* 17 (1990), pp. 361–364. DOI: 10.1016/0920-5632(90)90273-W.

[21] S. Gusken et al. "Nonsinglet Axial Vector Couplings of the Baryon Octet in Lattice QCD". In: *Phys. Lett.* B227 (1989), pp. 266–269. DOI: 10.1016/S0370-2693(89)80034-6.

[22] Gunnar S. Bali et al. "Novel quark smearing for hadrons with high momenta in lattice QCD". In: *Phys. Rev. D* 93.9 (2016), p. 094515. DOI: 10.1103/PhysRevD.93.094515. arXiv: 1602.05525 [hep-lat].

[23] M. Falcioni et al. "AGAIN ON SU(3) GLUEBALL MASS". In: *Nucl. Phys.* B251 (1985), pp. 624–632. DOI: 10.1016/0550-3213(85)90280-9.

[24] F. M. Dittes et al. "The Altarelli-Parisi kernel as asymptotic limit of an extended Brodsky-Lepage kernel". In: *Phys. Lett.* B209 (1988), p. 325. DOI: 10.1016/0370-2693(88)90955-0.

[25] Dieter Müller et al. "Wave functions, evolution equations and evolution kernels from light ray operators of QCD". In: *Fortsch. Phys.* 42 (1994), p. 101. DOI: 10.1002/prop.2190420202. arXiv: hep-ph/9812448 [hep-ph].

[26] Xiang-Dong Ji. "Gauge-Invariant decomposition of nucleon spin". In: *Phys. Rev. Lett.* 78 (1997), p. 610. DOI: 10.1103/PhysRevLett.78.610. arXiv: hep-ph/9603249 [hep-ph].

[27] A. V. Radyushkin. "Scaling limit of deeply virtual Compton scattering". In: *Phys. Lett.* B380 (1996), p. 417. DOI: 10.1016/0370-2693(96)00528-X. arXiv: hep-ph/9604317 [hep-ph].

[28] John C. Collins, Leonid Frankfurt, and Mark Strikman. "Factorization for hard exclusive electroproduction of mesons in QCD". In: *Phys. Rev. D* 56 (1997), p. 2982. DOI: 10.1103/PhysRevD.56.2982. arXiv: hep-ph/9611433 [hep-ph].

[29] M. Diehl. "Generalized parton distributions". In: *Phys. Rept.* 388 (2003), p. 41. DOI: 10.1016/j.physrep.2003.08.002. arXiv: hep-ph/0307382 [hep-ph].

[30] A. V. Belitsky and A. V. Radyushkin. "Unraveling hadron structure with generalized parton distributions". In: *Phys. Rept.* 418 (2005), p. 1. DOI: 10.1016/j.physrep.2005.06.002. arXiv: hep-ph/0504030 [hep-ph].

[31] A. Airapetian et al. "Measurement of the beam spin azimuthal asymmetry associated with deeply virtual Compton scattering". In: *Phys. Rev. Lett.* 87 (2001), p. 182001. DOI: 10.1103/PhysRevLett.87.182001. arXiv: hep-ex/0106068 [hep-ex].

[32] A. Airapetian et al. "Beam-helicity asymmetry arising from deeply virtual Compton scattering measured with kinematically complete event reconstruction". In: *JHEP* 10 (2012), p. 042. DOI: 10.1007/JHEP10(2012)042. arXiv: 1206.5683 [hep-ex].

[33] Kresimir Kumericki, Simonetta Liuti, and Herve Moutarde. "GPD phenomenology and DVCS fitting". In: *Eur. Phys. J.* A52.6 (2016), p. 157. DOI: 10.1140/epja/i2016-16157-3. arXiv: 1602.02763 [hep-ph].

[34] R. L. Jaffe and Aneesh Manohar. "The g_1 problem: Fact and fantasy on the spin of the proton". In: *Nucl. Phys. B* 337 (1990), p. 509. DOI: 10.1016/0550-3213(90)90506-9.

[35] E. Leader and C. Lorcé. "The angular momentum controversy: Whats it all about and does it matter?" In: *Phys. Rept.* 541.3 (2014), p. 163. DOI: 10.1016/j.physrep.2014.02.010. arXiv: 1309.4235 [hep-ph].

[36] Xiang-Dong Ji et al. "Spin decomposition of the electron in QED". In: *Phys. Rev. D* 93.5 (2016), p. 054013. DOI: 10.1103/PhysRevD.93.054013. arXiv: 1511.08817 [hep-ph].

[37] M. Engelhardt. "Quark orbital dynamics in the proton from Lattice QCD – from Ji to Jaffe-Manohar orbital angular momentum". In: *Phys. Rev. D* 95.9 (2017), p. 094505. DOI: 10.1103/PhysRevD.95.094505. arXiv: 1701.01536 [hep-lat].

[38] Ph. Hägler et al. "Nucleon Generalized Parton Distributions from Full Lattice QCD". In: *Phys. Rev. D* 77 (2008), p. 094502. DOI: 10.1103/PhysRevD.77.094502. arXiv: 0705.4295 [hep-lat].

[39] J. D. Bratt et al. "Nucleon structure from mixed action calculations using $2+1$ flavors of asqtad sea and domain wall valence fermions". In: *Phys. Rev. D* 82 (2010), p. 094502. DOI: 10.1103/PhysRevD.82.094502. arXiv: 1001.3620 [hep-lat].

[40] C. Alexandrou et al. "Moments of nucleon generalized parton distributions from lattice QCD". In: *Phys. Rev. D* 83 (2011), p. 114513. DOI: 10.1103/PhysRevD.83.114513. arXiv: 1104.1600 [hep-lat].

[41] S. N. Syritsyn et al. "Quark contributions to nucleon momentum and spin from Domain Wall fermion calculations". In: *PoS* LATTICE2011 (2011), p. 178. arXiv: 1111.0718 [hep-lat].

[42] A. Sternbeck et al. "First moments of the nucleon generalized parton distributions from lattice QCD". In: *PoS* LATTICE2011 (2011), p. 177. arXiv: 1203.6579 [hep-lat].

[43] C. Alexandrou et al. "Nucleon form factors and moments of generalized parton distributions using $N_f = 2+1+1$ twisted mass fermions". In: *Phys. Rev. D* 88.1 (2013), p. 014509. DOI: 10.1103/PhysRevD.88.014509. arXiv: 1303.5979 [hep-lat].

[44] G. S. Bali et al. "Nucleon generalized form factors and sigma term from lattice QCD near the physical quark mass". In: *PoS* LATTICE2013 (2014), p. 291. arXiv: 1312.0828 [hep-lat].

[45] Constantia Alexandrou et al. "Nucleon transversity generalized form factors with twisted mass fermions". In: *PoS* LATTICE2013 (2014), p. 294. arXiv: 1311.4670 [hep-lat].

[46] Xiang-Dong Ji et al. "One-Loop Matching for Generalized Parton Distributions". In: *Phys. Rev. D* 92 (2015), p. 014039. DOI: 10.1103/PhysRevD.92.014039. arXiv: 1506.00248 [hep-ph].

[47] Jiunn-Wei Chen et al. "Nucleon Helicity and Transversity Parton Distributions from Lattice QCD". In: *Nucl. Phys. B* 911 (2016), p. 246. DOI: 10.1016/j.nuclphysb.2016.07.033. arXiv: 1603.06664 [hep-ph].

[48] Jiunn-Wei Chen, Xiang-Dong Ji, and Jian-Hui Zhang. "Improved quasi parton distribution through Wilson line renormalization". In: *Nucl. Phys. B* 915 (2017), p. 1. DOI: 10.1016/j.nuclphysb.2016.12.004. arXiv: 1609.08102 [hep-ph].

[49] Jian-Hui Zhang et al. "Pion Distribution Amplitude from Lattice QCD". In: *Phys. Rev. D* 95.9 (2017), p. 094514. DOI: 10.1103/PhysRevD.95.094514. arXiv: 1702.00008 [hep-lat].

[50] G. S. Bali et al. "Nucleon isovector couplings from $N_f = 2$ lattice QCD". In: *Phys. Rev. D* 91.5 (2015), p. 054501. DOI: 10.1103/PhysRevD.91.054501. arXiv: 1412.7336 [hep-lat].

[51] John C. Collins and Andreas Freund. "Proof of factorization for deeply virtual Compton scattering in QCD". In: *Phys. Rev. D* 59 (7 1999), p. 074009. DOI: 10.1103/PhysRevD.59.074009. URL: https://link.aps.org/doi/10.1103/PhysRevD.59.074009.

[52] Xiang-Dong Ji. "Off forward parton distributions". In: *J. Phys.* G24 (1998), p. 1181. DOI: 10.1088/0954-3899/24/7/002. arXiv: hep-ph/9807358 [hep-ph].

[53] Ph. Hägler. "Hadron structure from lattice quantum chromodynamics". In: *Phys. Rept.* 490 (2010), p. 49. DOI: 10.1016/j.physrep.2009.12.008. arXiv: 0912.5483 [hep-lat].

[54] M. Vanderhaeghen, Pierre A. M. Guichon, and M. Guidal. "Deeply virtual electroproduction of photons and mesons on the nucleon: Leading order amplitudes and power corrections". In: *Phys. Rev. D* 60 (1999), p. 094017. DOI: 10.1103/PhysRevD.60.094017. arXiv: hep-ph/9905372 [hep-ph].

[55] K. Goeke, Maxim V. Polyakov, and M. Vanderhaeghen. "Hard exclusive reactions and the structure of hadrons". In: *Prog. Part. Nucl. Phys.* 47 (2001), p. 401. DOI: 10.1016/S0146-6410(01)00158-2. arXiv: hep-ph/0106012 [hep-ph].

[56] L. Maiani et al. "Scalar densities and baryon mass differences in lattice QCD with Wilson fermions". In: *Nucl. Phys. B* 293 (1987), p. 420. ISSN: 0550-3213. DOI: https://doi.org/10.1016/0550-3213(87)90078-2. URL: http://www.sciencedirect.com/science/article/pii/0550321387900782.

[57] G. S. Bali et al. "$\langle x \rangle_{u-d}$ from lattice QCD at nearly physical quark masses". In: *Phys. Rev. D* 86 (2012), p. 054504. DOI: 10.1103/PhysRevD.86.054504. arXiv: 1207.1110 [hep-lat].

[58] G. S. Bali et al. "The moment $\langle x \rangle_{u-d}$ of the nucleon from $N_f = 2$ lattice QCD down to nearly physical quark masses". In: *Phys. Rev. D* 90.7 (2014), p. 074510. DOI: 10.1103/PhysRevD.90.074510. arXiv: 1408.6850 [hep-lat].

[59] G. Martinelli et al. "A general method for nonperturbative renormalization of lattice operators". In: *Nucl. Phys. B* 445 (1995), p. 81. DOI: 10.1016/0550-3213(95)00126-D. arXiv: hep-lat/9411010 [hep-lat].

[60] K. G. Chetyrkin and A. Retey. "Renormalization and running of quark mass and field in the regularization invariant and $\overline{\text{MS}}$ schemes at three loops and four loops". In: *Nucl. Phys. B* 583 (2000), p. 3. DOI: 10.1016/S0550-3213(00)00331-X. arXiv: hep-ph/9910332 [hep-ph].

[61] J. A. Gracey. "Three loop anomalous dimension of the second moment of the transversity operator in the $\overline{\text{MS}}$ and RI' schemes". In: *Nucl. Phys. B* 667 (2003), p. 242. DOI: 10.1016/S0550-3213(03)00543-1. arXiv: hep-ph/0306163 [hep-ph].

[62] M. Göckeler et al. "Perturbative and Nonperturbative Renormalization in Lattice QCD". In: *Phys. Rev. D* 82 (2010). DOI: 10.1103/PhysRevD.82.114511, 10.1103/PhysRevD.86.099903. arXiv: 1003.5756 [hep-lat].

[63] Daniel Boer and P. J. Mulders. "Time reversal odd distribution functions in leptoproduction". In: *Phys. Rev. D* 57 (1998), p. 5780. DOI: 10.1103/PhysRevD.57.5780. arXiv: hep-ph/9711485 [hep-ph].

[64] Philipp Wein, Peter C. Bruns, and Andreas Schäfer. "First moments of nucleon generalized parton distributions in chiral perturbation theory at full one-loop order". In: *Phys. Rev. D* 89.11 (2014), p. 116002. DOI: 10.1103/PhysRevD.89.116002. arXiv: 1402.4979 [hep-ph].

[65] C. Alexandrou et al. "Nucleon spin and momentum decomposition using Lattice QCD simulations". In: *Phys. Rev. Lett.* 119.14 (2017), p. 142002. DOI: 10.1103/PhysRevLett.119.142002. arXiv: 1706.02973 [hep-lat].

[66] M. Diehl and Ph. Hägler. "Spin densities in the transverse plane and generalized transversity distributions". In: *Eur. Phys. J.* C44 (2005), p. 87. DOI: 10.1140/epjc/s2005-02342-6. arXiv: hep-ph/0504175 [hep-ph].

[67] M. Göckeler et al. "Transverse spin structure of the nucleon from lattice QCD simulations". In: *Phys. Rev. Lett.* 98 (2007), p. 222001. DOI: 10.1103/PhysRevLett.98.222001. arXiv: hep-lat/0612032 [hep-lat].

[68] Davison E. Soper. "Parton model and the Bethe-Salpeter wave function". In: *Phys. Rev. D* 15 (4 1977), p. 1141. DOI: 10.1103/PhysRevD.15.1141. URL: https://link.aps.org/doi/10.1103/PhysRevD.15.1141.

[69] Johannes Siegfried Samir Najjar. *Nucleon structure from stochastic estimators*. 2014. URL: https://epub.uni-regensburg.de/30694/.

[70] Constantia Alexandrou et al. "A Stochastic Method for Computing Hadronic Matrix Elements". In: *Eur. Phys. J.* C74.1 (2014), p. 2692. DOI: 10.1140/epjc/s10052-013-2692-3. arXiv: 1302.2608 [hep-lat].

[71] Richard Evans, Gunnar Bali, and Sara Collins. "Improved Semileptonic Form Factor Calculations in Lattice QCD". In: *Phys. Rev.* D82 (2010), p. 094501. DOI: 10.1103/PhysRevD.82.094501. arXiv: 1008.3293 [hep-lat].

[72] Gunnar S. Bali et al. "Nucleon structure from stochastic estimators". In: *PoS* LATTICE2013 (2014), p. 271. DOI: 10.22323/1.187.0271. arXiv: 1311.1718 [hep-lat].

[73] Yi-Bo Yang et al. "Stochastic method with low mode substitution for nucleon isovector matrix elements". In: *Phys. Rev.* D93.3 (2016), p. 034503. DOI: 10.1103/PhysRevD.93.034503. arXiv: 1509.04616 [hep-lat].

[74] S. Capitani et al. "Nucleon axial charge in lattice QCD with controlled errors". In: *Phys. Rev. D* 86 (7 2012), p. 074502. DOI: 10.1103/PhysRevD.86.074502. URL: https://link.aps.org/doi/10.1103/PhysRevD.86.074502.

[75] Simon Dinter et al. "Precision study of excited state effects in nucleon matrix elements". In: *Physics Letters B* 704.1 (2011), pp. 89 –93. ISSN: 0370-2693. DOI: https://doi.org/10.1016/j.physletb.2011.09.002. URL: http://www.sciencedirect.com/science/article/pii/S0370269311010628.

[76] J.R. Green et al. "Nucleon structure from Lattice QCD using a nearly physical pion mass". In: *Physics Letters B* 734 (2014), pp. 290 –295. ISSN: 0370-2693. DOI: https://doi.org/10.1016/j.physletb.2014.05.075. URL: http://www.sciencedirect.com/science/article/pii/S0370269314003852.

[77] Shigemi Ohta. "Nucleon axial charge in 2+1-flavor dynamical DWF lattice QCD". In: *PoS* LATTICE2013 (2014), p. 274. DOI: 10.22323/1.187.0274. arXiv: 1309.7942 [hep-lat].

[78] B. Jäger et al. "A high-statistics study of the nucleon EM form factors, axial charge and quark momentum fraction". In: *PoS* LATTICE2013 (2014), p. 272. DOI: 10.22323/1.187.0272. arXiv: 1311.5804 [hep-lat].

[79] J. R. Green et al. "Nucleon Scalar and Tensor Charges from Lattice QCD with Light Wilson Quarks". In: *Phys. Rev.* D86 (2012), p. 114509. DOI: 10.1103/PhysRevD.86.114509. arXiv: 1206.4527 [hep-lat].

[80] Parikshit M. Junnarkar et al. "Nucleon axial form factors from two-flavour Lattice QCD". In: *PoS* LATTICE2014 (2015), p. 150. DOI: 10.22323/1.214.0150. arXiv: 1411.5828 [hep-lat].

[81] Huey-Wen Lin et al. "Nucleon structure with two flavors of dynamical domain-wall fermions". In: *Phys. Rev.* D78 (2008), p. 014505. DOI: 10.1103/PhysRevD.78.014505. arXiv: 0802.0863 [hep-lat].

[82] Takeshi Yamazaki et al. "Nucleon form factors with 2+1 flavor dynamical domain-wall fermions". In: *Phys. Rev.* D79 (2009), p. 114505. DOI: 10.1103/PhysRevD.79.114505. arXiv: 0904.2039 [hep-lat].

[83] Tanmoy Bhattacharya et al. "Nucleon Charges and Electromagnetic Form Factors from 2+1+1-Flavor Lattice QCD". In: *Phys. Rev.* D89.9 (2014). DOI: 10.1103/PhysRevD.89.094502. arXiv: 1306.5435 [hep-lat].

[84] Constantia Alexandrou et al. "Nucleon observables and axial charges of other baryons using twisted mass fermions". In: *PoS* LATTICE2014 (2015), p. 151. DOI: 10.22323/1.214.0151. arXiv: 1411.3494 [hep-lat].

[85] Stefano Capitani et al. "Systematic errors in extracting nucleon properties from lattice QCD". In: *PoS* LATTICE2010 (2010), p. 147. DOI: 10.22323/1.105.0147. arXiv: 1011.1358 [hep-lat].

[86] Gunnar S. Bali et al. "Hyperon couplings from $N_f = 2 + 1$ lattice QCD". In: *PoS* LATTICE2019 (2019), p. 099. arXiv: 1907.13454 [hep-lat].

[87] Rudolf Rödl. *wick - A python package to compute Wick contractions*. https://rqcd.ur.de:8443/rudi_roedl/wick. 2018.

[88] Travis E. Oliphant. *Guide to NumPy*. Provo, UT, Mar. 2006. URL: http://www.tramy.us/.

[89] Shao-Jing Dong and Keh-Fei Liu. "Stochastic estimation with Z(2) noise". In: *Phys. Lett.* B328 (1994), pp. 130–136. DOI: 10.1016/0370-2693(94)90440-5. arXiv: hep-lat/9308015 [hep-lat].

[90] S. Bernardson, P. McCarty, and C. Thron. "Monte Carlo methods for estimating linear combinations of inverse matrix entries in lattice QCD". In: *Comput. Phys. Commun.* 78 (1993), pp. 256–264. DOI: 10.1016/0010-4655(94)90004-3.

[91] Simon Heybrock. *LHA*. https://rqcd.ur.de:8443/hes10653/lib-hadron-analysis. 2019.

[92] Robert G. Edwards and Balint Joo. "The Chroma software system for lattice QCD". In: *Nucl. Phys. Proc. Suppl.* 140 (2005). [,832(2004)], p. 832. DOI: 10.1016/j.nuclphysbps.2004.11.254. arXiv: hep-lat/0409003 [hep-lat].

[93] Rudolf Rödl. *chromaxml - Creates your chroma xml file with less pain and less bugs*. https://rqcd.ur.de:8443/kern/chromaxml. 2019.

[94] Gunnar S. Bali et al. "Baryonic and mesonic 3-point functions with open spin indices". In: *EPJ Web Conf.* 175 (2018), p. 06014. DOI: 10.1051/epjconf/201817506014. arXiv: 1711.02384 [hep-lat].

[95] Rudolf Rödl. *openGFF - A python package to calculate stochastic thee-point functions*. https://rqcd.ur.de:8443/rudi_roedl/openGFF. 2018.

[96] Rudolf Rödl. *rioc - Regensburg IO Client*. https://rqcd.ur.de:8443/rudi_roedl/rioc. 2019.

[97] Rudolf Rödl. *rios - Regensburg IO Server*. https://rqcd.ur.de:8443/rudi_roedl/rios. 2019.

[98] Rudolf Rödl. *rioc - Regensburg IO Interface*. https://rqcd.ur.de:8443/rudi_roedl/rioi. 2019.

[99] Xiang-Dong Ji. "Parton Physics on a Euclidean Lattice". In: *Phys. Rev. Lett.* 110 (2013), p. 262002. DOI: 10.1103/PhysRevLett.110.262002. arXiv: 1305.1539 [hep-ph].

[100] Huey-Wen Lin et al. "Flavor Structure of the Nucleon Sea from Lattice QCD". In: *Phys. Rev. D* 91 (2015), p. 054510. DOI: 10.1103/PhysRevD.91.054510. arXiv: 1402.1462 [hep-ph].

[101] Constantia Alexandrou et al. "Lattice calculation of parton distributions". In: *Phys. Rev. D* 92 (2015), p. 014502. DOI: 10.1103/PhysRevD.92.014502. arXiv: 1504.07455 [hep-lat].

[102] Constantia Alexandrou et al. "Updated lattice results for Parton Distributions". In: *Phys. Rev. D* 96.1 (2017), p. 014513. DOI: 10.1103/PhysRevD.96.014513. arXiv: 1610.03689 [hep-lat].

[103] Gunnar S. Bali et al. "Pion distribution amplitude from Euclidean correlation functions: Exploring universality and higher-twist effects". In: *Phys. Rev. D* 98.9 (2018), p. 094507. DOI: 10.1103/PhysRevD.98.094507. arXiv: 1807.06671 [hep-lat].

[104] V. Braun and Dieter Müller. "Exclusive processes in position space and the pion distribution amplitude". In: *Eur. Phys. J.* C55 (2008), p. 349. DOI: 10.1140/epjc/s10052-008-0608-4. arXiv: 0709.1348 [hep-ph].

[105] James Zanotti et al. "Transverse spin densities of octet baryons using Lattice QCD". In: Feb. 2017, p. 163. DOI: 10.22323/1.256.0163.